Excavating the fossil record of spiral galaxies

Thomas Peterken

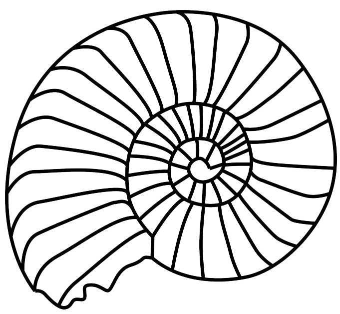

Thesis submitted to the University of Nottingham
for the degree of Doctor of Philosophy

March 2020

Take another deep breath
and another cup of whatever it is you are drinking

– Roberto Cid Fernandes, 2007. *Spectral Fitting with Starlight*

Supervisors:	Prof. Alfonso Aragón-Salamanca	
	Prof. Michael Merrifield	
Examiners:	Dr. Jesús Falcón Barroso	(IAC Tenerife)
	Prof. Frazer Pearce	(University of Nottingham)
Examination chair:	Dr. Meghan Gray	
Submitted:	31 March 2020	
Examined:	14 May 2020	
Final version:	23 May 2020	

Contents

Abstract

Despite spiral galaxies being extremely common in our local neighbourhood, their formation, growth, and dynamics are not fully understood. However, the spatial variation in the properties of stellar populations contained within spiral galaxies are expected to bear the imprint of some of the past and present physical processes driving global and local structure and dynamics. Combining modern integral-field spectroscopic galaxy surveys with spectral fitting methods offers an unprecedented opportunity to peer into the stellar population "fossil record" and how it varies between and within spiral galaxies. By obtaining a full star-formation history at every location, it is possible to construct images denoting the spatial distribution of stars of different ages across the galaxy. In this thesis we explore how such a "time slicing" technique can be applied to data from the SDSS-IV MaNGA survey, and show that this approach can provide insights into the formation and the internal structure of spiral galaxies.

While the defining features of spiral galaxies are the beautiful arms that they display, the exact nature of such structure is still an open question. It has been widely assumed that spiral arms in "grand design" systems are the products of density waves that propagate around the disk with an approximately constant angular speed Ω_P. We show that it is possible to measure an offset between young stars of a known age and the spiral arm in which they formed in a grand-design spiral galaxy, consistent with predictions of a density wave model. By measuring how this offset varies with radius, we obtain a direct measure of Ω_P at a range of radii, and show that the spiral pattern in this galaxy is consistent with being quasi-stationary.

We then investigate how the azimuthal structures of the barred spiral galaxy MCG+07-28-064 vary when traced by stars of different ages. Decomposing this galaxy into "time slices", we find evidence for the ongoing growth of the bar, and for the most recent star formation occurring on its leading edge. We also show that spiral arms can be traced in stellar populations as old as 2 Gyr, providing further evidence for the density wave model of spiral structure.

In preparation to apply time slicing analyses to a large population of galaxies, we refine and test the spectral fitting methods. We show that the stellar population fitting techniques employed in this thesis must be carefully interpreted. For example, we find that accurately extracting the very youngest ($\leq$ 30 Myr) stellar populations is not feasible, due to the limitations of modelling template spectra. However, reassuringly, we demonstrate that most populations can be reliably modelled in all of the conditions typically found in MaNGA galaxies.

Finally, we perform a fossil record analysis for a large population of low-redshift spiral galaxies, thereby making use of the full power of MaNGA's sample size. By measuring the mean stellar ages and formation times as a function of galactic radius — and also the radial profiles of different time slices — we find evidence for inside-out growth being a generic feature of spiral galaxies, and most significant in massive galaxies. By interpreting the radial profiles of time slices as indicative of the size of the galaxy at the time those populations had formed, we are able to use the stellar population fossil record to quantitatively trace the simultaneous growth in mass and size of the spiral galaxies over the last 10 Gyr. Despite finding that the evolution of the measured light-weighted radius is consistent with inside-out growth in the majority of spiral galaxies, we observe that an equivalent mass-weighted radius has changed little over the same time period. Since radial migration effects are likely to be small, we conclude that although the growth of disks in spiral galaxies has occurred predominantly through an inside-out mode, this has not had anywhere near as much impact on the distribution of stellar mass within spiral galaxies.

These studies show that there is a wealth of untapped information on the spatial variation of the stellar populations which is now available to exploit with the current generation of integral-field spectroscopic galaxy surveys. A time-slicing approach to studying the fossil record is therefore an extremely powerful technique to answer some open questions on the structure and dynamics of spiral galaxies.

Acknowledgements

Firstly, I must thank Mike and Alfonso for being the best supervisors I could ask for. Thanks for the lively discussions every week, and for always managing to somehow make time to listen to my "can I just check something?" or "do you want to see something interesting?" in between those meetings. Your relentless enthusiasm for this work has been contagious and you've never failed to convince me that what I've been doing has (usually) been pretty interesting. Thanks also for your seemingly endless patience when I've been indecisive about everything non-science. It is very much appreciated.

I also need to say thanks to everyone else who's been part of the little MaNGA family at Nottingham. Martha, Mick, Becky, and especially Amelia; thanks for the helpful sciencey discussions, for being excellent travel buddies to Santiago, Alabama, Oxford, and Shanghai, and most importantly for providing opportunities to rant about whatever part of the project has been most frustrating recently. I should also thank the wider SDSS collaboration for being so welcoming. I couldn't possibly have wished to be part of a more simultaneously exciting and caring project.

I think every PhD thesis to come out of CAPT should gratefully acknowledge Phil's knowledgeable assistance, without whom nothing could be done because nothing would work. You're a genius.

Also thanks to everyone who I have been involved in outreach with, particularly the Inflatiteam: CB, Roan, Amy, Jake, Rachel, Ross. It's been so important to have those frequent opportunities to be reminded why astronomy matters. Working with you has been so very rewarding.

Thanks to the regular 3pm tea gang (Lizzie, Simon, Roan, CB, Amy, Mick, Karel) for providing a break to look forward to every day, for the consistent moral support, and for always agreeing that LaTeX/Python/science/politics/society/COVID-19 is daft. Also thanks to everyone I've shared A108 with — Ulli, Ross, Martha, Simon, Mick, Florian, Agustín — for creating such a healthy working environment, for always being ready to help out, and for occasionally humouring me when I get excited by the bird life outside the window. Truly the best office.

Thank you too to Matt and all my other wonderful friends in the music department (past and present) for providing creativity, respite, and support, and for treating me as one of your own. Also thanks to my DP & Penarth friends — Dan, Siân, Naina, Adam — who have helped to keep me motivated this whole time.

Of course, I'd also like to thank my whole family. Thanks for taking an interest in what I do, to show me that at least some people care what I'm trying to find out about galaxies. I always said I'd be a scientist when I grew up, and here I am: I guess I can call myself a scientist now, but maybe not yet a grown-up. Thank you for your enthusiastic and truly unerring support at every step along the way from those first children's space books to here.

Finally, thank you Hannah for your constant support, for your patience, and for showing me how exciting it is to find things out.

Published works

The majority of the material presented in this thesis has already been published in journals as the following three works.

i **Peterken T. G.**, Merrifield M. R., Aragón-Salamanca A., Drory N., Krawczyk C. M., Masters K. L., Weijmans A.-M., Westfall K. B., 2019a. *A direct test of density wave theory in a grand-design spiral galaxy*. Nature Astronomy, 3, 178–182.

ii **Peterken T. G.**, Fraser-McKelvie A., Aragón-Salamanca A., Merrifield M. R., Kraljic K., Knapen J. H., Riffel R., Brownstein J., Drory N., 2019b. *Time-slicing spiral galaxies with SDSS-IV MaNGA*. Monthly Notices of the Royal Astronomical Society, 489, 1338–1343.

iii **Peterken T. G.**, Merrifield M. R., Aragón-Salamanca A., Fraser-McKelvie A., Avila-Reese V., Riffel R., Knapen J. H., Drory N. *SDSS-IV MaNGA: Excavating the fossil record of stellar populations in spiral galaxies*. Monthly Notices of the Royal Astronomical Society, ?, ?–?.

Chapter 3 is based on material published in Paper i, Chapter 4 on that in Paper ii, and Chapters 5 and 6 contains work described in Paper iii.

The vast majority of work presented here was carried out by the author, with advice from the paper co-authors above. Where the work contains the product of larger collaborations, this is mentioned in the relevant chapter.

Chapter 1

Introduction

The dynamics and growth of spiral galaxies and their structural components are not fully understood. The work contained in this thesis aims to use observations from the SDSS-IV MaNGA survey to derive spatially-resolved star-formation histories, in order to better understand the growth of spiral galaxies, and the nature of their spiral arms and bars.

Some background and motivation for the work in this thesis is detailed in this chapter. First, an historical overview of the study of galaxy morphology is contained in Section 1.1. Section 1.2 then further details some of the relevant current understanding of the structure, growth, and dynamics of spiral galaxies. We then outline the general principles of spectral fitting and integral-field spectroscopy — key to much of the work presented here — in Sections 1.3 and 1.4.

Where relevant throughout this thesis, we assume a ΛCDM cosmology with $\Omega_\lambda = 0.7$, $\Omega_\mathrm{m} = 0.3$, and $H_0 = 70$ km s^{-1} Mpc^{-1}, consistent with results from the Planck Collaboration et al. (2018). All logarithms are base-10, unless stated otherwise.

Figures 4.2, 6.1, 6.10, and 7.3 include animations which require Adobe Reader or similar to view properly in the pdf. Alternative versions of these figures are available online at tinyurl.com/peterken-thesis.

1.1 Galaxy morphology

Spiral structure had been observed and documented in galaxies by the Earl of Rosse (1845–1850) — notably in M51 and M99 — before it was confirmed that such 'nebulae' were not located within the Milky Way. It wasn't until Hubble (1925, 1926a, 1929) measured accurate distances to NGC 6822, M31, and M33 — using Cepheid variables as the first "standard candles" (Leavitt & Pickering, 1912) — that it was shown that these objects are indeed extragalactic. Since then, many studies in the field of extragalactic astronomy have focused or made use of the classification of galaxies by their morphological appearance.

It has been obvious since early studies of galaxy morphology (e.g. Hubble 1926b) that galaxies generally fall into one of two broad classes. Elliptical galaxies appear smooth and featureless, while spiral galaxies comprise principally a flattened disk within which is embedded spiral structure. Hubble (1936) introduced a full classification scheme with "early type" elliptical galaxies and "late type" spiral galaxies being linked by the S0 lenticular class, which are smooth and featureless like ellipticals but contain a prominent disk like the spiral galaxies. This scheme also began to acknowledge the enormous variation in morphology between different spiral galaxies: the spiral galaxies are split into two branches, separating the "normal" and barred spirals, and are further

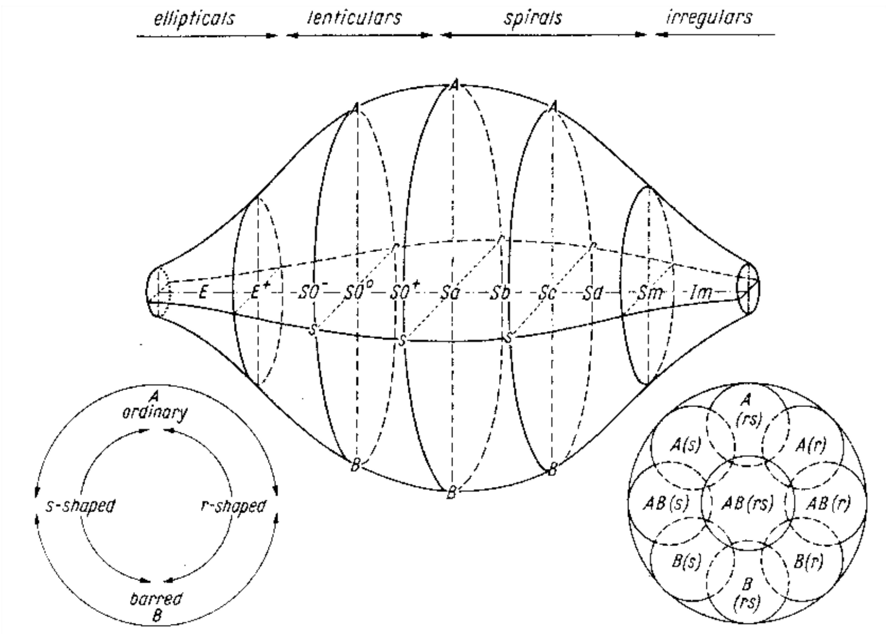

Figure 1.1: The de Vaucouleurs classification scheme. Galaxies are arranged on three axes: general morphological type (x-axis), and by the presence of bars or rings (y- and z-axes). Originally shown as Figure 3 of de Vaucouleurs (1959).

classified as Sa, Sb, and Sc denoting increasingly "open" spiral arms and decreasing prominence of the bulge in spirals. The equivalent subclassification of barred galaxies is denoted by SBa, SBb, and SBc.

The variety of structures present in galaxies was further expanded in numerous later classification schemes, including the one developed by de Vaucouleurs (1959, 1963). In this scheme, galaxies are arranged in three dimensions to describe the presence of morphological features such as spiral arms, bars, and galactic rings, as shown in Figure 1.1. Such an approach allows for more detailed subdivisions of Hubble's classification of galaxies of a single spiral type, as shown in Figure 1.2. Both the Hubble and de Vaucouleurs classifications — and other variants of them — are still in use for morphological studies of galaxies today.

It is worth highlighting that these classification schemes are not discrete, in that they are based on the presence — or otherwise — of internal structures which vary

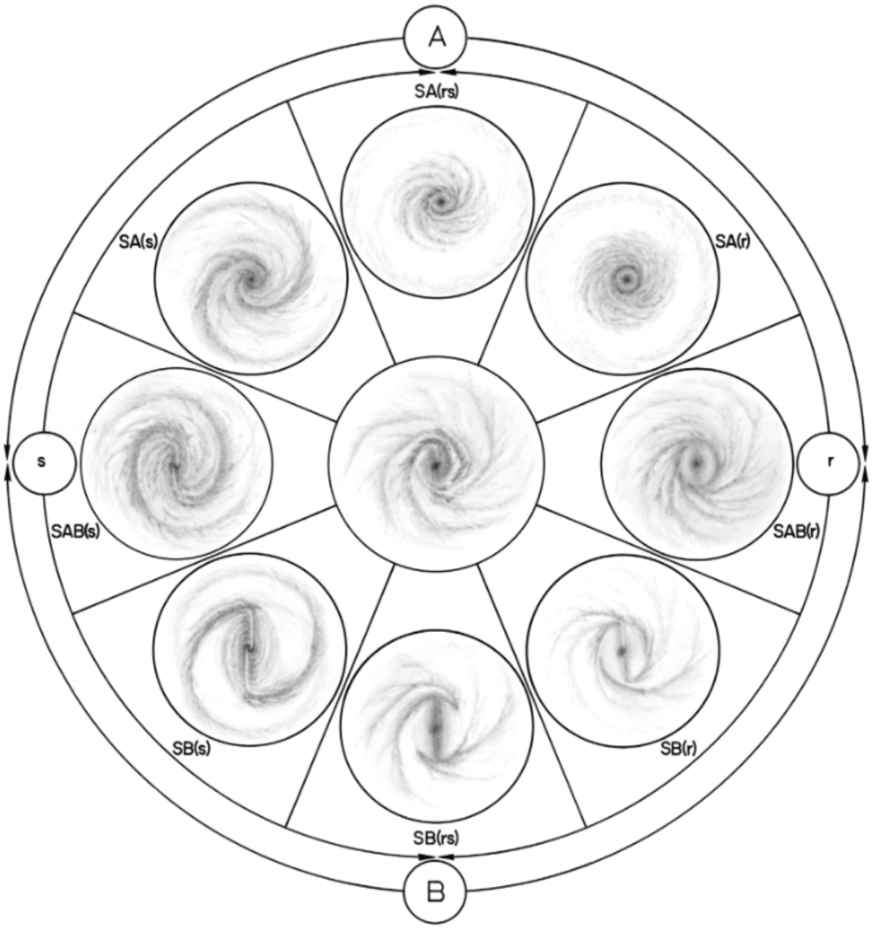

Figure 1.2: A slice of the de Vaucouleurs classification scheme (shown in Figure 1.1) for spirals near stage Sb, showing the variety of ring (increasing prominence towards the right) and bar (increasing prominence towards the bottom) structure within spiral galaxies. Original illustration by de Vaucouleurs (1963), reproduced as Figure 1.13 by Buta et al. (2007).

continuously in strength between galaxies. As a result, the classification of any single galaxy on these schemes can be subjective (Naim et al., 1995). There is also evidence that the tendency to simultaneously classify spirals based on both the bulge size and arm winding is flawed since these are often independent parameters (Freeman, 1970; Hart et al., 2017a, 2018; Masters et al., 2019). However, in any general morphological classification scheme, the distinction between smooth early-type galaxies and structured late-type galaxies is accepted as being a fundamental difference.

Having established the types of galaxies we see in the Universe, the question arises of why different galaxies should exhibit such variety in appearance. Spiral galaxies are generally bluer in colour (e.g. Holmberg 1958), are forming stars at a higher rate (e.g. Roberts 1963; Kennicutt 1983), are located in less-dense environments (Dressler, 1980), have stronger net angular momentum (Emsellem et al., 2007; Cappellari et al., 2011b; Graham et al., 2018), and are less massive (Blanton & Moustakas, 2009) than ellipticals and lenticulars, suggesting an evolutionary sequence of galaxies transitioning from late to early types as they grow and fall into gravitational wells. However, the exact mechanisms by which a spiral galaxy can cease its star formation, lose internal non-axisymmetric structure, and redistribute its angular momentum during this process are still not fully understood and are matters of active research.

1.2 Spiral galaxies

A simple model of a spiral galaxy comprises a dynamically hot core forming a bulge component, and a rotation-supported disk component (Freeman, 1970). Current research suggests that these components are distinct in their stellar populations (Kennedy et al., 2016b; Coccato et al., 2018; Breda & Papaderos, 2018) and kinematics (Taranu et al., 2017; Zhu et al., 2018; Tabor et al., 2019). Although the bulge and disk dominate a spiral galaxy's light and mass (Mackereth & Bovy, 2020), other fainter components exist. For example, the stellar halo is a faint extended spherical component which exists in the Milky Way (e.g. Kinman et al. 1966; Searle & Zinn 1978; Mackereth & Bovy 2020) and other spiral galaxies (e.g. Monachesi et al. 2016). There is also tentative evidence for the separation of the disk component into distinct thin and thick disks based on their typical scale heights in other galaxies (Burstein, 1979; Yoachim & Dalcanton, 2006; Comerón et al., 2015; Kalinova et al., 2017) and the Milky Way (Gilmore & Reid, 1983), but the distinctness of these sub-components is disputed by some authors (e.g. Bovy et al. 2012, 2016).

1.2.1 Disk growth

It is thought that disk galaxies form and grow hierarchically. Initially small density perturbations in the early Universe grow and accrete dark matter through gravity (White & Rees, 1978) and gain angular momentum due to interactions with neighbouring dark matter protohalos (Silk, 2001). These halos then accrete gas (Fall & Efstathiou, 1980) which dissipates energy to collapse into a star-forming disk (Binney, 1977; Kereš et al., 2005).

Colour and stellar population gradients are observed in most galactic disks (Gonzalez-Perez et al., 2011; Kennedy et al., 2016a,b; Ellison et al., 2018), suggesting that they grow "inside-out" (e.g. Coccato et al. 2018; Sacchi et al. 2019). This scenario is backed up by studies of galaxy populations over different redshifts, showing that the typical sizes of galaxies grow rapidly as they build mass (e.g. Trujillo et al. 2007; van der Wel et al. 2008; van Dokkum et al. 2008, 2013). However, neither of these approaches fully measures the exact growth rate of individual disk galaxies. Colour gradients (or mean stellar age gradients; e.g. Sánchez-Blázquez et al. 2014; González

Delgado et al. 2015; Zheng et al. 2017) are generally unable to imply the formation sequence of a galaxy in a fully quantitative manner, while studies of galaxies at different redshifts can only measure the average growth of galaxy populations. This issue is further discussed in Chapter 6.

1.2.2 Bars

The majority of spiral galaxies host a bar (Sellwood & Wilkinson, 1993; Knapen et al., 2000; Eskridge et al., 2000; Aguerri et al., 2009). The exact processes by which a bar forms, grows, and interacts with the other galactic components are areas of active research. It is thought that bars are long-lived (Gadotti et al., 2015) disk-related phenomena capable of redistributing the angular momentum within their host galaxies (Simkin et al., 1980; Weinberg, 1985; Knapen et al., 1995; Minchev & Famaey, 2010). They can also be responsible for large-scale redistributing of a galaxy's gas (Hernquist & Mihos, 1995; Martin & Friedli, 1997) and dust (Sánchez-Menguiano et al., 2015), and can therefore affect the spatial distribution of stellar populations (Di Matteo et al., 2013; Gavazzi et al., 2015; Seidel et al., 2016; Molaeinezhad et al., 2017; Fraser-McKelvie et al., 2018, 2019). Bars can also influence the structure and number of spiral arms (Block et al., 2004; Salo et al., 2010; Dobbs & Baba, 2014; Hart et al., 2017b).

In dynamical models, most stars in the bar region are trapped on orbits which are elongated in the direction of the bar's axis (Contopoulos & Papayannopoulos, 1980; Athanassoula, 1992) with little mixing between bar- and disk-related orbits, making the bar a distinct component of a spiral galaxy. This separation is in contrast with spiral arms, for which it is generally accepted that stellar and gaseous matter is constantly passing through, and which therefore do not have stellar or gas constituents that are distinct from the disk component.

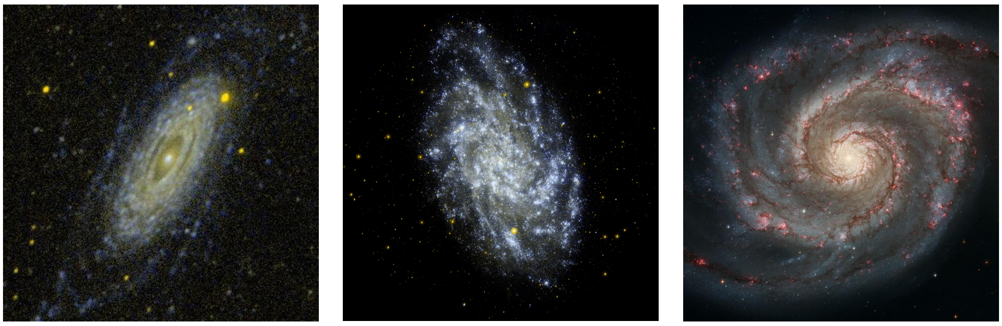

(a) NGC 2841 (b) M33 Triangulum (c) M51a Whirlpool

Figure 1.3: Examples of the three main classes of unbarred spiral galaxies. *a*: NGC2851, a flocculent galaxy with a fractured spiral pattern.[1] *b*: The Triangulum Galaxy M33, a many-arm spiral galaxy.[2] *c*: The Whirlpool Galaxy M51a, a grand design spiral with two clear arms.[3]

1.2.3 Spiral structure

Spiral arms are associated with locally-high star formation rates (Toomre, 1977; Calzetti et al., 2005; González Delgado et al., 2017) which in turn have been found to affect the local gas and dust properties (Grabelsky et al., 1987; Holwerda et al., 2005; Sakhibov et al., 2018; Kreckel et al., 2019). However, there is evidence to suggest that the exact effects that spiral arms have on the local stellar populations (Dobbs & Pringle, 2010; Sánchez-Gil et al., 2011; Hart et al., 2017b), gas properties (Sánchez-Menguiano et al., 2017, 2020), and global structural parameters (Bittner et al., 2017) of a galaxy depend on the dominant type of spiral structure.

There are broadly three such types of spiral structure, examples of which are shown in Figure 1.3. “Flocculent” spirals have no clearly-defined spiral arms, and show instead patchy discontinuous structure throughout their disk, like NGC 2841 in Figure 1.3a. The majority of spiral galaxies are “multi-arm” like M33 in Figure 1.3b, with three or more arms which can show breaks along their lengths. By contrast, “grand design” spirals

[1]Source image at `wikisky.org`
[2]Source image at `https://photojournal.jpl.nasa.gov`
[3]Source image at `http://www.spacetelescope.org`

— like M51a in Figure 1.3c — exhibit a pair of well-defined high-contrast arms which extend over most of their radius (Elmegreen & Elmegreen, 1982). Recent studies have shown that the Milky Way is likely a flocculent (Quillen et al., 2018) or multi-armed (Hunt et al., 2018) barred (Blitz & Spergel, 1991; Anders et al., 2019) spiral galaxy (see Xu et al. 2018 for a review).

Just as the Hubble (1936) and de Vaucouleurs (1963) morphological classifications are capturing the imprint of different physical processes occurring on a galaxy scale, the above classification of spiral galaxies based on the type of spiral structure is likely to be physically-motivated, since different mechanisms are thought to be responsible for generating them (Dobbs & Baba, 2014; Bittner et al., 2017). However, those exact mechanisms which give rise to spiral structure — and how they vary to induce the above distinct forms of such structure — are poorly understood.

In some galaxies, the presence of grand design structure could be due to the influence of a bar (Sellwood & Sparke, 1988) or tidal interactions from a nearby galaxy (Oh et al., 2008; Dobbs et al., 2010; Struck et al., 2011; Kendall et al., 2015). The leading model for the nature of coherent spiral structure — regardless of the excitation mechanism — is a quasi-stationary density wave. This model was developed by Lin & Shu (1964, 1966) as an explanation for the propagation of large-scale structure in a stable disk with a nearly fixed pattern speed. Such a model with its single radially-invariant pattern speed neatly explains the apparent lack of extremely tightly-wound spiral arms in nearby grand design galaxies which should be expected if the spiral arm co-rotates with the stellar disk (Kalnajs, 1973; Bertin et al., 1989). Although some studies find evidence supporting this model (e.g. Egusa et al. 2009; Miller et al. 2019), recent observations suggest that it does not fully explain the spiral structure in all galaxies (e.g. Hart et al. 2017a, 2018; Masters et al. 2019). The quasi-stationary density wave model in grand design spiral structure is further discussed in Chapter 3.

By contrast, simulations suggest that the primary driver of flocculent spiral structure is stochastic self-propagating star formation, whereby star formation causes shock waves in an unstable gas disk which then induce further star formation in neighbouring regions, preferentially propagating along spiral pathways due to the disk's rotation (Mueller & Arnett, 1976; Gerola & Seiden, 1978; Dobbs et al., 2018). Arms produced in this manner — or by similarly stochastic mechanisms — may be transient in nature (Sellwood & Carlberg, 1984, 2014). This model appears to explain the spiral structure in most nearby flocculent spiral galaxies well (e.g. Jungwiert & Palous 1994; Thornley & Mundy 1997b; Mineikis & Vansevičius 2010; Tenjes et al. 2017). However, others have also found evidence for some underlying density wave structures to still be present in flocculent galaxies (Thornley, 1996; Thornley & Mundy, 1997a; Berman, 2003), possibly providing an explanation for the handful of galaxies for which two or more entirely different forms of spiral structure can be observed in different photometric bands in a single galaxy (Grosbol & Patsis, 1998; Eskridge et al., 2000; Kendall et al., 2011).

1.3 Spectral fitting

This thesis makes use of full spectral fitting to study stellar populations. In principle, the spectrum of a galaxy contains a wealth of information about the composition of the galaxy's stellar, gas, and dust contents, as well as the kinematics of the gas and stars. However, in practice, obtaining such information to perform a "fossil record" analysis is not straightforward and requires careful analysis.

Early works studying the chemical compositions of different stellar populations in the Milky Way aimed to distinguish the formation history of the different components of the Galaxy (e.g. Hearnshaw 1972; Demarque & McClure 1977; Searle & Zinn 1978).

These studies made use of the locations of stellar populations in the Hertzsprung–Russell diagram, but others (e.g. Tinsley 1968; Searle et al. 1973; Bruzual 1983) began the more sophisticated approach of using stellar evolution models to directly infer the ages and metallicities of populations in observed spectra, initially through broad-band photometry or individual line indices (Wood, 1966; Faber, 1972; Worthey, 1994; Kauffmann et al., 2003) and later by using the entire visible spectrum. This approach is now widespread, with many libraries of stellar population templates publicly available (e.g. Leitherer et al. 1999; Bruzual & Charlot 2003; Maraston 2005; Vazdekis et al. 2010; Maraston & Strömbäck 2011). Walcher et al. (2011) and Conroy (2013) provide detailed reviews of the applications of and processes involved in creating stellar population models, but some key information relevant to the material in this thesis is described here.

1.3.1 Stellar population models

Creating a model spectrum of a stellar population such as that of a galaxy requires several ingredients, which are illustrated in Figure 1.4. Firstly, a library of stellar spectra is required. This library is often a collection of observed spectra of Milky Way stars, and there are now a number of such collections (e.g. Prugniel & Soubiran 2001; Le Borgne et al. 2003; Valdes et al. 2004; Sánchez-Blázquez et al. 2006; Rayner et al. 2009; Chen et al. 2011). These empirical libraries suffer from poor coverage in some regions of parameter space (notably in that they lack high-mass, low-metallicity stars), and their quality is limited by the spectral resolution and calibration of the observations. An alternative approach is to use purely theoretical stellar spectra. Although theoretical libraries (e.g. Lejeune et al. 1997, 1998; Westera et al. 2002; Coelho et al. 2005, 2007; Martins et al. 2005; Munari et al. 2005) cover a wide range of star types, they are still unable to fully model all absorption features when compared to observed spectra (Kučinskas et al., 2005; Kurucz, 2011) or even each other (Martins & Coelho, 2007).

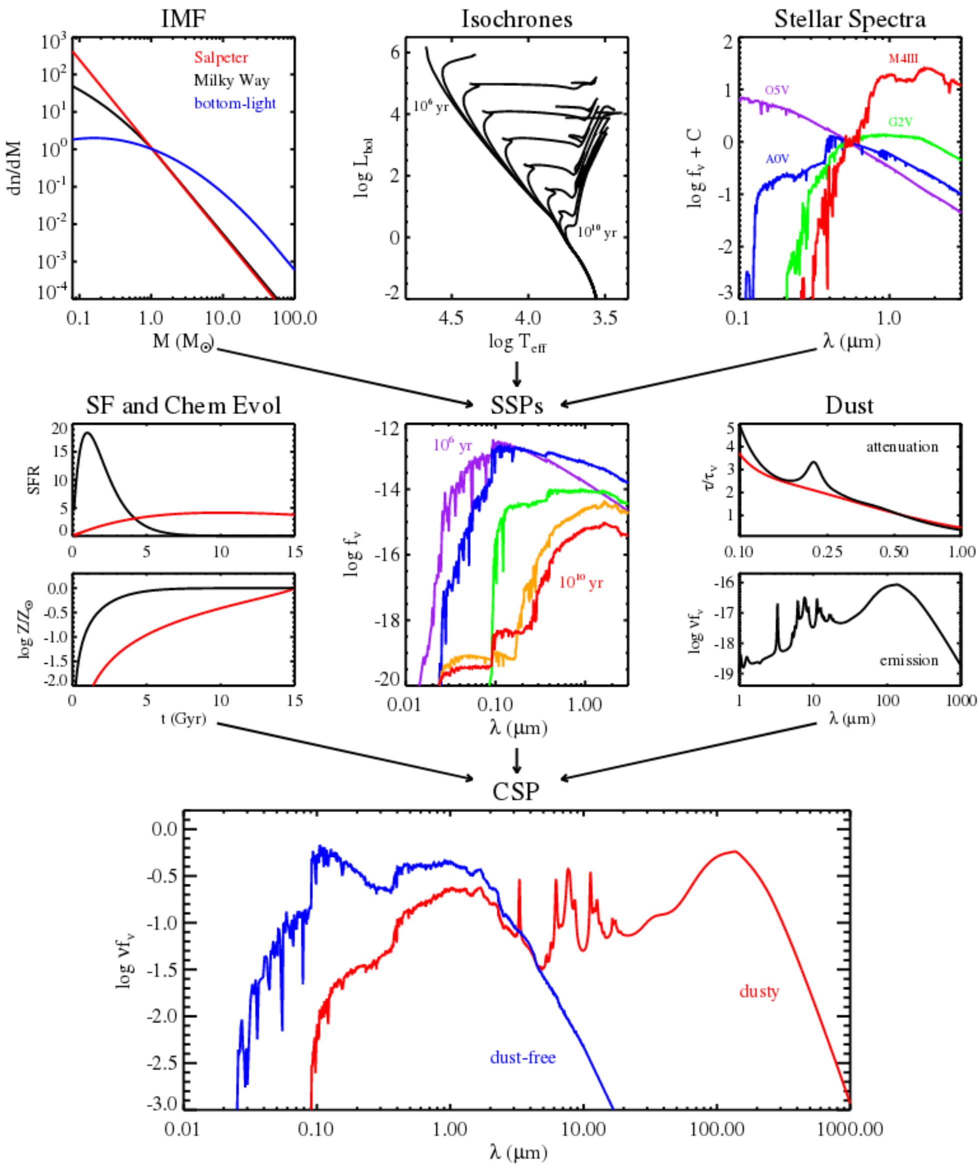

Figure 1.4: The creation of a synthetic composite stellar population (CSP) spectrum such as that of a galaxy requires several ingredients. Measured stellar spectra are combined with model isochrones and an initial mass function (IMF) shape to create single stellar population (SSP) spectra. These SSPs are then combined with star-formation and chemical evolution models, and a model wavelength-dependent dust extinction curve is applied. Figure originally shown as Figure 1 in Conroy (2013).

These stellar spectra must be combined with an initial mass function (IMF) describing the zero-age relative frequency of stars of different masses. Despite extensive studies into the form of the IMF, significant uncertainties remain which can affect the results of stellar population modelling (Tinsley, 1980; Maraston, 1998; van Dokkum et al., 2008; Conroy et al., 2009; Pforr et al., 2012). The IMF and stellar spectra must also be combined with model isochrones, describing how a given stellar population evolves over time through parameter space. Uncertainties in isochrones are large in the rapid later phases of stellar evolution — such as the evolution of stars after the asymptotic giant branch (post-AGB stars) — which can also affect stellar population modelling (Charlot et al., 1996; Maraston, 1998, 2005; Yi, 2003; Lee et al., 2007; Conroy et al., 2009; Ge et al., 2019).

1.3.2 Deriving star-formation histories

Notwithstanding the uncertainties in each ingredient used in constructing single stellar populations (Conroy et al., 2009, 2010; Conroy & Gunn, 2010), many works have successfully used them to measure star-formation histories (SFHs) and shown that the results obtained are broadly reliable (e.g. Cid Fernandes et al. 2005; Li et al. 2017; de Amorim et al. 2017; Cid Fernandes 2018; see also Chapter 5). Several tools to measure the SFHs of galaxies using single stellar population templates (SSPs) exist. Parametric implementations use a generalised and parametrised star-formation history shape (and a dust extinction law) to create a composite stellar population (CSP; as shown in Figure 1.4) which best matches the galaxy spectrum (e.g. Franzetti et al. 2008; Moustakas et al. 2011; Chevallard & Charlot 2016; Carnall et al. 2018; Boquien et al. 2019; Smethurst et al. 2019). While a parametric implementation can be computationally fast, the choice of SFH shape can severely bias the fitting results, particularly for star-forming galaxies (Lee et al., 2009, 2010; Maraston et al., 2010; Wuyts et al., 2011; Pforr et al., 2012).

By contrast, non-parametric fitting routines (e.g. Heavens et al. 2000; Cappellari & Emsellem 2004; Cid Fernandes et al. 2005; Ocvirk et al. 2006b; Tojeiro et al. 2007; Koleva et al. 2009; Sánchez et al. 2006) fit the stellar population templates to the galaxy's spectrum without any assumption regarding the shape of the star-formation history or the level of dust extinction. The drawbacks of this flexible approach are that the resulting star-formation histories or dust model are not physically motivated, and that there are many more degrees of freedom which can result in unconstrained fits and degeneracies, so careful interpretation of results is required. Nevertheless, Cid Fernandes et al. (2005), Panter et al. (2007), Li et al. (2017), de Amorim et al. (2017), Ge et al. (2018), Cid Fernandes (2018) and others have shown that different non-parametric fitting tools give generally consistent results.

1.4 Integral-field spectroscopy

Integral-field spectroscopic (IFS) observations obtain spectra at multiple locations across an imaging field using an integral-field unit (IFU), combining the spatial information of two-dimensional imaging with the diagnostic power of spectroscopy. A single observation can therefore be considered as a "datacube".

Although integral-field spectrographs have been in development and use for several decades (e.g. see Bacon et al. 1988, 1995; Courtes et al. 1988; Barden & Wade 1988; Guerin & Felenbok 1988; Garcia et al. 1994; Arribas et al. 1998a,b for early examples), large-scale galaxy IFS surveys have been more recent undertakings. SAURON (Bacon et al., 2001) obtained integral-field spectroscopy for the inner regions of 72 early-type galaxies, and was later extended to a sample of $\sim$ 300 with ATLAS3D (Cappellari et al., 2011a). More recently, CALIFA (with a sample of 600 galaxies; Sánchez et al.

2012), SAMI (3400 galaxies; Croom et al. 2012), and now MaNGA (10,000 galaxies; Bundy et al. 2015) are providing extensive data to probe the variation of stellar and gas properties across galaxies of all types to better understand their formation and evolution. The MaNGA survey is detailed in Chapter 2, and a succinct comparison of these IFS surveys is outlined by Sánchez (2015).

In the context of spiral galaxies, modern IFS surveys have been previously used to understand how the properties of gas in the interstellar medium is affected by galaxy properties (e.g. Sánchez-Menguiano et al. 2019; Mingozzi et al. 2020; Schaefer et al. 2020) and by spiral arms (e.g. Sánchez-Menguiano et al. 2017; Ho et al. 2017; Sakhibov et al. 2018; Poetrodjojo et al. 2018). Other studies have focused on understanding the kinematics of galaxies and their structural components (e.g. Falcón-Barroso et al. 2006, 2017, 2019; Tabor et al. 2017, 2019; Zhu et al. 2018), the dynamics of bars (e.g. Barrera-Ballesteros et al. 2014; Aguerri et al. 2015; Cuomo et al. 2019; Garma-Oehmichen et al. 2020), or on stellar population parameters such as variations in the IMF (Parikh et al., 2018).

Many other studies of the stellar populations in spiral galaxies with IFS surveys have focused on how average stellar properties — particularly age and metallicity — vary with radius (e.g. Goddard et al. 2017; Li et al. 2017; Boardman et al. 2020), and have generally found a trend of the stellar populations at the centres of spiral galaxies being older and more metal-rich than their outskirts. This approach has been extended by Sánchez-Blázquez et al. (2014) for example, who find that these age gradients are not significantly affected by the presence of bars. However, this result has recently been challenged by Fraser-McKelvie et al. (2019).

Some work has started to go beyond mean stellar ages and metallicities, towards using full star-formation histories to understand how a full "fossil record" approach can help in studying a galaxy's active galactic nucleus (Mallmann et al., 2018), structural components (Cid Fernandes et al., 2013), star formation rate (González Delgado et al., 2016), disk growth (Pérez et al., 2013; Ibarra-Medel et al., 2016; González Delgado et al., 2017), and contribution to the Universe's star-formation history (Sánchez et al., 2019). Such fossil record studies are possible since the spatial distributions of different stellar populations contain imprints of the growth and dynamics of the galaxy. This approach — of making full use of stellar population fitting — is the one that we primarily use throughout this thesis. Some further background to fossil record analysis with integral-field spectroscopy is discussed in later chapters, especially in Chapters 4 and 6.

1.5 Outline of this thesis

This thesis makes use of star-formation histories measured using spectral fitting methods applied to integral-field spectroscopic observations from the SDSS-IV MaNGA survey. In Chapter 2, we describe the data from the MaNGA integral-field spectroscopic survey and some technical details regarding the specific spectral fitting tools used in this thesis. Chapter 3 describes an initial application for which the stellar populations in spiral galaxies can be used to test the quasi-stationary density wave model of spiral structure. In Chapter 4, we outline a general approach to studying the spatially-resolved fossil records of spiral galaxies, and explore some more ways in which such an approach can be used to better understand the properties and nature of the bar and spiral arms. We then perform some tests and improvements to these spectral fitting methods in Chapter 5. Chapter 6 studies the fossil records of a large population of spiral galaxies to uncover their historical growth sequences. Finally, the general conclusions of the thesis and some related future work are outlined in Chapter 7.

Chapter 2

Data and technical methods

This Chapter details some of the key data and software used in this thesis. Most importantly, the acquisition and reduction of MaNGA data is described in Section 2.1. Additionally, throughout this work some data from the Galaxy Zoo:3D citizen science project are used, so this is also described in Section 2.2. Finally, this work makes significant use of the spectral fitting code STARLIGHT and single stellar population (SSP) templates, so brief descriptions of these are also outlined in Sections 2.3 and 2.4.

2.1 SDSS-IV MaNGA

MaNGA is one of the three major programmes of the fourth generation of the Sloan Digital Sky Survey (SDSS-IV; Blanton et al. 2017). It is the largest integral-field spectroscopic galaxy survey to date, and will acquire observations of over 10,000 galaxies by its completion in late 2020. Observations began in the summer of 2014 and as of writing in early 2020, 8405 galaxy datacubes have been observed, reduced, and released in the most recent internal data release. The survey's overview and science goals are described by Bundy et al. (2015). The section outlines some of the key details regarding the design, data, observations, reduction, and sample selection of MaNGA, but further details are found within the technical references given in each subsection.

2.1.1 Instrumentation

In common with all current and previous SDSS programmes, MaNGA makes use of the Sloan telescope (Gunn et al., 2006). Its spectroscopic data collection is done using the BOSS spectrograph (Smee et al., 2013), but adapted to be used with specially-designed integral-field units (Drory et al., 2015).

2.1.1.1 The Sloan telescope

MaNGA observations are acquired using the 2.5 m SDSS telescope at the Apache Point Observatory (APO), located in the Sacramento Mountains of New Mexico, USA. The telescope was initially commissioned for imaging and spectroscopy for the first generation of the Sloan Digital Sky Survey SDSS-I, and was designed to have a large (3°) field of view (FOV), making it ideal for the MaNGA survey. Its first light was in May 1998, and has been fully operational since 2000. The full details of the telescope's design and construction are described by Gunn et al. (2006).

An interesting design feature is the telescope's location on the side — rather than the top — of the observatory's peak, as shown in Figure 2.1. It is situated on a platform projecting $\sim$ 20 m into the prevailing wind, eliminating wake turbulence from the ridge. For the same reason, during observations the telescope's entire enclosure is moved downwind of the telescope by means of a roll-away crane structure (Figure 2.1, lower panel). This also reduces heat contamination in observations.

Figure 2.1: The 2.5 m SDSS telescope at APO. *Top*: The telescope's enclosure housing the telescope during the day. Note the side door of the enclosure for scale. *Bottom*: The telescope at sunset, with the enclosure rolled away for observing. Photos taken by the author, April 2018.

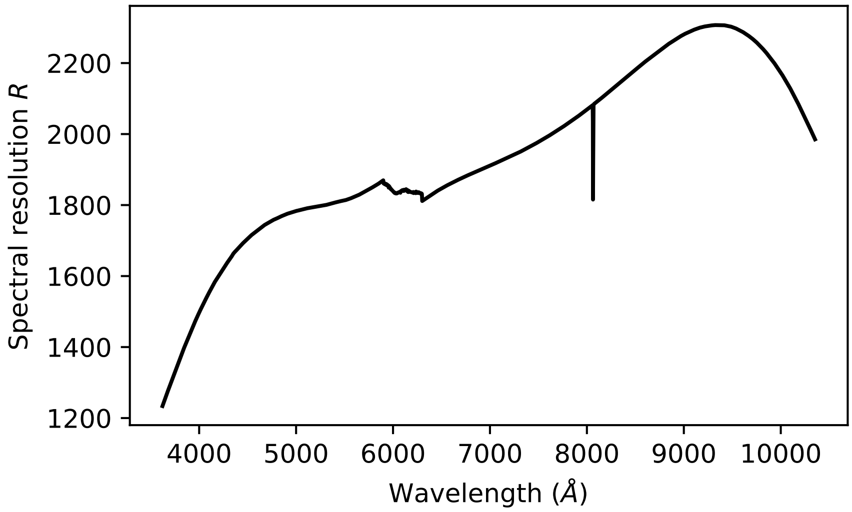

Figure 2.2: A typical spectral resolution R spectrum for a MaNGA galaxy using the BOSS spectrograph (Smee et al., 2013). The feature at $\sim$ 6000 Å is due to the effects of the dichroic beamsplitter of the BOSS spectrograph, where the coverage of the red and blue arms of the spectrograph overlap. The feature at $\sim$ 8000 Å relates to a single-pixel discontinuity in the red arm's CCD detector (Yan et al., 2016b).

2.1.1.2 The BOSS spectrograph

The two spectrographs used for MaNGA are the BOSS spectrographs, described by Smee et al. (2013). The total wavelength coverage makes use of the full optical window, over the range of 3600–10300 Å. This range is achieved through two "arms" which cover the blue (3600–6300 Å) and red (5900–10300 Å) regions separately. The overall spectral resolving power R — defined as the ratio of the FWHM of the line spread function (LSF) to the wavelength — is a function of wavelength, and varies from $R \sim 1500$ at the blue end of the spectrum to $R \sim 2500$ near the red end, as shown in Figure 2.2.

2.1.1.3 MaNGA integral field units

The fibres in MaNGA integral-field units (IFUs) are hexagonally packed and are each separated by cladding and a small buffer region. This results in a relatively poor fill

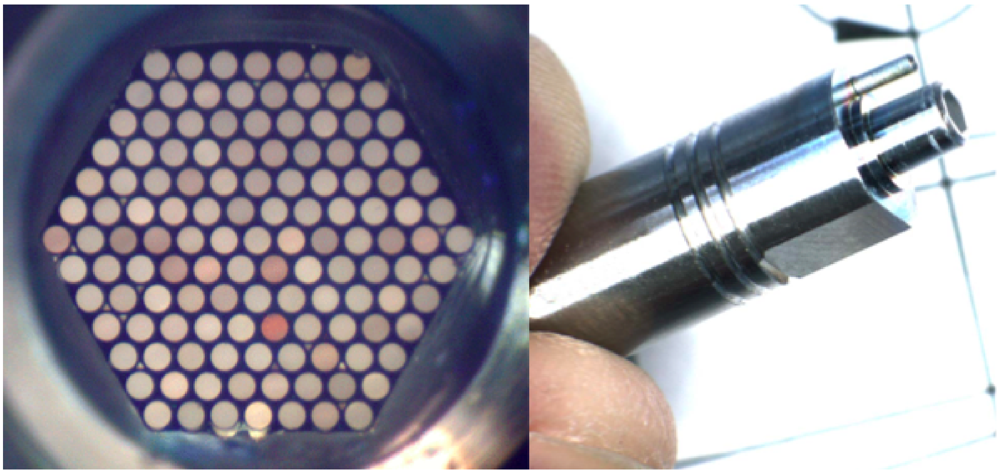

Figure 2.3: A 127-fibre IFU. *Left*: hexagonal packing of fibres within the IFU. *Right*: The ends of these fibres are held in place by a ferrule, which allows it to be plugged into an SDSS plate. See fingertips for scale. Image courtesy of SDSS (https://www.sdss.org/surveys/manga/).

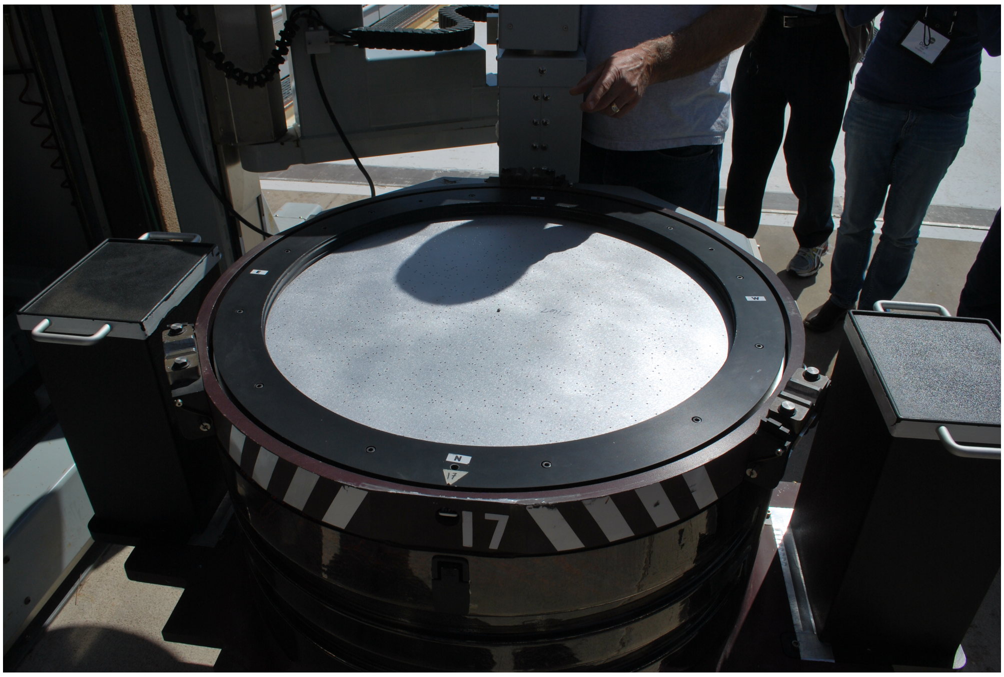

Figure 2.4: An SDSS plate loaded into a cartridge, ready to be loaded onto the telescope. Shown is an SDSS-III BOSS plate (Dawson et al., 2013), but MaNGA plates are similar. Image source: https://commons.wikimedia.org/wiki/File:SDSS_spectrograph_cartridge.JPG

fraction of 56%, but improved fibre throughput and decreased breakages (an important consideration for a long survey) as compared to an IFU design comprising fibres in concentric rings (Law et al., 2015). MaNGA observations utilise five different sizes of IFUs, with sizes of 19, 37, 61, 91, and 127 fibres, granting fields of view ranging from 12 to 32 arcsec. The full specifications regarding the requirement of these sizes of IFU is described by Wake et al. (2017), and the manufacturing and design considerations of these units is described by Drory et al. (2015).

Each IFU is encased in a metal "ferrule" as shown in Figure 2.3, which is plugged into an aluminium plate, where each plate's holes are uniquely drilled for every observation. During drilling (done off-site), the plates are deformed so that the fibres align with the principal ray at the focal plane of the telescope. Plugging is done by hand during daytime, and the plugged plates are loaded onto "cartridges" prior to a night's observing, as shown in Figure 2.4. During observing nights, these cartridges are loaded onto the telescope by hand using a trolley. This procedure is outlined by Drory et al. (2015).

Each plate has a unique four-digit number, and each IFU has a unique four- or five-digit number, so galaxies in this thesis are commonly referred to by their plate-IFU designation. The first two or three digits denote the IFU size, so for example galaxy 8132-12702 was observed using the second of the 127-fibre IFUs on plate number 8132.

2.1.2 Sample selection

All MaNGA target galaxies are located in the region covered by the SDSS-II imaging footprint (described by Abazajian et al. 2009). As a compromise between sample size, spatial coverage, and spatial resolution, there are three main subsamples within the MaNGA target selection, which are more fully described by Yan et al. (2016a) and Wake et al. (2017):

- The Primary sample accounts for 45.1% of the full sample, for which observations extend out to at least 1.5 R_e in at least 80% of cases (where R_e is the elliptical semi-major effective radius), thereby covering the majority of a galaxy's light. The sample is designed to have an approximately flat distribution in stellar mass $M_\star$ within the range 10^9–10^{11} $M_\odot$ h^{-2} so that trends with mass are able to be measured with a statistically powerful number of galaxies at either end of the sample. However, to avoid the model dependencies in measurements of $M_\star$, the sample is in practice selected to have a flat distribution in the K-corrected i-band magnitude M_i, which is a good proxy for stellar mass. No bias is added in the colour selection; the Primary sample at any given mass is volume-limited. As a result, the sample is simply defined by selecting from a redshift window at any given M_i. This window is defined to be at the lowest possible redshift whilst still satisfying the selection criteria.

- The Secondary sample accounts for 35.7% of MaNGA IFU usage. It is sampled in the same way (i.e. with a flat distribution in M_i but volume-limited at any given $M_\star$), but with coverage extending further, to 2.5 R_e. Due to the requirement of greater spatial extent, the Secondary sample is selected from galaxies at a higher redshift window at each M_i than the Primary sample. Since this results in poorer signal-to-noise and lower spatial resolution in kpc, the Secondary sample is primarily designed for emission-line studies.

- The Colour-Enhanced sample constitutes 15.0% of the MaNGA galaxy sample, for which observations extend to 1.5 R_e. This sample targets regions of the colour–magnitude space which have few galaxies, for example the "green valley", high-mass blue, or low-mass red galaxies. The Primary and the Colour-Enhanced samples together form the Primary+ sample.

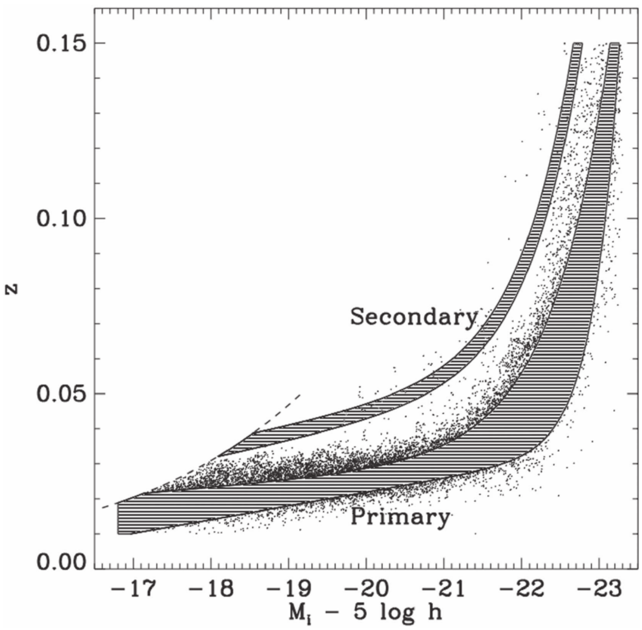

Figure 2.5: The selection for the main MaNGA samples in luminosity–redshift space. The Primary and Secondary samples are indicated by shaded regions, and the dots indicate the Colour-Enhanced sample. Figure taken from Yan et al. (2016a, Figure 1)

The remaining 4.2% allocation of IFUs is given to ancillary projects targeting specific rare classes of galaxy, repeat observations (in cases of overlapping plates), or to observe random "filler" galaxies.

The MaNGA targeting criteria result in the full sample having a median redshift of 0.03. The luminosity–redshift selection windows for the main samples is shown in Figure 1 of Yan et al. (2016a), which is reproduced here as Figure 2.5.

2.1.2.1 Sample weights

It is important to emphasise that although the samples are selected to be volume-limited at any single given stellar mass, the overall full sample and all of the main subsamples are not. Specifically, the requirement of flat distributions in M_i results in a significant over-abundance of high-mass galaxies compared to a volume-limited sample.

However, since the MaNGA selection criteria are well-defined, it is straightforward to weight each galaxy in any of the samples so that the properly weighted sample represents a volume-limited one, as described by Wake et al. (2017). We use these weights to calculate population averages, so that the weighted average corresponds to that of a fully representative sample of galaxies within the MaNGA stellar mass range. In practice, this requires high-mass galaxies to be assigned a low sample weighting and vice-versa in the Primary and Secondary samples. The sample weighting of each galaxy in the Primary+ sample also accounts for the over-sampling of unusual colour space by the Colour-Enhanced sample. As a result, a galaxy in the Primary sample for example will have three associated sample weightings; one for using that galaxy as part of the Primary sample, one for the Primary+ sample, and one for the entire (Primary+ and Secondary combined) sample.

2.1.3 Observations

MaNGA observations use half of the dark time at APO, with the other half taken by the extended Baryon Oscillation Spectroscopic Survey (eBOSS; Dawson et al. 2016; Morganson et al. 2015; Clerc et al. 2016). To ensure full coverage between initial fibre locations, MaNGA observations are made in a three-point dither forming an equilateral triangle. Each exposure takes fifteen minutes, and repeated observations are required to reach an overall minimum signal-to-noise ratio of 5 $\mathrm{\AA}^{-1}$ per fibre at 1.5 R_e in the r band. Each set of exposures is required to have consistent seeing at 2 arcsec or better. On average, this requires 3.3 sets of three exposures per plate. The full details of the observing strategy based on considerations of the hardware is described by Law et al. (2015).

2.1.4 The Data Reduction Pipeline (DRP)

The raw spectrum from each fibre and each exposure is flux-calibrated to better than 5% accuracy as detailed by Yan et al. (2016b). The individual spectra from all fibres of an IFU are then reduced and combined into a three-dimensional datacube by the Data Reduction Pipeline (DRP), which is described by Law et al. (2016).

The DRP performs sky subtraction — which is particularly important for the outskirts of galaxies where there is low observed surface brightness — using the 92 sky fibres located on each plate. The main sky lines impinging on the spectrum are located redwards of $\sim$ 8000 Å. Each of the sky-subtracted spectra of a single galaxy are then combined and constructed into a datacube, for which the astrometry is typically accurate to within 0.1 arcsec. The resulting spatial point spread function (PSF) in the datacube has a Gaussian profile with a median full width at half maximum (FWHM) of 2.54 arcsec.

As well as constructing a flux datacube, the DRP also provides other measurements, such as a corresponding datacube of each pixel's inverse variance in its flux ("`IVAR`"), a mask cube to denote any pixels for which data reduction failed, and a measurement of the line-spread function (LSF) cube.

2.1.5 The Data Analysis Pipeline (DAP)

A Data Analysis Pipeline (DAP) — described by Westfall et al. (2019) — provides high-level analysis products of each MaNGA observation. These include measurements of stellar and gas kinematics, emission-line strengths and equivalent widths, and various spectral indices resolved across the galaxy. These data products are acquired through extensive use of the fitting routine `pPXF` (Cappellari & Emsellem, 2004), concurrently fitting the continuum and stellar absorption lines with stellar template spectra from the MILES library (Sánchez-Blázquez et al., 2006; Falcón-Barroso et al., 2011) and an emission-line spectrum using a series of Gaussian profiles. Any choice of stellar template library has potential to induce bias in the measurements of absorption-line features (and therefore also emission-line strengths and widths when lines and continuum are fitted simultaneously as in the DAP), but Belfiore et al. (2019) showed that these systematic effects are generally smaller than the noise in the MaNGA spectra.

2.2 Galaxy Zoo:3D

One of the aims of any large integral-field spectroscopic survey is to understand how the gas and stellar properties — such as kinematics, metallicities and elemental abundances, electron temperature, ionisation parameters, star-formation histories, and many others — vary systematically between the different distinct components of galaxies. To do so, it is necessary to identify which spatial regions of each IFS datacube correspond to the different galaxy components such as bulges, disks, spiral arms, and bars. The separation between bulge and disk regions can be done in an automated fashion with elliptical profile fitting, using packages such as `Galfit` (Peng et al., 2002). For example, Simard et al. (2011) published a catalogue of two-dimensional bulge+disk decompositions of $> 10^6$ SDSS galaxies using r- and g-band imagery with which it is straightforward to identify these components in MaNGA observations. This decomposition can also be done from the galaxy's kinematics (Tabor et al., 2017, 2019).

By contrast, automatic identification of non-axisymmetric structures such as spiral arms and bars is a significantly more difficult problem to solve, and has not yet been performed for many galaxy surveys. A notable exception is the Spiral Arc Finder and Reporter (SpArcFiRe; Davis & Hayes 2014) tool, which can successfully measure parameters relating to the number, winding, and length of spiral arm "segments" in large numbers of spiral galaxies. However, SpArcFiRe is not reliably able to directly

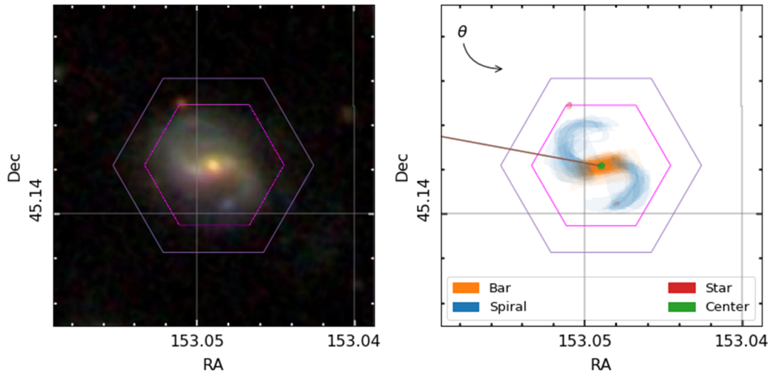

Figure 2.6: In Galaxy Zoo:3D, users are shown a galaxy image (*left*), and asked to draw on regions corresponding to the spiral arms, bar, any foreground stars, and the galaxy's centre. The resulting maps of users' vote (*right*) can be used to differentiate between the non-axisymmetric components of the galaxy in a MaNGA datacube.

extract the image *regions* corresponding to spiral arms, and crucially requires human verification to remove false positives in the identification of individual arms (Hart et al., 2017a).

Instead, an alternative approach being developed specifically to solve this problem for galaxies in the MaNGA survey is to use the assistance of up to hundreds of thousands of volunteer "citizen scientists" as part of the Galaxy Zoo:3D project. Such an approach reduces the net time required to visually inspect each individual galaxy (with repeated classifications for reliability) to the point that developing a fully automated solution becomes unnecessary. "Citizen science" has been applied to morphological classifications of many galaxies as part of the Galaxy Zoo project (Lintott et al., 2008, 2011) and since to many other projects as part of the Zooniverse platform[1].

Galaxy Zoo:3D[2] (GZ:3D; Masters et al., in preparation) is an ongoing project on the Zooniverse platform. Volunteer users are shown images of galaxies in the MaNGA target catalogue and are asked to draw boundaries marking the edges of spiral arms and bars, as well as identifying the position of the galactic centre and any foreground

[1] www.zooniverse.org
[2] www.zooniverse.org/projects/klmasters/galaxy-zoo-3d/classify

stars. The end result is an image with defined spiral and bar weights at each position, determined by the number of users who designated that position as part of a spiral arm or a bar, as shown in Figure 2.6. We make use of the spiral arm masks from GZ:3D in Chapter 3 and more significantly in Chapter 4.

2.3 Spectral fitting with Starlight

There are several publicly-available tools to fit an input spectrum with a set of template spectra. Since each of these packages tries to combine a set of template spectra to match an input spectrum, the choice of fitting routine should in theory have no effect on the measured results. However, some recent studies (e.g. Ge et al. 2018) appear to suggest that this is not quite true in some situations. In any case, the choice of which of the well-established and fully-tested tools to use is somewhat arbitrary, although they each have slightly different design specifications. The following have all been used for modelling MaNGA data:

- The Penalised PiXel-Fitting (pPXF; Cappellari & Emsellem 2004; Cappellari 2017) code was designed to provide extremely robust kinematic measurements, and also measures stellar population compositions.
- Starlight (Cid Fernandes et al., 2005) was designed for accurate recovery of stellar populations in any application. Its flexibility has led it to be used in a range of settings, including at different redshifts.
- Pipe3D (Sánchez et al., 2016a) was developed as an adaptation of the earlier FIT3D (Sánchez et al., 2006). As with Fitting IteRativEly For Likelihood analYsis (firefly; Wilkinson et al. 2015, 2017), it was specifically designed for application to integral-field spectroscopic data.

It is worth noting that there are several other full spectral fitting codes available. For example, STECMAP/STECKMAP (Ocvirk et al., 2006b,a), VESPA (Tojeiro et al., 2007), ULySS (Koleva et al., 2009), and more recent innovations such as Bayesian Analysis of Galaxies for Physical Inference and Parameter EStimation (bagpipes; Carnall et al. 2018), Code Investigating GALaxy Emission (CIGALE; Boquien et al. 2019), and SNITCH (Smethurst et al., 2019) would all — in principle — be applicable to MaNGA datacubes, as would the GIST pipeline (Bittner et al., 2019), which is a new implementation of pPXF specifically designed for IFU datacubes.

However, for the vast majority of the spectral fitting work contained in this thesis, we use Starlight to measure stellar populations. This decision was made for the following main reasons:

1. Unlike many stellar population fitting algorithms (e.g. bagpipes, CIGALE, SNITCH), we do not wish to impose any assumptions on the shape of the star-formation history that we wish to measure. Starlight is fully non-parametric, and also does not limit the "smoothness" of any derived SFH through the use of regularisation, unlike the normal setup of pPXF for example. The implications of this detail are discussed in later chapters.

2. Although they were well-tested on launch, Pipe3D and firely are comparably newer, so had not yet been applied in many instances when the work here was started.

3. Starlight is specifically designed for robust population analysis, rather than primarily for studying kinematics.

4. Starlight has a flexible configuration which can easily be altered. For example, it is able to fit spectra using an irregular grid of template spectra, whereas pPXF is not in its standard setup.

5. MaNGA's continuum is well-calibrated, and its long wavelength range potentially contains stellar population information. Starlight fits this continuum shape as well as all absorption features, unlike `pPXF`.

6. Although other fitting tools can be significantly faster than Starlight (see e.g. Ge et al. 2018, 2019), we have access to the University of Nottingham High Performance Computing facility (Minerva/Augusta), so this is not a significant concern.

7. Starlight has already been successfully applied to study the spatially-resolved fossil record in integral-field spectroscopic galaxy surveys (Pérez et al., 2013; Cid Fernandes et al., 2013, 2014; García-Benito et al., 2019; González Delgado et al., 2017; Mallmann et al., 2018).

Starlight builds a model spectrum using Monte Carlo methods, first sampling a broad range in parameter space before narrowing to a detailed fit. Some aspects of how this is achieved are further discussed in Chapter 5, but the full details of its spectral fitting method is described by Cid Fernandes et al. (2005).

2.4 Single stellar population (SSP) template spectra

A key input in stellar population modelling with any spectral fitting programme is the set of template spectra. Most studies of fitting galaxy spectra make use of single stellar population (SSP) models. A single SSP spectrum represents how a model population of stars — all with a given chemical composition (usually a single metallicity parameter but occasionally more complex; see Vazdekis et al. 2015) — appears after a given time interval since an idealised instantaneous star-formation burst. These spectra are

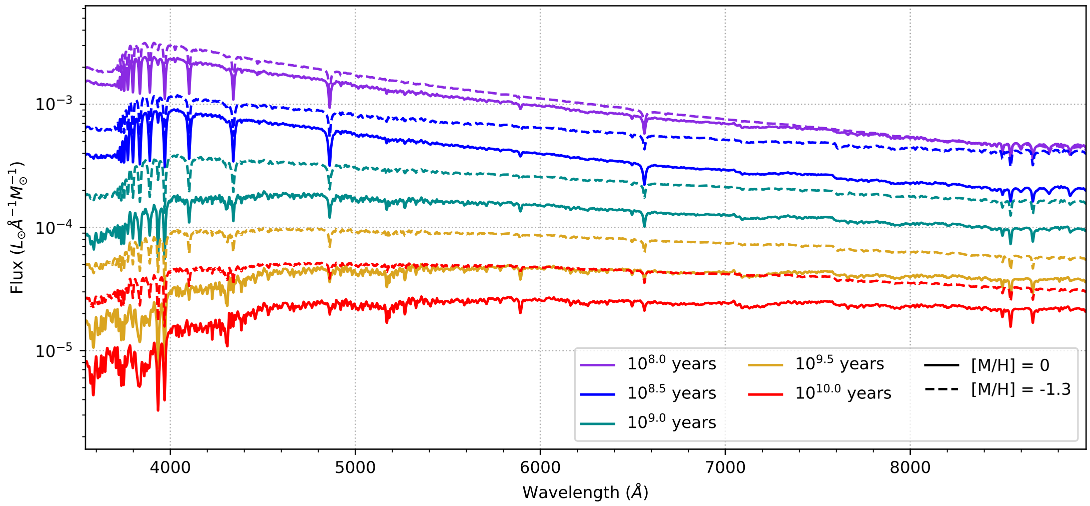

Figure 2.7: SSP spectra from the E-MILES library (Vazdekis et al., 2016) for populations of different ages (denoted by different colours) at solar (solid lines) and twentieth-solar (dashed lines) metallicities.

built from observed spectra of stars, combined with a model isochrone (defining the distribution on the Hertzsprung-Russell diagram of stars of the given age) and an initial mass function (IMF). Each of these ingredients suffers from uncertainties (see Conroy 2013 for a review), so the choice of which template library to use can affect any scientific results (e.g. MacArthur et al. 2004; Conroy et al. 2009, 2010; Cid Fernandes et al. 2014; Ge et al. 2019; Belfiore et al. 2019).

However, despite small uncertainties and discrepancies between model libraries, there is agreement on how a general SSP spectrum changes as a function of population. Examples of stellar population spectra of different ages and metallicities are shown in Figure 2.7. The continua of the youngest templates appear brighter and bluer than the oldest ones, and the absorption features show strong trends with age and metallicity. The spectra shown are from the E-MILES library (Vazdekis et al., 2016), which are an extension of the earlier MILES library (Vazdekis et al., 2010; Falcón-Barroso et al., 2011). Further details on these libraries are discussed in later chapters.

2.4.1 MaStar

The template and test spectra in any spectral fitting routine should be observed in as similar ways as possible, to reduce any unintended side-effects of systematic uncertainties in flux calibration or spectral resolution (Conroy & Gunn, 2010). Ideally, this means that the spectrum to be modelled should be observed using the same instrument under the same conditions as the spectra used to build the SSP models. In practice, this is almost never achieved.

To solve this problem for MaNGA, MaStar (Yan et al., 2019; Aguado et al., 2019) is an ongoing project to obtain stellar spectra using the MaNGA instrumentation by "piggybacking" onto SDSS-IV APOGEE-2N (part of the APO Galactic Evolution Experiment, a major programme of SDSS-IV obtaining high-quality NIR stellar spectra; Blanton et al. 2017; Majewski et al. 2017) observations during bright time at APO. When this project is complete, it will be possible to build stellar population templates with nearly-exactly matching quality to the MaNGA galaxy spectra. At the time of writing, templates with only a limited range of stellar population ages have been created (Maraston et al., 2019).

Chapter 3

A direct test of the quasi-stationary density wave model of spiral structure in a grand design galaxy

As a pilot study to see what can be done with the integral-field spectroscopic data from MaNGA, in this chapter we make use of spectral fitting to investigate how stellar population analysis can help to understand spiral structure in a grand-design spiral galaxy.

The exact nature of the arms of spiral galaxies is still an open question (Dobbs & Baba, 2014), but the leading model is that they are the products of density waves that propagate around the disk, with the spiral arms being visibly enhanced by the star formation that is triggered as the passing wave compresses gas in the galaxy disk (Roberts, 1969; Bertin, 2014). To avoid the "winding problem", whereby a radially-varying wave angular speed causes the spiral arms to wind up over short timescales, a persistent wave must propagate with an approximately radially-invariant angular speed, its pattern speed Ω_P. Testing this model of such a "quasi-stationary" density wave arm therefore ideally requires measurements of the radially-dependent pattern speed $\Omega_P(r)$, which is difficult to achieve. In this chapter, we outline a novel technique using stellar population analysis to infer $\Omega_P(r)$ and test the quasi-stationary density wave model in a grand-design spiral galaxy.

3.1 Introduction

The hypothesized existence of quasi-stationary waves is based on the large number of "open" spiral patterns seen in nearby galaxies, implying that spiral structure is unlikely to change significantly on short timescales. Solutions and models of the nature of such constant spiral arms emerged from work in the 1960s on self-exciting density waves in stellar and gaseous disks (Lin & Shu, 1964, 1966; Kalnajs, 1965). With this came the realisation that the prevalence of long-lived large-scale spiral arms in galaxies means that a single global spiral mode dominates the process (Toomre, 1969; Bertin et al., 1989), primarily driven by the gas dynamics of the disk (Bertin & Lin, 1996). As such a global density wave propagates coherently around the galaxy triggering star formation where it compresses gas, whereby it should create a quasi-stationary spiral pattern across the face of disk galaxies (Bertin, 2014; Zhang, 2016).

In theory, the quasi-stationary nature of the density wave model can therefore be tested by measuring Ω_P and showing that it does not vary with radius in the galaxy. Unfortunately, this measurement is difficult because Ω_P is only indirectly connected to observables such as the stellar rotation speed (Tremaine & Weinberg, 1984; Font et al., 2011; Beckman et al., 2018). However, an alternative approach is to measure the combined effects of the stellar rotation and the pattern speed on the distribution of stellar populations around the galactic disk. In a quasi-stationary model of spiral waves, the stars and gas which comprise the inner part of a galactic disk rotate faster than the spiral pattern speed. In this region, gaseous material entering the concave edge of the spiral density wave will compress and cause a burst of star formation (Roberts, 1969; Gouliermis et al., 2017; Schinnerer et al., 2017). These new stars continue to move ahead of the spiral arm with the older stellar and remaining gaseous material, retaining their spiral structure for a short while before being mixed into the disk (Egusa et al., 2011). Outside a certain radius (known as the corotation radius, denoted here by R_{CR}), material orbits the galactic centre at a slower rate than the pattern speed thanks to a combination of the material's rotational velocity $\Omega(r)$ gradient and a fixed pattern speed, and so gas compression is expected to occur when the convex edge of the spiral arm sweeps through the gaseous disk. Young stars are then left behind the concave spiral arm edge.

As time progresses, stars which formed at the peak of the density wave will therefore move away from spiral arms at a rate that depends on the relative speeds of stars and wave. Thus, the offset between such stars and the current location of the density wave provides a direct measure of the speed at which this wave is propagating. Using such offsets to determine pattern speeds is not new: it has been employed to good effect using the observed offset between the dense molecular gas that is currently being compressed by the spiral wave and young hot stars that formed previously in the spiral arm and have now moved from the peak of the wave (Egusa et al., 2004; Tamburro et al., 2008; Egusa et al., 2009), including in the Milky Way (Dias et al., 2019). The resulting colour gradient across an arm has also been used to the same effect (Gonzalez & Graham, 1996; Puerari & Dottori, 1997; Martínez-García et al., 2009; Martínez-García & González-Lópezlira, 2013; Miller et al., 2019; Abdeen et al., 2020).

Material passing through the spiral arm at its angular speed $\Omega(r)$ will travel around the galaxy by an angle of $\theta_{\mathrm{m}}(r)$ over a time interval $\delta\tau$, since

$$\Omega(r) = \frac{\theta_{\mathrm{m}}(r)}{\delta\tau}. \tag{3.1}$$

If this material contains an imprint of the effects of the spiral arm — for example young stars which were formed at the peak of the density wave — then it will trace the spiral structure, but offset by $\theta_{\mathrm{m}}(r)$ from where the arm affected this material. However, over the same time interval $\delta\tau$, the arm itself will have also moved around the disk by a small angle $\theta_{\mathrm{P}}(r)$ due to the pattern speed, as

$$\Omega_{\mathrm{P}}(r) = \frac{\theta_{\mathrm{P}}(r)}{\delta\tau}, \tag{3.2}$$

so from the observed angle offset $\delta\theta(r)$ between any two tracers

$$\Omega_{\mathrm{P}}(r) = \Omega(r) - \frac{\delta\theta(r)}{\delta\tau}, \tag{3.3}$$

as outlined by Egusa et al. (2009). The presence of the spatial offsets between spiral structure seen in different tracers identified in the above previous works lends some weight to some form of a density wave model of spiral structure. However, in these previous analyses the offset in time between the two phases $\delta\tau$ — essentially the timescale for star formation — was also unknown, so had to be solved for simultaneously. The price paid for deriving this extra parameter was that Ω_{P} had to be assumed to be constant with radius, preventing such a method from being used as a test of the quasi-stationary nature of the density wave picture.

However, we have now reached a point where the quality of optical spectroscopy and the associated modelling techniques allow one to extract a stellar population of a specified age from spectral data, so that Ω_{P} can be measured as a function of radius to see how constant it really is. In this chapter, we use the detailed information on stellar populations of the grand-design spiral galaxy UGC 3825, extracted from spectral mapping, to measure the offset between young stars of a known age and the current location of star formation occurring in the spiral arm in which they formed, allowing the first direct measure of Ω_P at a range of radii.

3.2 UGC 3825

As a test case, we have selected the galaxy UGC 3825 (MaNGA plate-IFU 8132-12702). This isolated (Verley et al., 2007b; Argudo-Fernández et al., 2015) system has a symmetric grand-design structure, which makes it a prime candidate for being the product of a global density wave of internal — rather than tidal — origin (Bertin, 2014; Pettitt et al., 2017; Aramyan et al., 2017). It also does not contain a bar or a significant bulge (Karachentsev & Karachentseva, 2019), which might complicate the interpretation of its spiral structure, and it is at an ideal intermediate inclination to the line of sight at 28° according to the NASA-Sloan Atlas (NSA; Blanton et al. 2011) axis ratio measurements (assuming that the galaxy is an intrinsically flat circular disk), allowing us both to identify its spiral structure and to measure the rotational motion of material via the Doppler shift. At $10^{10.56} M_{\odot}$ it is a relatively high-mass spiral galaxy lying within the blue star-forming main sequence ($g - r = 0.56$) according to photometric measurements from the NSA (Blanton et al., 2011). It also has a low redshift of $z = 0.0276$, so it was observed with MaNGA's largest 127-fibre IFU, thereby providing simultaneous detailed spatial and spectral information.

3.3 Analysis Methods

To measure the pattern speed $\Omega_P(r)$ using Equation 3.3, spiral structure must be measured in two tracers with a known associated time interval $\delta\tau$, and the radially-dependent angular offset $\delta\theta(r)$ must be measured between them. Finally, the velocity of material through the arms $\Omega(r)$ must also be determined.

3.3.1 Spectral Fitting

At each location across the face of the galaxy, we decompose the MaNGA spectrum into the contributions from stars of differing ages and that from current star formation, allowing us to map the distribution of all these various components. For this, we use a combination of two spectral fitting software packages; `pPXF` (Cappellari & Emsellem, 2004) and Starlight (Cid Fernandes et al., 2005). We fit each spaxel's spectrum individually to ensure that we retain all of the spatial information possible. This will result in a decreased signal-to-noise per Ångstrom (SNR) at the edges of the galaxy, but within the region of interest in the galaxy's disk, no spaxel has a SNR less than 5. Any noise on a pixel-by-pixel level is smoothed out later when we measure offsets; we only consider variations in a population's flux on large scales of many spaxels combined. More detail on the effects of low signal-to-noise on the fitting results are discussed later in Chapter 5.

3.3.1.1 Template Spectra

Each spaxel's spectrum of UGC 3825 was fitted using a set of 270 single stellar population (SSP) template spectra from the MILES project (Vazdekis et al., 2015). The MILES templates have a wavelength range similar to MaNGA (3540 Å to 7410 Å),

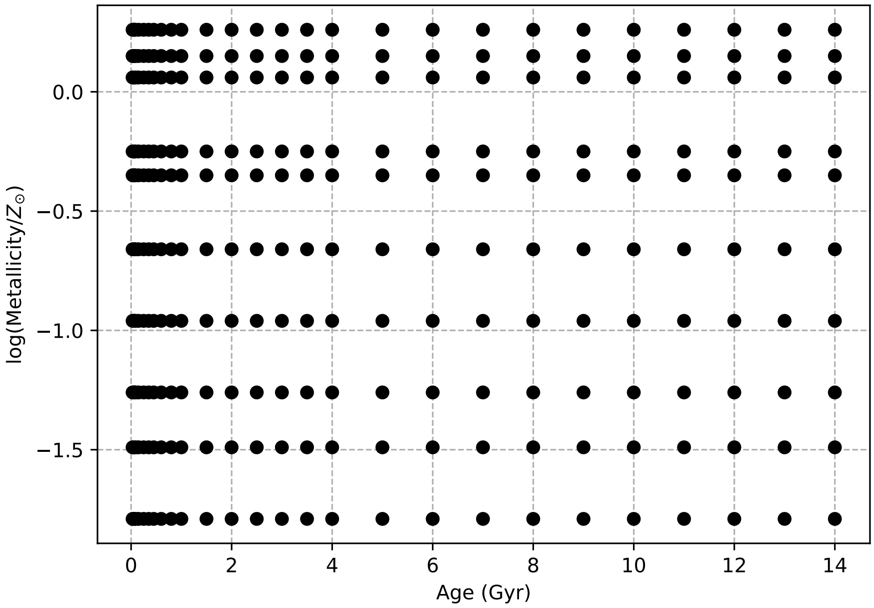

Figure 3.1: The adopted set of SSP template spectra used in fitting. Black points indicate the location in parameter space of SSPs from the MILES library.

with SSPs available for a large number of different ages and metallicities. We use templates covering a wide range of ages (27 values between 3×10^7 ($\approx 10^{7.5}$) years and 13×10^9 ($\approx 10^{10.1}$) years) and metallicities (10 values of [M/H] between -1.79 and +0.40) as indicated in Figure 3.1. Such fine sampling of the age parameter space is employed to achieve the temporal resolution needed to separate out the young stellar components sought in this analysis; the coarser sampling in metallicity is entirely adequate for this work while keeping the total number of templates within the maximum that the software can process. We assume a Kroupa (2001) revised stellar initial mass function (IMF) with "BaSTI" isochrones (Pietrinferni et al., 2004).

3.3.1.2 Measuring Hα flux

As a first step to extract and remove emission-line contributions from the spectra, `pPXF` (Cappellari & Emsellem, 2004; Cappellari, 2017) was used to simultaneously fit the shape and kinematics of both the stellar spectra and a full set of emission lines, whose profiles were assumed to be Gaussian. The resulting Hα emission-line flux measurements provide the tracer of ongoing star formation, since Hα luminosity $L_{\mathrm{H}\alpha}$ is directly proportional to the local star-formation rate (Kennicutt, 1998).

3.3.1.3 Deriving star-formation histories

The spectra were initially logarithmically binned to allow the kinematics to be derived. After the emission lines had been subtracted out, the remaining stellar spectra were rebinned to a linear scale and fitted using the Starlight (Cid Fernandes et al., 2005; Asari et al., 2007) code that is optimised for modelling stellar populations. To reproduce the observed spectra in the fitting process, we also allowed for dust obscuration using a variable-strength Cardelli et al. (1989) reddening law.

The resulting output from Starlight provides the contribution of each SSP of specific age and metallicity to the spectrum at each location across the face of the galaxy. Thus, we are now in a position to create maps showing how stars with differing properties contribute to the total light of the galaxy. In this case, we are interested in mapping out the young stars, so we extract the contribution from all the SSPs with ages of less than 6×10^7 years.

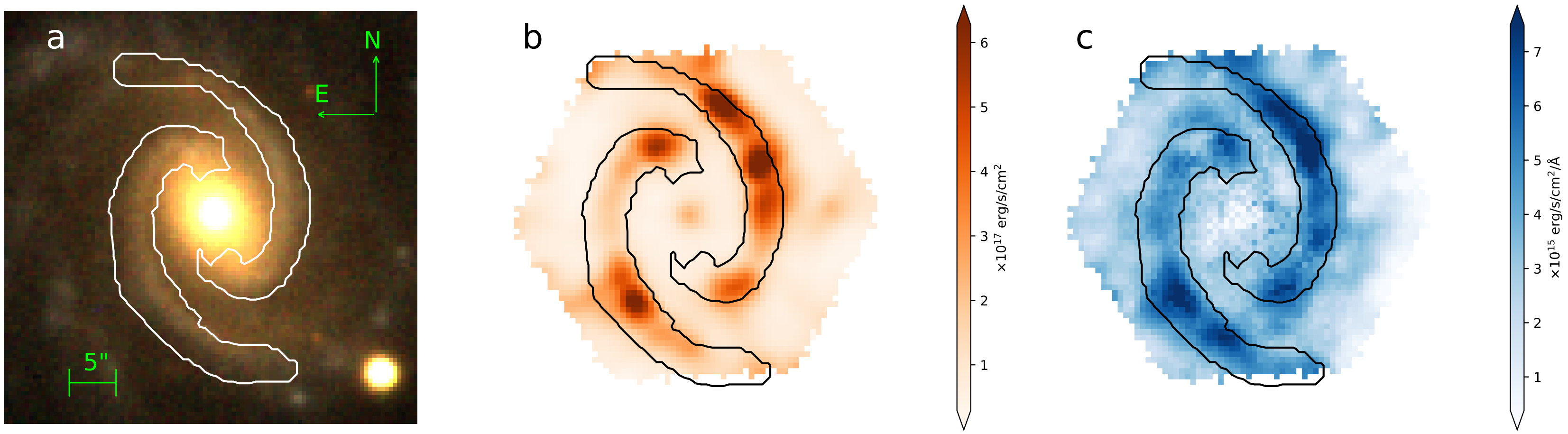

Figure 3.2: UGC 3825 and its star formation tracers used here. *a*: SDSS imagery (Fukugita et al., 1996), showing 5 arcseconds for scale. *b*: Ongoing star-formation, traced by the Hα emission line. *c*: 4020 Å flux of young ($\leq 6 \times 10^7$ years) stars. In each panel, the outline denotes the region within which at least 25% of Galaxy Zoo:3D users agreed on the presence of a spiral arm.

3.3.2 Spiral arm tracers

Figure 3.2 shows the resulting distribution of Hα emission (representing regions of ongoing star-formation) and the map of young ($\leq 6 \times 10^7$ years) stars. As a fiducial, the figure also shows the location of the spiral arm regions determined as part of the ongoing Galaxy Zoo:3D (GZ:3D) citizen science project (see Section 2.2), although this information on the locations of the arms is not required or used in the analysis here. For UGC 3825, 8 users drew spiral arms, so the fiducial in Figure 3.2 is a contour denoting the contiguous region where at least 2 users defined as being part of the spiral arms.

The resulting $L_{\mathrm{H}\alpha}$ map is consistent with that measured using similar methods by the MaNGA DAP (Westfall et al. 2019; Belfiore et al. 2019; see Section 2.1.5) and the overall results do not change depending on which measurements are used. The broad agreement in the shape of the two spiral tracers — despite the emission-line information being removed before performing the Starlight fits — provides some confidence that the spectral fitting methods are measuring what we require. It is also worth noting that the structure within the arms in both tracers is at the ≈ 2.5 arcsec level, which is the MaNGA PSF. Fitting each spaxel independently therefore does not introduce significant spaxel-to-spaxel noise over the level of the intrinsic signal.

3.3.2.1 Determining the time offset $\delta\tau$

The youngest SSP template age used in the fit is 3×10^7 years, but the fitting process will attribute all younger stars — which we know exist thanks to the presence of ongoing star formation indicated by the Hα emission-line map — to this population as well. We therefore assume that this very youngest template's 'true' age is approximately half of this age, 1.5×10^7 years, and all other templates' weights account for stars of their listed age. By weighting by Starlight's fit's template weights, we find the mean age of all stars younger than 6×10^7 years over the entire MaNGA field of view to be 1.9×10^7 years. Due to the assumptions in estimating the effective age of the youngest template, we conservatively assign an uncertainty in this age as 1.0×10^7 years. The peak in Hα emission occurs very soon after the onset of star-formation, and hence the temporal offset between the young population and the Hα emission is $\delta\tau = 19 \pm 10$ Myr.

3.3.2.2 Determining the angular offset $\delta\theta(r)$

Even in these raw maps shown in Figure 3.2, it is discernible that over most of the galaxy the young stellar population is found on the leading edge of the spiral arm. This is what one would expect from the spiral density wave picture, as the material in the inner parts of a galaxy is predicted to circulate at a higher angular velocity than the spiral pattern, so gas clouds overtake the arms and collapse to form stars in the density wave. These young stars continue to overtake the spiral arm to emerge out of the leading edge after a time interval determined by the difference between the pattern and material speeds, as defined in Equation 3.3.

We can render this description more quantitative by measuring the small angular offset in azimuth between these two spiral arm tracers as a function of radius, $\delta\theta(r)$, by cross correlating data from the maps of current star formation and the young stellar population. As a first step, we deproject the maps to face-on using centre coordinates, inclination, and position angle measurements determined from the best-fit parameters to the gas disk kinematics,[1], and convert the Cartesian images to polar ones, binned in radius with a step-size of $\Delta r \approx 0.16$ kpc. When the NSA measurements are used instead for the centre, inclination and position angles (assuming the galaxy disk is intrinsically a flat circular disk), the results are unchanged.

[1]These measurements were made using a method similar to that of Andersen & Bershady (2013) which was implemented on the MaNGA observations of UGC 3825 by K. Westfall in work not yet published.

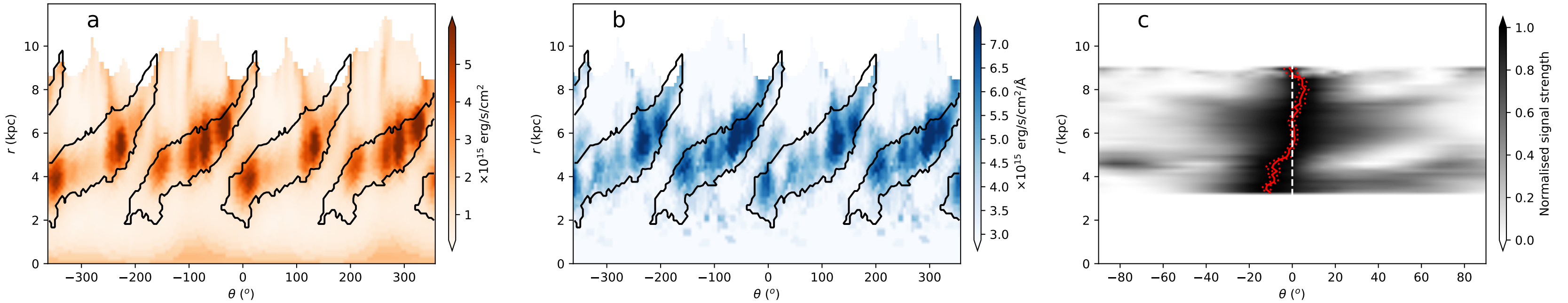

Figure 3.3: Cross-correlating allows us to determine the angular offset between the two tracers. Polar-coordinate maps of the Hα emission line and young stars from Figure 3.2 are shown in *a* and *b*. The galactic centre is at the bottom of the map, and the black outlines indicate the location of the same GZ:3D spiral arm mask shown in Figure 3.2. The cross-correlation signal between these maps is also shown in *c*, with the cross-correlation angle $\delta\theta(r)$ shown as a red line. The red dotted line indicates the uncertainty in the cross-correlation angle $\Delta_{\delta\theta}(r)$, defined using Equation 3.4.

For each such radius, we determine the offset between the spiral features in the Hα and young stellar map by cross-correlating the signal in the polar maps, displayed in Figure 3.3. The boundary of the polar-coordinate maps at $\pm 2\pi$ is entirely arbitrary and the correlation must "wrap" to ensure that the signal is that of the spiral arms and not that of the image boundary. For this reason, we actually employ a convolution algorithm between the two tracers, which acts as a close proxy for cross correlation with easier handling of the boundary wrapping. The convolution makes use of the convolution theorem, which states that the convolution $f * g$ between two signals f and g can be written as $f * g = \mathcal{F}^{-1}\{\mathcal{F}\{f\} \cdot \mathcal{F}\{g\}\}$ where $\mathcal{F}$ denotes a Fourier transform. We expect a spiral arm enhancement in flux in either tracer to be approximately symmetrical about its maximum at a given radius r, in which case the convolution and cross-correlation methods produce identical results. Regardless, we are only interested in the location of the peak of the convolution/cross-correlation signal, which is unaffected by the symmetry of the spiral arm signals. The location of the maximum in this convolution signal is refined to a sub-pixel value by fitting a 2$^{\mathrm{nd}}$-order polynomial around the peak.

The region of $r < 3.2$ kpc (approximately 0.32 R_{e} using the elliptical Petrosian effective radius measurements R_{e} from the NSA) in Figure 3.3 is ignored when calculating $\Omega_{\mathrm{P}}(r)$ since the azimuthal signal of Hα variations here is found to be too small to reliably measure $\delta\theta(r)$. We also ignore the region of $r > 9$ kpc, as the MaNGA IFU covers less than 50% of the azimuthal range here due to the non-circular boundary.

A conservative estimate for the uncertainty $\Delta_{\delta\theta}(r)$ in this offset can be obtained from the ratio of the full-width-at-half-maximum (FWHM) of the peak in the convolution signal to the signal-to-noise ratio (SNR) of the signal at each radius r. Since there are no regions of the convolution dominated by noise rather than signal, the radially-dependent convolution SNR is in turn estimated as the ratio of the peak height $H(r)$ (i.e. the maximum strength of the cross-correlation signal at r) to the standard deviation of the cross-correlation signal $\sigma_{\delta\theta}(r)$; i.e.

$$\Delta_{\delta\theta}(r) = \frac{\mathrm{FWHM}(r) \times \sigma_{\delta\theta}(r)}{H(r)}. \tag{3.4}$$

The radially-varying FWHM allows the value of $\Delta_{\delta\theta}(r)$ to account for the radial variation in the MaNGA beam size effects in the polar-coordinate plots. At low r, the beam covers a large range in θ. The cross-correlation signal's peak will therefore be proportionally wider, increasing $\Delta_{\delta\theta}(r)$. At large radius, the beam will cover a small range in θ, allowing us to obtain a tighter constraint on the value of $\delta\theta(r)$.

3.3.3 Measuring the angular velocity of circular orbits $\Omega(r)$

The other ingredient needed to determine the pattern speed is the angular speed of material following a circular orbit in the galaxy, $\Omega(r)$. We use gas velocity measurements from the MPL-6 version of the MaNGA DAP to determine the angular velocity of material $\Omega(r)$ since the very young stars this material traces will not yet have been dynamically heated from their purely circular trajectories (Gerssen et al., 1997).

Using the same process as described in Section 3.3.2.2, the gas velocity map can be remapped into polar coordinates, as shown in Figure 3.4. At each radius, the observed line-of-sight velocity will vary sinusoidally with azimuthal angle, and a simple least-squares fit yields the amplitude of this variation at each radius, $V_{\mathrm{gas}}(r)$. This is illustrated for $r = 6\,\mathrm{kpc}$ in Figure 3.4. The angular speed can then be calculated as

$$\Omega(r) = \frac{V_{\mathrm{gas}}(r)}{r \times \sin(i)} \tag{3.5}$$

where i is the inclination angle of the galaxy to the line of sight ($i = 0$ for a face-on galaxy) derived from the galaxy's kinematics in Section 3.3.2.2. The error in Ω is

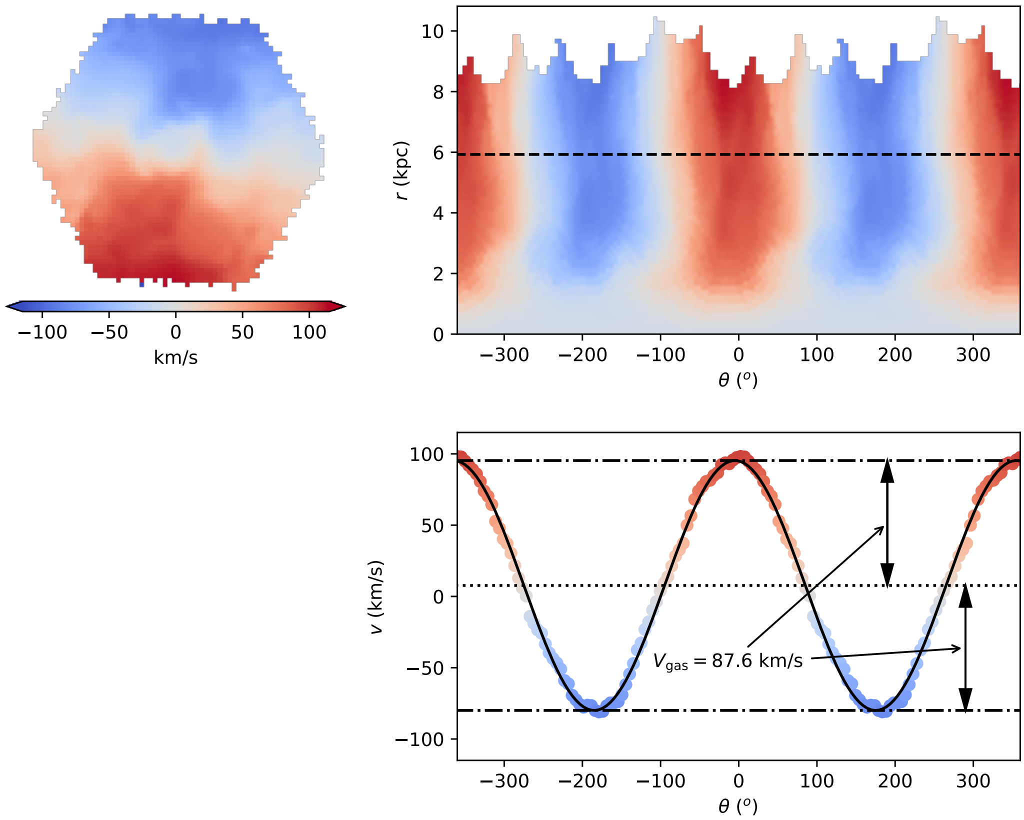

Figure 3.4: The line-of-sight gas velocity map (*top left*) is transformed to polar coordinates (*top right*). At any given radius r (for example $r = 6$ kpc indicated by the dashed line), the velocity variation with azimuth is modelled as a sine wave (*bottom*). The value of V_{gas} at this radius is defined as the amplitude of the best-fit sine wave ($V_{gas} = 87.6$ km/s at $r = 6$ kpc).

dominated by the contribution from the uncertainty in the sinusoidal fit, and so this value is adopted.

3.4 Results

The resulting pattern speed $\Omega_P(r)$ using Equation 3.3 is shown in Figure 3.5. We find that $\Omega_P(r)$ has very little (if any) trend with galactocentric radius r, and within the uncertainties of the complex measurements is consistent with having a constant value of $33\,\mathrm{km\,s^{-1}kpc^{-1}}$. Such constancy was in no way imposed by the analysis, so the result of this analysis for UGC 3825 is therefore entirely consistent with the predictions of a quasi-stationary density wave.

At small radii — as expected from the qualitative analysis of offsets in Figure 3.2 — matter is rotating faster than the derived pattern speed, but eventually the measured angular speed of material drops to where it is rotating at the same speed as the spiral pattern, at the corotation resonance R_{CR}. The location of this resonance in Figures 3.3 and 3.5, at a radius of $R_{\mathrm{CR}} \approx 6\,\mathrm{kpc}$ ($0.6\,R_{\mathrm{e}}$), is broadly consistent with estimates for other galaxies using less direct techniques (e.g. Tamburro et al. (2008) who find that $0.8 \lessapprox R_{\mathrm{CR}}/R_{\mathrm{e}} \lessapprox 2.2$ in most galaxies) and with the predictions for a modal picture of quasi-stationary density waves for which it is expected that $0.6 \leqslant R_{\mathrm{CR}}/R_{\mathrm{e}} \leqslant 1.2$ (Bertin & Lin, 1996; Bertin, 2014).

3.4.1 Testing with an older stellar population

If the picture established here is correct, then it should be possible to repeat the analysis using a somewhat older stellar population that will have had time to travel further from the peak of the spiral density wave. In practice, it appears that the residual spiral

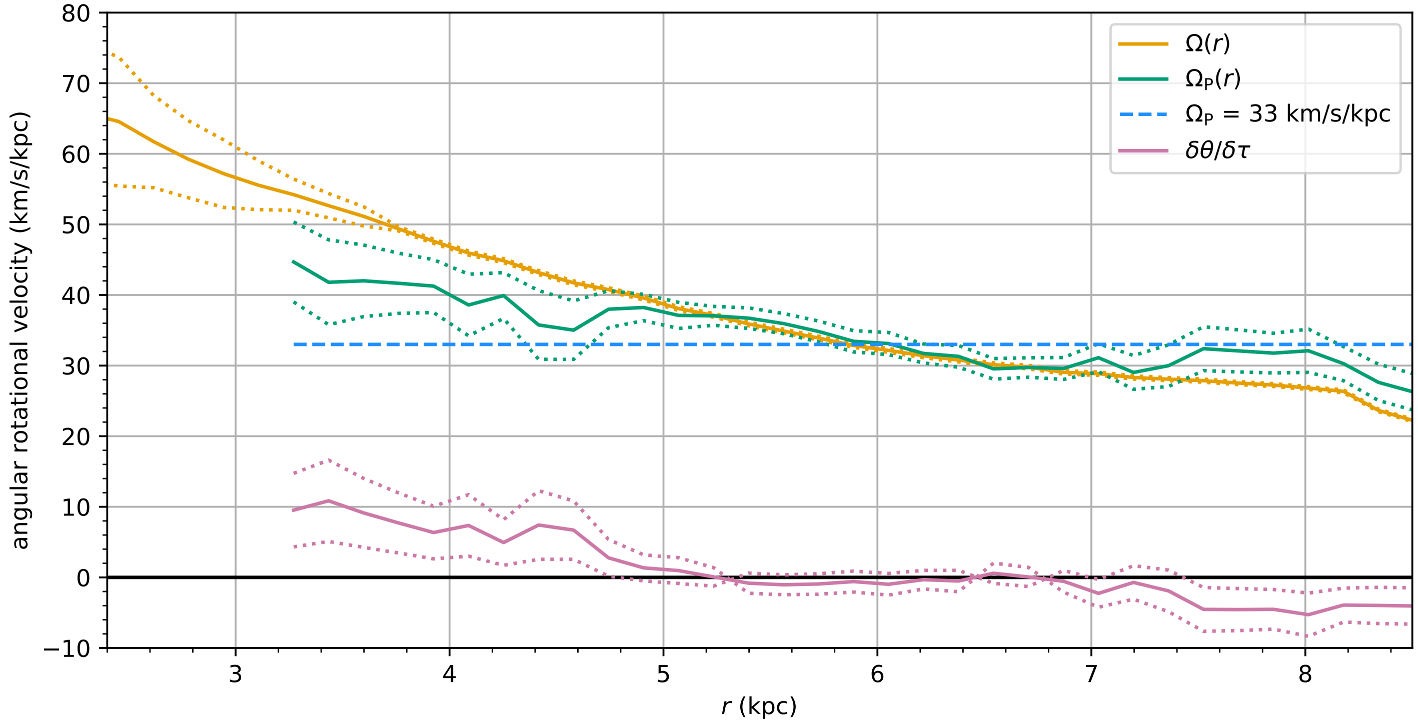

Figure 3.5: The derived pattern speed $\Omega_{\mathrm{P}}(r)$ for UGC 3825 using this method is shown in green. This is the value of $\frac{\delta\theta}{\delta\tau}(r)$ (plum solid) subtracted from the angular velocity of material $\Omega(r)$ (gold solid), as defined in Equation 3.3. The estimated 1 σ uncertainties in these quantities as defined in Sections 3.3.2.2 and 3.3.3 are denoted by dotted lines. The light blue dashed line shows a constant pattern speed consistent with the measured $\Omega_{\mathrm{P}}(r)$. The horizontal axis is limited here to the region where at least 25% of the GZ:3D users agree on the location of the spiral arms. At $r < 3.2$ kpc, the azimuthal change in the Hα emission-line map becomes too unreliable to measure a cross correlation, as explained in Section 3.3.2.2.

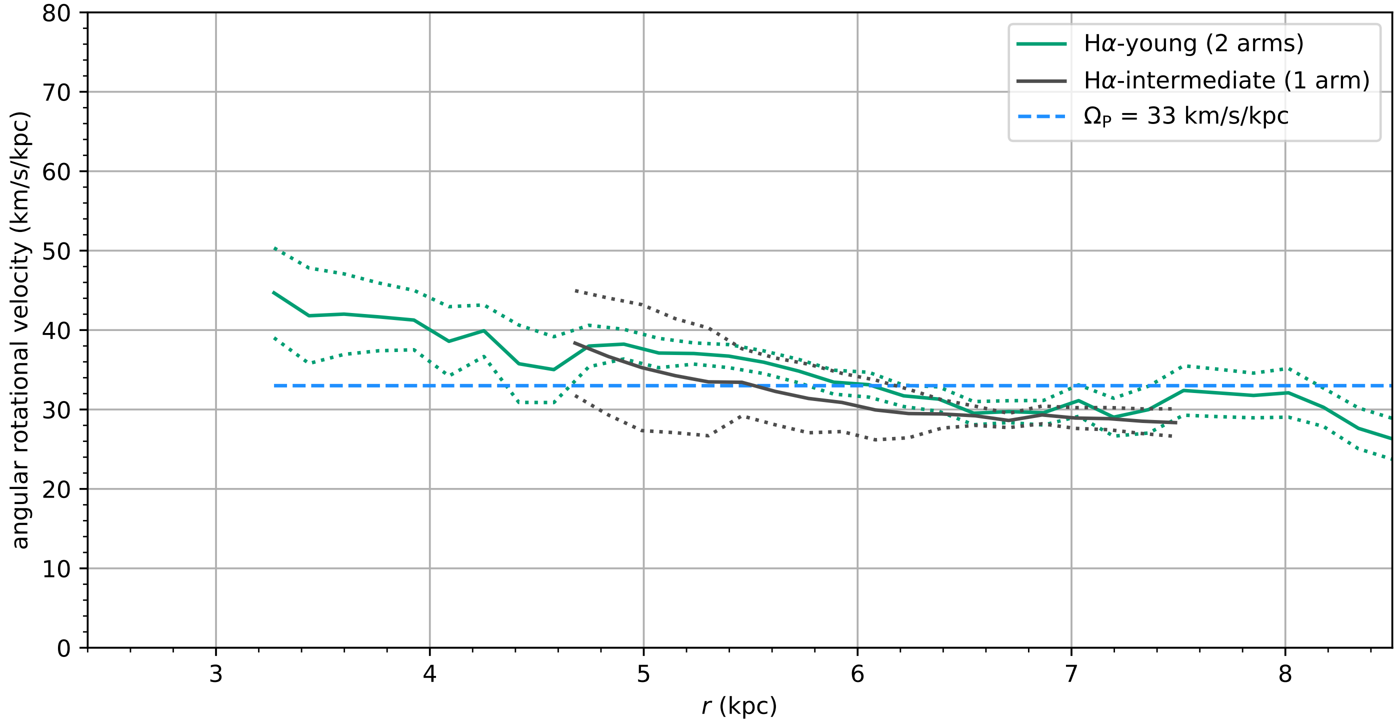

Figure 3.6: As Figure 3.5; $\Omega_\mathrm{P}(r)$ defined as in Figure 3.5 (green solid) with its best-fit flat line (light blue dashed), but also showing $\Omega_\mathrm{P}(r)$ derived from the offset between Hα and the stars of ages 0.2 to 1.3 Gyr in the southern arm (grey). Dotted lines indicate estimated 1 σ uncertainties. The results show clear consistency.

feature fades very rapidly into the noise from the more general disk population, but we were able to extract a consistent signal from a portion of the southern spiral arm for an intermediate-age population combining the templates with ages between 0.2 and 1.3 Gyr. This population is dominated by B- and A-type stars. We find that the flux-weighted average age of these stellar populations is at the very youngest end of this range, due to the strong dependence on stellar age of the population's luminosity. Therefore adopting a luminosity-weighted age of ≈ 0.2 Gyr, the results from the angular offset of these somewhat older stars from the Hα emission-line map — which we have shown in Figure 3.6 — are entirely consistent with the pattern speed derived in Figure 3.5, giving some further confidence in both the method and the model of a quasi-stationary density wave. Similarly, the same cross-correlation method applied between the spiral arms traced by these intermediate-age stars and the youngest stars produces consistent results, albeit with larger uncertainties.

3.5 Conclusions

We have shown that the spiral structure present in different tracers — in this case the Hα emission line representing ongoing star formation, and two stellar populations of different ages — can be measured separately using spectral fitting methods. In UGC 3825, the presence of an offset in the spiral structure between tracers of different timescales since star formation provides evidence for the spiral arms being consistent with a density wave model, and also reassures that the spectral fitting techniques employed here are reliable. We found that the measured spiral pattern speed is entirely consistent with being constant with radius. A coherent story therefore emerges in which the observed spiral structure is consistent with a quasi-stationary internal-origin density wave.

However, it has been suggested (and evidence is making it increasingly clear) that such a model can only explain the spiral structure found in a fraction of all galaxies (Meidt et al., 2009; Hart et al., 2017a; Pringle & Dobbs, 2019). Since different mechanisms for producing spiral arms should result in significantly different radial profiles in pattern speed (Bertin, 2014; Baba et al., 2015), future studies could distinguish between such physical processes using this new technique. Large spectroscopic surveys of galaxies like MaNGA will ultimately allow us to fully determine the circumstances under which galaxy spiral arms are produced by long-lived density waves.

This pilot study confirms that there is a wealth of information contained within the spatial distributions of stellar populations of different ages, motivating a more systematic study of the full star-formation histories first with a single galaxy in Chapter 4, leading to a larger survey in Chapter 6.

Chapter 4

Time-slicing spiral galaxies

Spectra of galaxies contain a wealth of information about the stellar populations from which they are made. With integral-field unit (IFU) surveys, such data can be used to map out stellar population properties across the face of a galaxy, allowing one to go beyond simple radial profiles and study details of non-axisymmetric structure. To-date, however, such studies have been limited by the quality of available data and the power of spectral analysis tools. This chapter makes the case for taking the next step, and studies the barred spiral galaxy MCG+07-28-064 from observations obtained as part of the SDSS-IV MaNGA survey. We aim to highlight that there is a wealth of untapped information on the spatial distribution of star-formation histories (SFHs) available in the current generation of IFU galaxy surveys, and as an example we explore what can be learned about bars and spiral arms when approached in this way.

4.1 Introduction

By analyzing the full spectrum of an unresolved stellar population, it is possible to extract detailed information about the population's star formation history (SFH) by measuring the fraction of stars of different ages present. Early works by Panter et al. (2003), Ocvirk et al. (2006b), Mathis et al. (2006), Tojeiro et al. (2007), Koleva et al. (2009) and others showed that spectral analysis of large low-redshift spectroscopic survey data can reveal information about the evolution of star formation in the Universe back to redshifts of $z \approx 2$.

With the advent of large integral-field spectroscopic surveys such as the Calar Alto Legacy Integral Field Area survey (CALIFA; Sánchez et al. 2012), the Sydney-AAO Multi-object Integral field spectrograph (SAMI; Croom et al. 2012), and MaNGA (Bundy et al., 2015), the populations of different regions of galaxies can be characterised. This can provide a valuable insight into the formation processes and the internal dynamics of galaxies, since these will leave a signature imprint in the stellar populations contained within. González Delgado et al. (2015) showed that the SFHs of galaxies vary with radius and that this has a significant connection to galaxy morphology. They found evidence for inside-out growth of galaxies, an effect which Ibarra-Medel et al. (2016) subsequently found to be strongest in currently star-forming spiral galaxies. This picture will be explored further in Chapter 6. Backing up these findings, Rowlands et al. (2018) also showed that the fractions of stars of different ages residing in different regions of a galaxy are connected to the local gas conditions in the system. Measuring the spatially-resolved SFHs with MaNGA can also help in understanding the known evolution of galaxy populations over cosmic time (Sánchez et al., 2019) as well as the effects of AGN activity on the conditions in the central regions of galaxies (Mallmann et al., 2018).

Statistical studies using large samples of galaxies are useful to help us understand the general evolution and growth of galaxies, but by only measuring variation in the SFHs with galactic radius some subtle details are being "washed out". Most low-redshift disc galaxies host non-axisymmetric structures such as spiral arms and bars (Knapen et al., 2000; Eskridge et al., 2000; Masters et al., 2011), which are likely to affect different stellar populations in different ways. For example, it is known that azimuthal variation in the current star formation rate can arise as a result of the presence of bars (Martin & Friedli, 1997; Verley et al., 2007a) and spiral arms (Chapter 3; Gonzalez & Graham 1996; Puerari & Dottori 1997; Dametto et al. 2019), and so the spatially-resolved fossil record of stellar populations are likely to contain the historical imprints of these structures. Additionally, bars are associated with stable orbits (Contopoulos & Papayannopoulos, 1980; Athanassoula, 1992) and hence flattened stellar population gradients (Fraser-McKelvie et al., 2019), while young stars are often associated with spiral arms (Roberts, 1969).

To gain a more complete picture of the spatially resolved SFHs of disc galaxies beyond the radial variations of previous large-scale works, we should generate two-dimensional maps of stars of different ages and test how these correlate with galaxy components including non-axisymmetric structures. Cid Fernandes et al. (2013, 2014) showed that it is possible to observe the distinct structures of stellar populations of different ages using spectral synthesis of CALIFA datacubes. In this chapter, we explore how similar methods could be reliably applied to a MaNGA datacube in preparation for larger studies, and to then investigate in what ways non-axisymmetric structures vary between the present-day distributions of different stellar populations. The work presented here also discusses whether such an approach can help to understand the dynamics of bars and spiral arms. To this end, a pilot study is presented of full-spectral fitting on a datacube to find the fractions of light and mass in stars of different ages and metallicities. We take care to preserve the full spatial information available in MaNGA, in order to build maps of stars of different ages.

4.2 Galaxy MCG+07-28-064

For the purposes of this exploratory study, we have selected MCG+07-28-064 (MaNGA plate-IFU 8332-12701) as an example galaxy to test the population analysis technique. It serves as an ideal test case galaxy for this purpose, since it shows clear spiral and bar structure and is located in a region with low Galactic extinction ($E(B-V)_{\mathrm{MW}} = 0.014$). According to the NASA-Sloan Atlas (NSA; Blanton et al. 2011), it has a redshift of $z = 0.028$, and a photometry-derived mass of $10^{9.78}\ M_{\odot}$.

As well as being in the MaNGA sample, MCG+07-28-064 is part of the initial sample of galaxies for the Galaxy Zoo:3D programme (GZ:3D; see Section 2.2), providing locations of bar and spiral arm features which we can use in the analysis described here.

4.3 Spectral Fitting

A number of spectral fitting tools are publicly available. As discussed in Section 2.3, we use Starlight (Cid Fernandes et al., 2005), which has previously been successfully applied to analyse stellar populations of CALIFA and MaNGA datacubes (Pérez et al., 2013; Cid Fernandes et al., 2013; Mallmann et al., 2018). For a given input spectrum, Starlight utilises Monte Carlo techniques to find a best-fit combination of template spectra, also allowing for a variable-strength dust extinction.

We apply Starlight to each spectrum in the MaNGA datacube of MCG+07-28-064 using Starlight's "long fit" settings — including long Markov chains and the requirement to retain at least 97% of the fit's total light, for example — which prioritises robustness over speed, as recommended by Ge et al. (2018) and Cid Fernandes (2018). It is common to bin neighbouring spatial pixels ("spaxels") together when fitting to ensure a minimum signal-to-noise. However, to ensure that we are not blending any non-axisymmetric structures into the surrounding disc, we perform the fits on every available spaxel. This results in lower signal-to-noise in individual spaxels in the faint outskirts of the galaxy (the consequences of which are discussed further in Chapter 5) but here we focus only on the brighter bar and spiral arm regions.

We allow Starlight to fit for extinction using a Calzetti (2001) curve, and use a wavelength range for the fit of 3300 to 8900 Å to make greatest possible use of all of the spectral information available in both MaNGA and E-MILES. Since stellar populations of different ages dominate different wavelengths in the spectrum, using such a long range in the fit is essential to constrain the full SFHs.

Starlight does not fit emission lines, so these must either be removed or masked before fitting. Although many authors (e.g. Cid Fernandes et al. 2013) choose to mask them, we make use of the MaNGA DAP emission-line measurements (Westfall et al. 2019; Belfiore et al. 2019; see Chapter 2) and subtract them from our spectra, allowing us to retain and fit all absorption line information which might otherwise be masked. This is particularly important for the Balmer lines, a key age diagnostic. Once the emission lines have been removed, each spectrum is de-redshifted and rebinned onto a linear wavelength base before being fit with Starlight.

4.3.1 Template spectra

The template spectra we use in fitting are synthetic single stellar populations (SSP) from E-MILES (Vazdekis et al., 2016). We use a set of 78 SSPs — indicated in Figure 4.1 — with 14 ages (0.03, 0.05, 0.08, 0.1, 0.2, 0.3, 0.45, 0.7, 1, 1.75, 2.5, 4, 6.5, and 10 Gyr) and 6 metallicities ([M/H] = $-1.79, -1.49, -0.96, -0.66, -0.25, +0.26$), avoiding the six templates (0.03–0.1 Gyr at [M/H] = -1.79, and 0.03–0.05 Gyr at [M/H] = -1.49) which fall outside the recommended safe ranges specified by Vazdekis et al. (2016). We

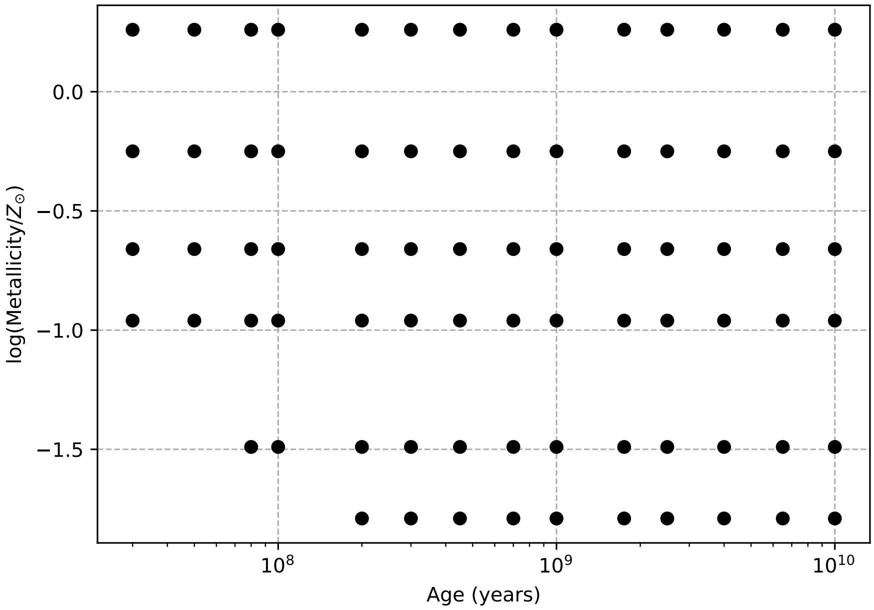

Figure 4.1: The set of SSP template spectra used in fitting in Chapter 4. As in Figure 3.1, black points indicate the location in parameter space of SSPs from the E-MILES library.

have tested how our derived SFHs vary if we include a finer sampling in age and found that reducing the total number of SSPs from the 270 used in Chapter 3 — almost the maximum of 300 allowed in STARLIGHT — to these 78 resulted in entirely consistent results, but significantly reduced computing times. The templates all assume a Kroupa (2001) IMF, Pietrinferni et al. (2004) isochrones, and a Milky Way [α/Fe] ("baseFe"). Before fitting, each of the template spectra have been Gaussian-smoothed to match the wavelength-dependent spectral resolution of the MaNGA spectra.

4.3.1.1 Treatment of α-element enhancement

It is not straightforward to predict how the assumptions made in the fitting processes affect the accuracy of the returned SFHs. An example of this is in the alpha enhancement. This is a measure of the over-abundance of the α-elements (primarily O, Mg, Si, Ca, and Ti) relative to that of iron. Since these α-elements are thought to be formed on short timescales in Type II supernovae while Fe is formed in Type Ia which have longer timescales (Tinsley, 1979), measurements of the variation in $[\alpha/\text{Fe}]$ of individual stars in the Milky Way have been used to study the possible formation sequences (Fulbright, 2002; Nissen & Schuster, 2010) and kinematics (Feltzing et al., 2019) of our galaxy. Varying the alpha enhancement will affect the relative strengths of absorption lines in a stellar population spectrum, and exactly how STARLIGHT might try to adjust its fit to account for the restriction to a single (potentially erroneous) value of $[\alpha/\text{Fe}]$ is uncertain.

Although the E-MILES templates' variation of alpha-enhancement is limited to be Milky Way scaled — in which $[\alpha/\text{Fe}]$ is a function of [M/H] according to observations of the Solar neighbourhood — the earlier MILES models as used in Chapter 3 (which have a shorter wavelength range; Vazdekis et al. 2010; Falcón-Barroso et al. 2011) are also available with solar ($[\alpha/\text{Fe}] = 0$) or alpha enhanced ($[\alpha/\text{Fe}] = 0.4$, which is representative of the most alpha-enhanced stars typically seen in the Milky Way; see for example Nissen & Schuster (2010)). To test how the restriction to a single value of $[\alpha/\text{Fe}]$ for each metallicity biases the results, we performed a test in which the basic SFH of a spectrum obtained using twelve MILES SSPs (4 ages $\times$ 3 metallicities $\times$ 1 alpha-enhancement) was compared with that using 36 SSPs (4 ages $\times$ 3 metallicities $\times$ 3 alpha-enhancements). By comparing the results from each fit, we found that although our resulting metallicity distributions may be affected by limiting the available SSP templates to a single $[\alpha/\text{Fe}]$, the age distributions are unaffected, so we conclude that this assumption does not impact on the measured SFHs significantly.

4.3.1.2 Treatment of young populations

We have also tested adding a set of theoretical templates from González Delgado et al. (2005) covering the range of 1 to 50 Myr to the E-MILES set described above, and found that the SFHs at times greater than 50 Myr to be generally unaffected. To avoid complications and additional uncertainties related to mixing two different population libraries, the results here are using only the E-MILES library. This of course limits the range of ages for which we are able to measure SFHs. A more detailed discussion of work to incorporate these younger templates to probe the structure of populations at a greater range of stellar ages is contained in Chapter 5.

4.3.2 Handling Starlight output data

For each spectrum in MCG+07-28-064, Starlight returns the weight assigned to each template in its best fit at a reference wavelength, in this case taken as 4020 Å. By retaining all of these weights at each position in the MaNGA datacube, we produce a 4D output cube $(x, y, \mathrm{age}, \mathrm{metallicity})$ from the 3D (x, y, λ) MaNGA datacube. Using this output, it is therefore possible to sum the relevant template weights to find the fraction of stars at a specific location within a particular metallicity or age range. Here we use the Starlight SSP weights to build maps of the flux produced by stars of each age, and can also find the mean metallicity of those stars across the face of the galaxy.

There are many uncertainties involved in full spectrum fitting (Conroy, 2013; Cid Fernandes et al., 2014), particularly in the ability to break the age-metallicity degeneracy, although the broad wavelength range of MaNGA spectra helps here. As a result, many spectral fitting tools such as `pPXF` (Cappellari & Emsellem, 2004) include regularisation to force the resulting SFHs to have a smoothed distribution. Since Starlight does not include regularisation, we smooth the grid of SSP weights in the age axis to produce maps of stars of different ages to ensure we are not over-interpreting extremely large or small weights given to a few SSPs (Cid Fernandes et al., 2005; Cid Fernandes, 2018).

It is also worth noting that the metallicity of young stellar populations is not easily determined, since these populations do not show strong metal absorption features. For populations younger than ≈ 0.1 Gyr, Starlight assigns weights to all metallicities approximately evenly, resulting in all populations at these ages to appear to have a mean metallicity of ≈ -0.75.

These issues are explained in more detail in Chapter 5.

4.4 Time slicing

The spectral fitting on the datacube for MCG+07-28-064 can be visualised by the animation shown in Figure 4.2, showing the flux contribution of stars as a function of age in different parts of the galaxy, coloured by those stars' mean metallicity. For each frame, we interpolate over the SSP weights using a Gaussian of width 0.4 dex in age to create a flux map of the stars of each age. We then find the mean metallicity of those stars at each point in the galaxy, which is indicated using the colour of each pixel.

In the animation, stars of varying ages exhibit varying radial and azimuthal structures. The fitting of each spaxel was performed entirely independently, so the presence of any such age-dependent structures provides some confidence in performing spectral fitting in a spaxel-by-spaxel manner. To highlight the importance of retaining the full spatial information from MaNGA, we focus here on the variation of azimuthal structure in populations of different ages.

4.5 Results

To quantify the structural variations seen in Figure 4.2, we generated images of each stellar population time slice (smoothed to 0.4 dex in age), and measured parameters

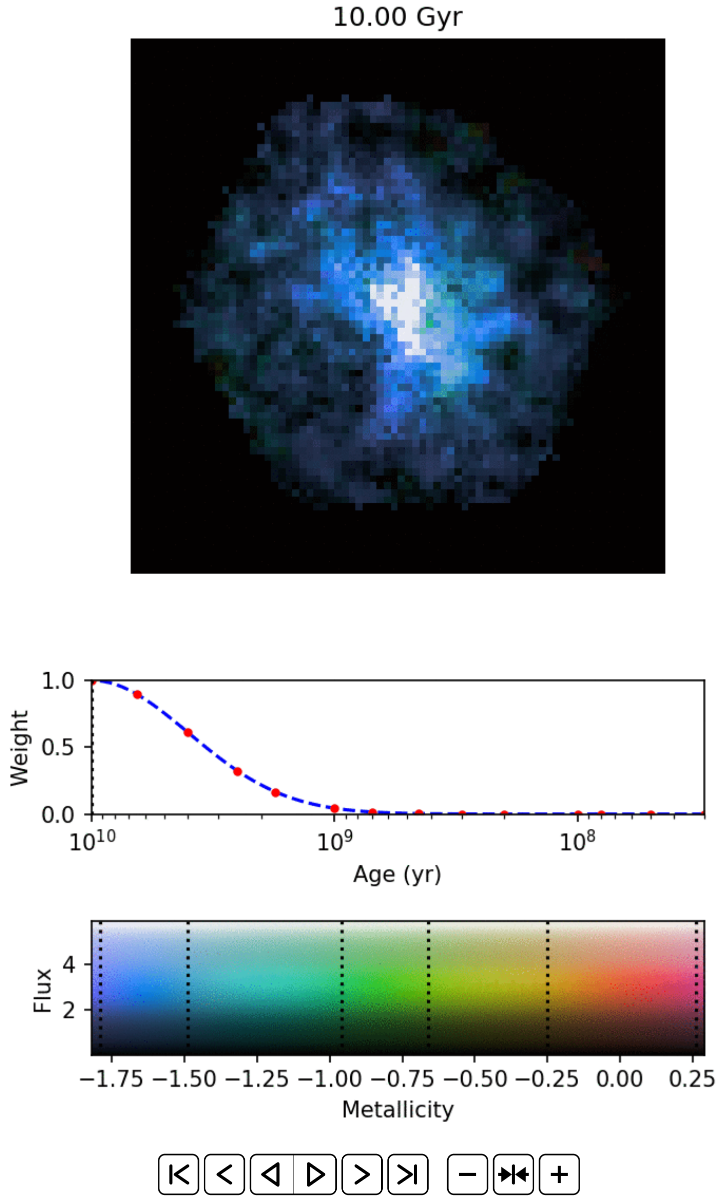

Figure 4.2: *Top*: Animation showing the spatially resolved flux (colour-coded by the mean metallicity) of stars as a function of age, running from 10 to 0.03 Gyr. *Middle*: Weighting function used. In each frame, the STARLIGHT output is smoothed in age using a Gaussian weighting function centred on the frame's age with a width of 0.4 dex. Red points indicate the SSP ages used in the fit. *Bottom*: Colour map indicating the flux (in units of 10^{-14} erg s^{-1} cm^{-2} Å^{-1} spaxel^{-1}) and light-weighted mean metallicity (in units of $\log(Z/Z_{\odot})$) of the stellar population. Dashed vertical lines indicate the SSP metallicities used.
Note that the metallicities of stellar populations younger than ~ 0.1 Gyr are unreliable, since these populations have very few metallicity-related spectral features.

relating to the spiral arms and the bar.

4.5.1 Measuring spiral arm and bar parameters

The bar structural parameters are measured using the Fast Fourier Transform bar analysis method of Kraljic et al. (2012). The presence of a bar is inferred by a strong $m = 2$ Fourier component. The length is inferred by measuring the phase of the second mode, $\Phi_2(r)$, within the bar region. A bar is deemed present if $\Phi_2(r)$ is constant to within $5°$, and the radii that this occurs for correspond to radii at which a bar is present. The length, strength, and angle of the bar are measured for age slices centred on each of the SSP ages used in the fitting. These FFT methods do not intrinsically provide an estimate for the uncertainties in each of the bar length, strength, and angle. We expect that uncertainties in these measurements will be dominated by noise in the time slice images, so we estimate them through a basic bootstrapping approach by measuring the bar parameters in each of four half-images (N, E, S, W) of the time slice separately and measuring the deviation of these measurements from that of the full time slice.

To define the spiral arm contrast $S(t)$ for a given population age t, we first measure the radial flux profiles of the galaxy within the spiral arm $f_s(r,t)$ and disc regions $f_d(r,t)$ separately as a function of radius r at that age t. These are obtained using the Galaxy Zoo:3D spiral masks, where the spiral region is defined as that where at least 40% of users have marked as being part of the spiral arms, and the disk region as that where less than 20% of users marked as being spiral arms. The specific thresholds used are somewhat arbitrary, since a spiral arm wave does not normally have a clearly-defined edge. However, these thresholds were chosen to ensure that a sufficient number of spaxels are included in both regions. Using these, we define a radially-dependent spiral contrast

$$S(r,t) = \frac{f_{\rm s}(r,t) - f_{\rm d}(r,t)}{f_{\rm d}(r,t)}, \tag{4.1}$$

and then take the median value of this quantity over all radii for a given time slice t as the single-valued spiral arm contrast $S(t)$. An uncertainty in this measurement is estimated by considering the uncertainties in measuring $f_{\rm d}(r,t)$ and $f_{\rm d}(r,t)$ due to the scatter of individual spaxel fluxes at a given r and t, and propagating these using Equation 4.1.

4.5.2 Variation in spiral arm and bar properties in different time slices

Figure 4.3 shows how these bar and spiral arm parameters change with stellar population age, for time slices centred on each SSP age used in the fit. The same parameters measured for the Hα emission map — which represents the very latest star formation in the galaxy — is consistent with those measured for the youngest populations, despite emission lines being excluded from the stellar population fitting. We also measured S and the bar parameters for u-, g-, r-, i- and z-band images. For consistency with the time slice measurements, these images were generated from applying the SDSS filter functions to the MaNGA datacube rather than using the higher-resolution and larger FOV in the raw SDSS imaging. The broad-band structural measurements show general agreement with the results from the stellar populations, (expecting that the redder bands are most sensitive to older populations), but highlight the amount of extra information which can be obtained from this stellar population analysis.

The bar is detected in stellar populations of all stars younger than 4 Gyr, and *exhibits variation in its length at different stellar ages*. It is not clear that this variation necessarily reflects the historical bar growth, or whether it is an imprint of the original radial distribution of stars which became locked into the bar when it formed. However,

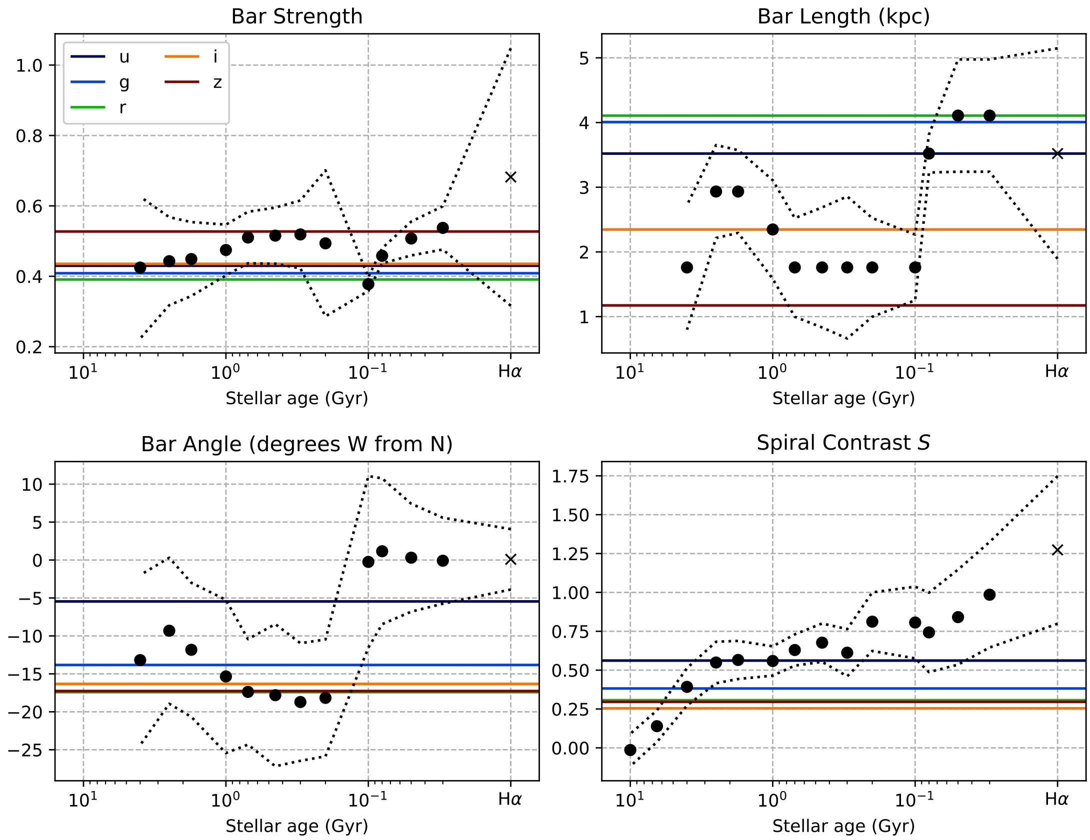

Figure 4.3: Bar and spiral parameters as a function of stellar age. Filled points are from the stellar population analysis, and the cross shows the results from the same measurements of Hα emission. Uncertainties are indicated by dotted lines. Coloured lines indicate the measurements obtained from the SDSS bands.

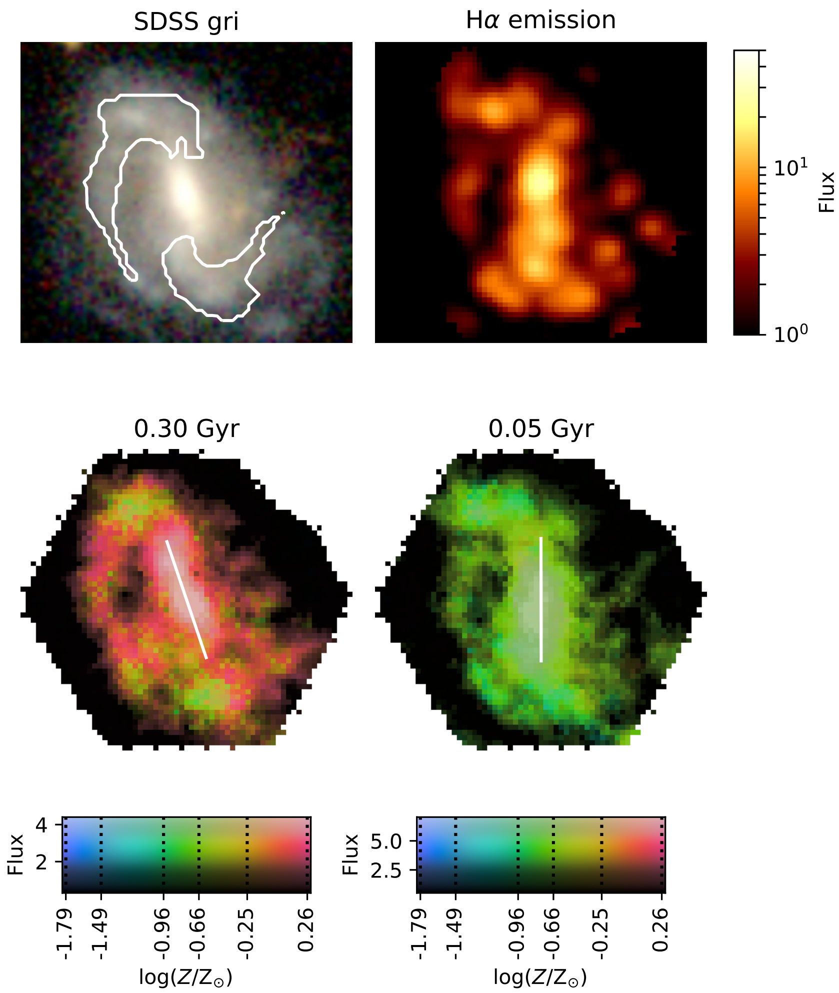

Figure 4.4: *Top left*: SDSS gri band image of galaxy MCG+07-28-064 showing outlines for the spiral mask from Galaxy Zoo:3D. *Top right*: Hα emission line flux map from the DAP. *Bottom row*: Maps of the stellar populations centred on ages of 0.3 Gyr and 0.05 Gyr, highlighting the observed change in bar angle between these stellar populations as indicated by the white lines. Both stellar maps are created as in Figure 4.2, by smoothing all SSP weights with a Gaussian of width 0.4 dex centred on the labelled age. In both time slices, the 4020 Å flux (measured in 10^{-14} erg s^{-1} cm^{-2} Å^{-1}) and the light-weighted mean metallicity (in $\log(Z/Z_{\odot})$) of each spaxel is represented using the colour scheme shown underneath. The metallicities of the youngest stars are not trustworthy, as explained in Section 4.5 and further discussed in Chapter 5.

since the bar instability is fundamentally a disk-related phenomenon, in either scenario it reflects the inside-out growth of the disk in this system. The other clear feature in the bar is the *discontinuity in its position angle at the youngest ages*, which we have highlighted in Figure 4.4. If the spiral arms are assumed to be trailing, this offset implies that stars are forming preferentially on the leading edge of the bar, as might be expected in this shock-forming region (Martin & Friedli, 1997; Verley et al., 2007a). The offset is only seen in stars younger than 0.1 Gyr because they have not had time to mix around their orbits, populating the whole bar potential. The agreement of the young stars' bar position angle with the independently-derived result from the Hα map adds significant confidence in the stellar population analysis.

A clear trend with age is also apparent in the spiral arm contrast $S(t)$. In the oldest stars the arms are not detected, while in most stellar population ages between 0.2 and 2 Gyr there appears to be about a 75% enhancement of stellar density in the arms, which rises further in stars younger than 0.1 Gyr toward the Hα contrast. Again, this picture is consistent with what might be expected in such a grand-design spiral galaxy, with the oldest stars forming a well-mixed population that is too dynamically hot to show the imprint of the arm, the intermediate-age stars making up the relatively modest density contrast representative of a spiral density wave, and the youngest stars showing the disproportionately-enhanced star formation that such a density wave can produce (Lin & Shu, 1964; Roberts, 1969).

4.5.3 A spurious population at 2.5 Gyr?

By contrast, the apparent increases in bar length and angle in Figure 4.3 at a stellar age of 2.5 Gyr are not real, and are a reflection of the level of systematic errors and degeneracies present in this analysis. Inspection of Figure 4.2 at 2.5 Gyr indicates that these features

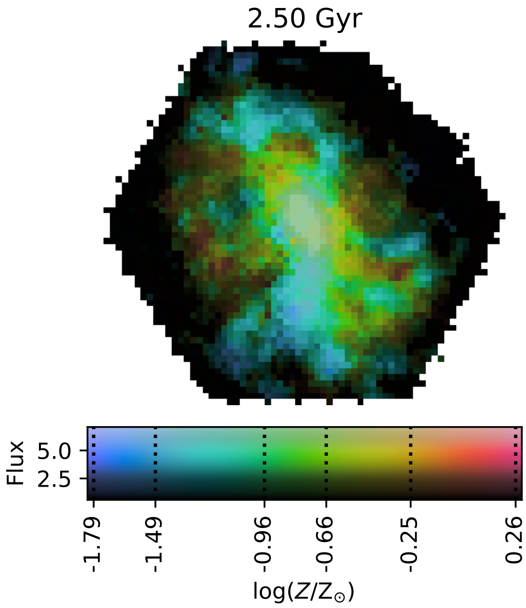

Figure 4.5: A time slice similar to those shown in Figure 4.4, but for a stellar population centred on 2.5 Gyr. The underlying bar of stars of $Z \approx 10^{-0.5}$ $Z_\odot$ is contaminated by a spurious population of $Z \approx 10^{-1.2}$ $Z_\odot$ stars, which are responsible for the skewed bar angle and length measurements in Figure 4.3.

are driven by an apparent population of low-metallicity stars of this age at the ends of the bar, shown in the time slice shown in Figure 4.5. The existence of such a trapped population would be fascinating, but based on our understanding of the dynamics of bars it seems more likely that their presence arises from either cross-talk between stellar population templates or from the lack of extremely young templates available in the fit, using stars with these properties to fill in some systematic shortcoming in this complex fitting process. These potential limitations will be addressed in more detail in Chapter 5.

4.6 Discussion and Conclusions

The above pilot analysis shows that there is a great deal of detailed information that can be derived on stellar populations from spectral fitting to IFU data. The coherence of the structures that emerge from this analysis — and their broad consistency with expectations in the context of galaxy evolution — indicate that our analysis allows us to extract information from spectra that would otherwise not be available. It is important to note that this coherence is in no way imposed on the analysis; since the spaxels are fitted individually, if the process were just fitting noise then the lack of information would be reflected in largely featureless noisy images. Further reassurance is offered by the consistency between the spatial properties of the youngest stellar populations derived from the absorption-line spectra and the results obtained entirely independently from the Hα emission-line image extracted from the same data cube.

We have shown an example where careful analysis of the full spatial variation in the measured star-formation histories can reveal interesting properties of the bar and spiral arms. We found that the bar's length in MCG+07-28-064 varies according to stellar population age, which we interpret as evidence for the inside-out formation of the galaxy's disk. We also found that the bar varies in position angle, which we attribute to shock-driven star formation occurring on its leading edge. The spiral arm contrast is strongest in the youngest stellar populations as expected, but stars as old as 2 Gyr still exhibit spiral structure at a level detectable in time slice analysis, indicative of an underlying density wave.

However, we have highlighted an example of an occasion where systematic errors and degeneracies when fitting so many parameters to each spectrum result in spurious features in the extracted time slices. More work will be presented in Chapter 5 to understand and quantify the covariances that will exist in this kind of study, but this initial study shows that such effects are not likely to compromise the analysis of higher surface-brightness features if proper care is taken in the interpretation of the results.

Having established the viability of deriving time slices for the full two-dimensional structure of galaxies using MaNGA IFU data cubes in this pilot study, it would now seem timely to expand analysis of this type to the large sample of galaxies becoming available in this and other surveys. Detailed stellar population analysis that goes beyond measuring the spatial variation in mean properties will allow us to understand the structure and growth of spiral galaxies and their azimuthal structures like bars and spiral arms in a way that has never been accessible before.

Chapter 5

Improvements and tests to spectral fitting

We have demonstrated the ability of time slicing methods to extract new insights into the structure and dynamics of individual galaxies. However, we have also highlighted occasions where small deficiencies in the spectral fitting techniques may potentially affect results, for example in Section 4.5.3. Before we apply this type of analysis to large populations of galaxies to make full use of the power of MaNGA's sample size, we must ensure that we have properly accounted for the limitations in stellar population fitting with STARLIGHT and hence adopted the best possible approach. In this chapter, we will describe the population analysis methods outlined in the previous chapters in more detail, and discuss some tests and improvements to the method to allow for a larger study of measuring the spatial distributions of stellar populations in many galaxies.

5.1 Treatment of emission lines

We begin by adopting a similar technique to that employed in Chapters 3 and 4 by retaining the approach of fitting each spectrum in each galaxy using STARLIGHT (Cid Fernandes et al., 2005). Before fitting, we de-redshift each spectrum using the NSA redshift measurements and the DAP's (Westfall et al. 2019; see Section 2.2) stellar velocity measurements. As before, we also remove emission lines from each spectrum prior to fitting. In Section 3.3.2, we found that measuring the emission line spectrum using `pPXF` gave the same results as using the DAP emission-line spectrum. We will use the DAP measurements from here onwards to avoid unnecessary steps in the fitting processes, and also since there has been significant work done for the most recent versions to ensure their robustness (Belfiore et al., 2019).

5.2 Error and flag spectra

As previously, the de-redshifted and emission-subtracted MaNGA spectra are rebinned onto a linear wavelength scale (as required by STARLIGHT) before fitting.

As well as the input spectrum's wavelengths and flux, it is also recommended (but not required) to provide STARLIGHT with an error spectrum to indicate the uncertainties on each pixel of the input spectrum. For this error spectrum e_λ, we use the reciprocal of the square root of the DRP's spaxel-by-spaxel measurements of the inverse variance ("`IVAR`"), which estimates flux uncertainties during data reduction (see Section 2.1.4).

As recommended, we also provide a full mask spectrum for each spaxel (rather than a general mask applied to all spectra), which removes DRP- or DAP-designated artifacts, and regions for which the DAP was unable to measure an emission line. This ensures that STARLIGHT is only attempting to fit spectra — and regions of spectra — for which we are confident the results will be reliable.

5.3 Template stellar population spectra

We previously used SSP template spectra from the MILES library (Sánchez-Blázquez et al., 2006; Vazdekis et al., 2010; Falcón-Barroso et al., 2011) in Chapter 3 covering 3540.5–7409.6 Å, and the longer templates from the related E-MILES library (Vazdekis et al., 2016) in Chapter 4 covering 1680–50000 Å. To make the best possible use of the wavelength range of MaNGA, we will continue to use the E-MILES library. We therefore use a combination of nine ages (log(age/years) = 7.85, 8.15, 8.45, 8.75, 9.05, 9.35, 9.65, 9.95, 10.25) and six metallicities ([M/H] $= -1.71, -1.31, -0.71, -0.40, +0.00, +0.22$) from the standard E-MILES library, assuming a Chabrier (2003) IMF, Girardi et al. (2000, "Padova") isochrones, and Milky-Way [α/Fe] ("baseFe"). We do not expect the exact choice of IMF or isochrone to significantly affect the results, and we found in Section 4.3.1.1 that the baseFe templates are sufficient to derive a star-formation history.

To sample the full star-formation histories in a large sample of galaxies, we also now include the younger templates of Asa'd et al. (2017) covering six ages (log(age/years) $= 6.8, 6.9, 7.0, 7.2, 7.4, 7.6$) and the two recommended metallicities ([M/H] $= -0.41, +0.00$), which are generated using the same method as the E-MILES set of Vazdekis et al. (2016), but with the earlier Bertelli et al. (1994) iteration of the Padova isochrones. Unfortunately there is no publicly-available combination of SSP templates from the Asa'd et al. (2017) and E-MILES libraries with identical isochrones, but as stated above, we do not expect isochrone shapes to affect our results. This is particularly true for the youngest populations, which will be dominated by the well-constrained main sequence.

Combining these two libraries allows us to exploit the high spectral resolution of

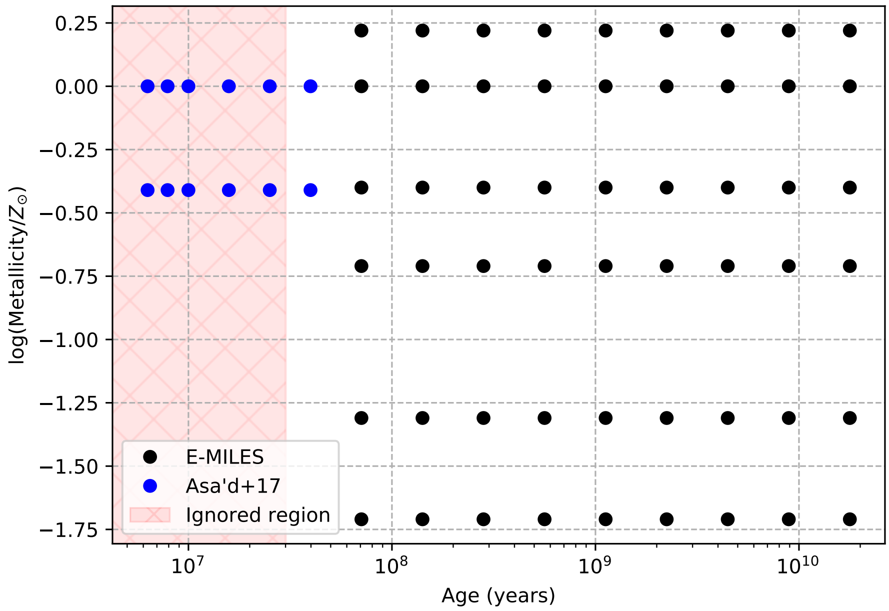

Figure 5.1: The adopted set of SSP template spectra used in fitting Chapters 5 and 6. Black points indicate SSPs from the Vazdekis et al. (2016) E-MILES library and blue points indicate those from Asa'd et al. (2017). The red-shaded region indicates the ages for which the template weights are ignored; see Section 5.5.

both MaNGA and E-MILES templates, while still being able to fully fit the whole of the star-formation histories of star-forming regions without combining different libraries produced in completely different ways. The resulting base size of 66 SSP templates is a compromise between manageable computation times when applied to samples of hundreds of galaxies whilst retaining a fine enough sampling to characterise the measured star-formation histories. The template ages were chosen so that they are approximately evenly spaced in log-space, as shown in Figure 5.1. We find that the smoothed SFHs using this SSP base and the larger sets used in Chapters 3 and 4 are entirely consistent.

We limit the fit to the wavelength range of 3541.4 to 8950.4 Å, within which the raw E-MILES templates have a constant FWHM of 2.51 Å. To ensure that the model and measured spectra have consistent resolution, we Gaussian-smooth each of the SSP templates to degrade them to the wavelength-dependent resolution of the median spaxel spectrum from all galaxies in our science sample of Chapter 6, using the rest-frame line spread function (LSF) measured by the MaNGA Data Reduction Pipeline (DRP; see Section 2.1.4). Each spaxel in each galaxy has a unique rest-frame LSF due to different velocity shifts, as well as variations in observation conditions. However, these effects are small in comparison to the overall wavelength-dependent LSF function, so to avoid excessive computation times required to recreate the SSP spectra for each individual fit, the median LSF of all spaxels is used for all fits.

5.4 Starlight configuration

As before, we use Starlight in a "long fit" mode to prioritise robustness over computation time, based on the recommendations from extensive testing of Starlight by Ge et al. (2018) and Cid Fernandes (2018). For example, we enforce long Markov chains (i.e. `N_chains = 12` in the Starlight "config" file), long fitting loops (`N_loops_FF = 8`, `N_loops_EX0s = 8`), and hard parameter convergence criteria at all stages (`IsGRTestHard_FF = 1`, `IsGRTestHard_BurnIn = 1`, `IsGRTestHard_EX0s = 1`).

Since the DAP robustly models the emission lines, we use STARLIGHT in its "NO-CLIP" mode to ensure that all of the diagnostic absorption lines are fully fitted rather than masked during the fit. The small number of wavelength pixels for which the DAP was unable to model either the continuum or emission lines reliably are masked before being fit with STARLIGHT. To ensure that the star-formation history of each spaxel is measured as fully as possible, we require STARLIGHT to retain at least 97% of its fit's total light during the "EX0" phase of reducing the number of templates used in the final fit (i.e. `EX0s_method_option = CUMUL` and `EX0s_Threshold = 0.03`). We also require the final fit to include weights assigned to at least 30% of the base (template) spectra (`fEX0_MinBaseSize = 0.30`).

The light weights we use from the fits (where relevant) are those contributed by each template at 4020 Å (`l_norm = 4020.0`) as used by Cid Fernandes et al. (2005). In almost all science analysis we ensure that we use either the mass weights — using the implicit mass-to-light ratios included in the SSP models and assuming a flat ΛCDM cosmology with $H_0 = 70$ km/s/Mpc — or only compare the spatial variation of flux weights of a specific age, rendering the exact choice of reference wavelength unimportant, since the mass-to-light ratio has only a moderate dependence on metallicity.

Any given model may represent the entire spectrum well at all wavelengths *except* that at which we measure the weights. We therefore allow the sum of weights at this wavelength to be between 50% and 150% of the input spectrum (`fn_low = 0.5` and `fn_upp = 1.5`) to ensure that the best fit of the whole spectrum is used.

From the STARLIGHT mass weights, a measure of the total stellar mass within the

MaNGA FOV can be readily calculated. Reassuringly, we find that these stellar masses agree well with those measured by the NASA-Sloan Atlas (NSA; Blanton et al. 2011); we discuss this further in Section 6.8.1. The E-MILES library contains stellar mass loss predictions for each of the SSP templates, allowing a measurement of the current mass and an initial mass at time of formation for each population contained within each spectrum. Unless otherwise stated, any quoted galaxy stellar mass measurements in this chapter and in Chapter 6 are those measured by Starlight, and the mass weightings used in this work are the present-day masses of each template, to avoid reliance on the mass loss predictions. In any case, we find that all results presented in Chapter 6 are entirely unaffected by the distinctions between Starlight- and NSA-measured total masses, and between initial and current SSP mass weights.

5.4.1 Treatment of dust extinction

Starlight has the capacity to fit a general dust law with extinction $A_{\rm V}$, and also include an extra extinction $A_{\rm V}^{\rm Y}$ which is applied only to specified templates in the fit. This extra parameter could, for example, allow for the possibility that the youngest stellar components are affected by dust extinction to a greater extent than those populations which would be expected to be free of their birth clouds. The exact values of $A_{\rm V}^{\rm Y}$ measured by Starlight would in that case be an interesting parameter to model and investigate. However, in practice, we found that this extra degree of freedom caused Starlight's fits to be drawn towards negative extinctions when we included a $A_{\rm V}^{\rm Y}$ term for all populations younger than $10^{7.05}$ years. This is likely due to the combination of the limited wavelength range for which these youngest templates dominate the spectrum due to their extreme colours, and the lack of any significant spectral information beyond their continuum shape. To the best of our knowledge, the $A_{\rm V}^{\rm Y}$ parameter in Starlight has not successfully been applied to any real spectral fitting to date.

We therefore include a single Calzetti et al. (2000) dust law in the fit, which has the same A_V for all templates. We allow A_V to vary in the range of $-1 \leq A_V \leq 8$ (`AV_low = -1.0` and `AV_upp = 8.0`), and we find that over 90% of the spaxel fits in most galaxies are within the range $0.1 \leq A_V \leq 0.8$.

5.4.2 Kinematics

We use the stellar velocity dispersion $\sigma_\star$ measured by the MaNGA DAP (Westfall et al., 2019) as an initial kinematic guess for the de-redshifted input spectrum's STARLIGHT fits, but allow its value to vary as a free parameter in the range of $\sigma_\star$ = 20 to 900 km/s (`vd_low = 20.0`, `vd_upp = 900.0`). Similarly, despite de-redshifting each spectrum individually using the DAP's stellar velocity $V_\star$ measurements, this is a free parameter for STARLIGHT to vary in the range of $V_\star$ = −600 to 600 km/s (`v0_low = -600.0`, `v0_upp = 600.0`) to find its best possible fit, using $V_\star = 0$ as the initial guess. In practice, we find that STARLIGHT's fits are consistent with $V_\star = 0$, with little deviation in $\sigma_\star$ from the DAP measurements. Unlike other spectral fitting tools such as `pPXF` (Cappellari & Emsellem, 2004), STARLIGHT is not fine-tuned for measuring stellar kinematics, and we do not expect STARLIGHT's exact measurements of $\sigma_\star$ to impact the measured SFHs.

5.5 Cross-talk between the oldest and youngest templates

We would not expect the star formation rate or chemical evolution to vary significantly within the last 10^8 years in the majority of cases (see e.g. Schönrich & Binney 2009), but initial tests with STARLIGHT revealed that there was a significant correlation between the weights assigned to templates of $\gtrapprox 10^{9.5}$ years and those of $\lessapprox 10^{7.2}$ years, resulting in a

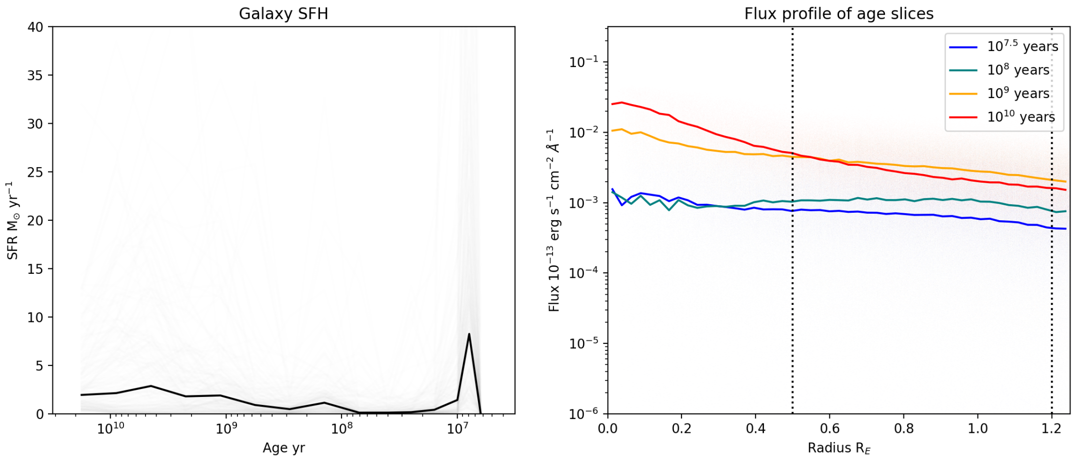

Figure 5.2: *Left*: Derived *unsmoothed* star-formation histories for a large sample of spiral galaxies, showing an unphysical peak at $\sim 10^7$ years. *Right*: The average radial 4020 Å flux profiles of the same galaxies.

sharp peak in the SFH at $\sim 10^7$ years. An example of this is shown in Figure 5.2. This effect was found to be present in all locations of all galaxies regardless of signal-to-noise or the strength of dust extinction, and often resulted in an implied recent SFR of the galaxy to be at least an order of magnitude greater than at any previous time in its history, of up to ~ 25 $M_\odot$/yr in some cases. Cid Fernandes & González Delgado (2010) also observed similar effects, and argued that this phenomenon is related to the known "UV upturn" seen in old stellar populations, which is normally attributed to planetary nebula cores; see Yi (2008) for a review. The cause and presence of this excess of blue light is not accounted for in the old SSP template spectra, so Starlight is forced to attribute it to another population. This false attribution is given to the youngest stellar populations, since these have the most similar spectral properties to the cause of the UV upturn: a blue continuum and few absorption features.

As a result, the implied flux profiles of populations of different ages were affected. In Figure 5.2, a clear trend of more extended distributions exhibited by younger stellar populations is bucked by that of the very youngest stars, which instead seem to partially track the distribution of the oldest stars. When analysed in a large sample of galaxies

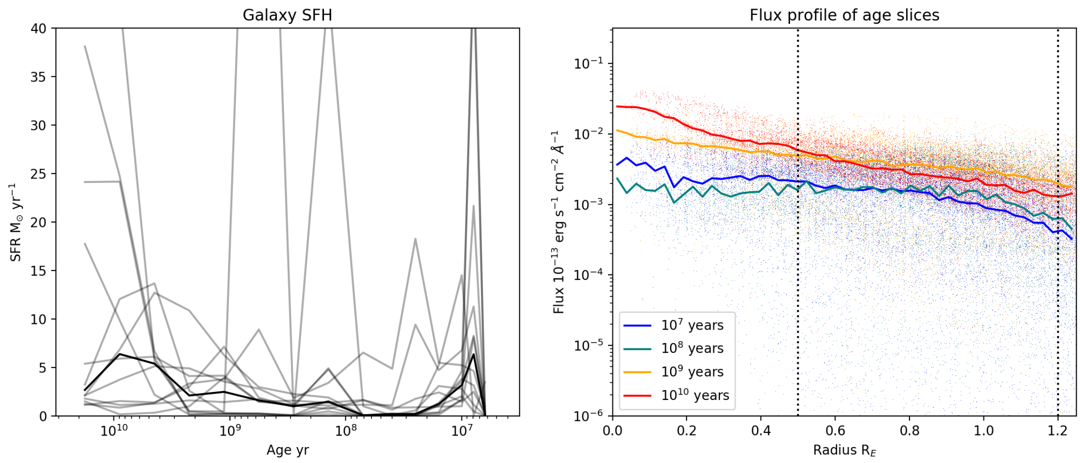

Figure 5.3: As Figure 5.2, but for a subsample of twelve galaxies, and with the lower bound of the fitting window increased to 3700 Å. The spurious SFH peak (and associated radial flux profiles) is broadly unchanged. The heavy black line indicates the average SFH of the twelve galaxies.

such as will be explored in Chapter 6, this would significantly distort the results. We have therefore explored a number of different possible mechanisms to remove this bias.

5.5.1 Limiting the fitting wavelength range

Using a test subsample of twelve galaxies, we first attempted to mitigate this effect by fitting only from 3700 Å instead of 3541.4 Å to avoid the worst-affected wavelengths, but found this had no measurable effect on the unphysical derived star-formation histories, as shown in Figure 5.3. We chose not to increase this lower wavelength limit further to avoid impacting the valuable Balmer absorption series.

5.5.2 Forcing a flat recent SFR

We then performed another fit with Starlight but where we had combined all of the templates younger than $10^{7.5}$ years for each metallicity into a single template representing a flat SFR over that time interval, and used these two templates (corresponding

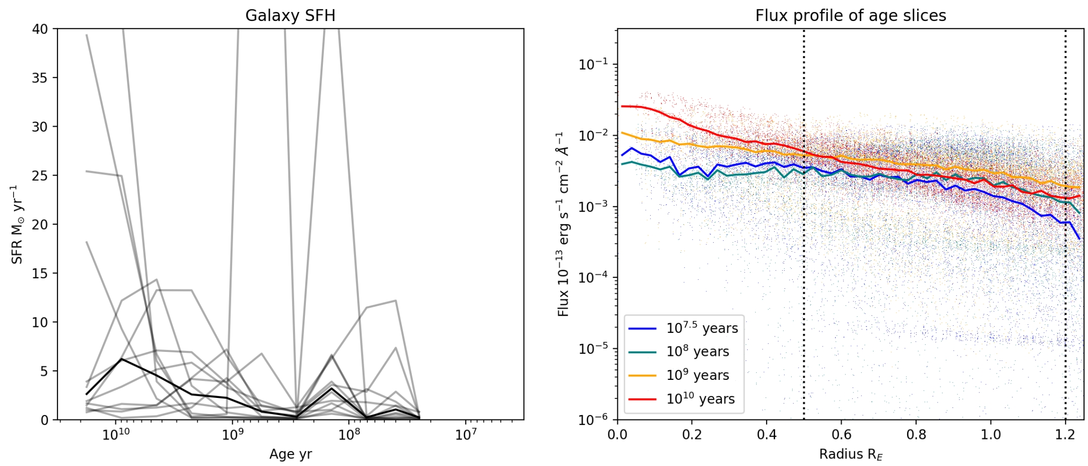

Figure 5.4: As Figures 5.2 and 5.3, but for a subsample of twelve galaxies, and with the most recent SFH forced to be flat: all SSPs younger than the youngest shown have been combined into a single template.

to the high and low metallicities available at these ages) in the fit instead of the original eight over this time interval, since we know that the SFR is very unlikely to change significantly over that time. The flat-SFR templates are defined as

$$S^Z_{\text{flat}} = \left(S^Z_1 \times t_1\right) + \sum_{n=2}^{8} \left[S^Z_n \times (t_n - t_{n-1})\right] \tag{5.1}$$

where S^Z_n is the spectrum of the n^{th} youngest SSP template with metallicity Z and age t_n. This assumes that a stellar population of any arbitrary age t is represented by the youngest E-MILES SSP spectrum for which that SSP's age is greater than t; i.e. $S^Z_t \equiv S^Z_{\min\{n\,:\,t_n \geq t\}}$.

As shown in Figure 5.4, the STARLIGHT results of this approach shows that enforcing a flat SFR in the youngest templates has no noticeable effect (< 0.1 dex) on the SFH in ages $\geq 10^{7.5}$ years at all. However, the youngest populations still show less extended radial distributions than those of 10^8 years, indicating that the correlation has simply moved to the combined SSP template. This is not noticeable as a peak in the SFH since this "peak" has now been spread over the full range of ages for which we combined the templates.

5.5.3 Limiting the range of available SSP templates

Similarly, when we compared Starlight fits using only those SSP templates for which $t_n > 10^{7.5}$ years (i.e. reduce the base shown in Figure 5.1), we found that the excess of hot stars was simply assigned to whichever stellar population was youngest. The rest of the star-formation histories were unaffected. We concluded that the youngest stellar population available in the Starlight fit would always have a "cross-talk" effect with populations $\gtrapprox 10^{9.5}$ years. The flux assigned to the youngest populations will always be a combination of the "true" flux from stars of that age, as well as a spurious contribution from the hot stars present but not modelled in older populations.

5.5.4 Adopted approach

It may be possible to effectively separate these two effects when stellar population models are able to fully model the hot stellar remnants or other factors responsible for the UV upturn. However, for the purposes of the work presented in this thesis, the weights and fluxes of stellar populations younger than 30 Myr are fundamentally unreliable, so *we resolve to ignore these populations entirely* and do not use them in deriving the Starlight-measured star formation histories. The SFHs are not likely to have varied over this time period (Schönrich & Binney, 2009), but such young stellar populations are clearly present in many galaxies, so by including these SSPs in the fit but ignoring their weights allows the spectrum to be fully modelled and does not limit the results from our analyses.

Based on this analysis, we advise users of Starlight and other stellar population fitting software to carefully consider the effects of attempting to measure star-formation histories to young ages without accounting for the limitations of SSP models to include the UV upturn. Cautious interpretation of all derived SFHs is essential to determine which parts of a SFH are likely to be correctly measured. On the other hand, we do see that the older populations are almost entirely unaffected however the youngest populations are modelled, so are likely to be robustly reliable.

5.6 Effects of low signal-to-noise

Many authors spatially bin neighbouring spaxels of integral-field spectroscopic data to create regions with approximately constant signal-to-noise ratio (SNR) before fitting. However, since we wish to retain and measure the full spatial information of the stellar populations — and therefore fit each spectrum independently instead of binning — we require the STARLIGHT fits in regions with low SNR to be reliable. Ge et al. (2018) showed that STARLIGHT may exhibit bias in the fitting of spectra with low SNR, but Cid Fernandes (2018) contend that these effects are not significant in most physical applications and with the robust STARLIGHT configuration used here. To assess this conclusion, we have performed a series of tests laid out here.

5.6.1 Average fits of regions with low signal-to-noise ratio

To test how the signal-to-noise ratio (SNR) of a spectrum in a MaNGA datacube may affect the fitting results from STARLIGHT, we combined spectra of a single galaxy (plate-IFU 8329-12701) within different SNR bins to form a single integrated spectrum for each bin. In combining spectra from the MaNGA datacube, emission lines were removed and the spaxel spectra de-redshifted and interpolated onto a common wavelength base before summing. Each single spaxel's SNR was then defined as the median value over

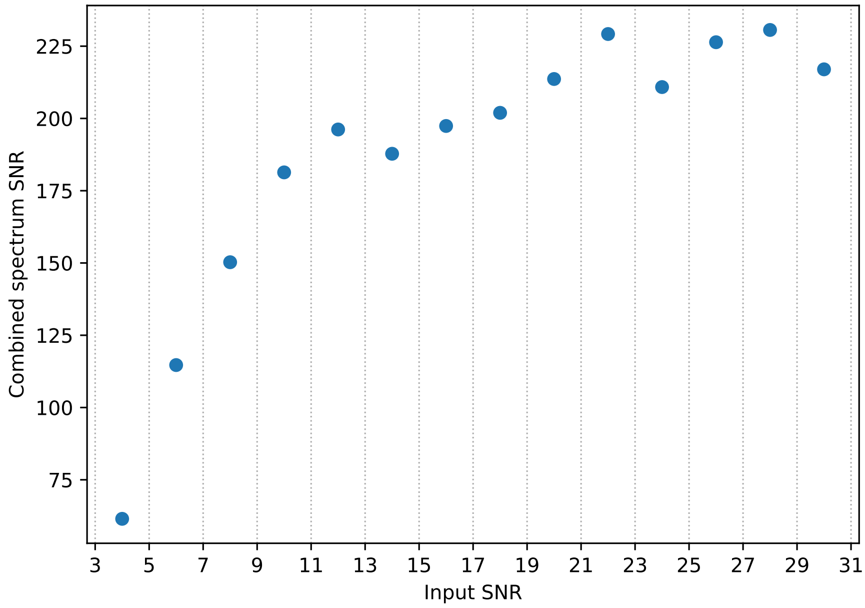

Figure 5.5: The combined SNR of the spectra created in Section 5.6.1 by summing individual spaxel spectra in different SNR bins. All combined spectra have high SNR, typically above 100.

the fitting wavelength range (see Section 5.3) of the ratio between the spaxel's flux spectrum and the reciprocal of the square root of the inverse variance spectrum (as measured by the DRP; see Section 2.1.4).

We chose to combine spaxel spectra in SNR bins of width 2, centred on every even value. A single spectrum was created by combining all spectra from spaxels with SNR between 3 and 5, another from spaxels with SNR between 5 and 7, etc., up to a spectrum comprising the sum of all spaxels with a SNR between 29 and 31. As shown in Figure 5.5, each of the combined spectra's signal-to-noise ratio is greater than 60 and most are greater than ~ 200. These combined spectra were then fit using Starlight with an identical configuration to that of the science fitting to see how their measured star-formation histories varied from the average of their constituent parts. In the absence of any systematic bias in Starlight, it would be expected that the average SFH measured in all individually-fitted spaxels in a given SNR bin should be the same

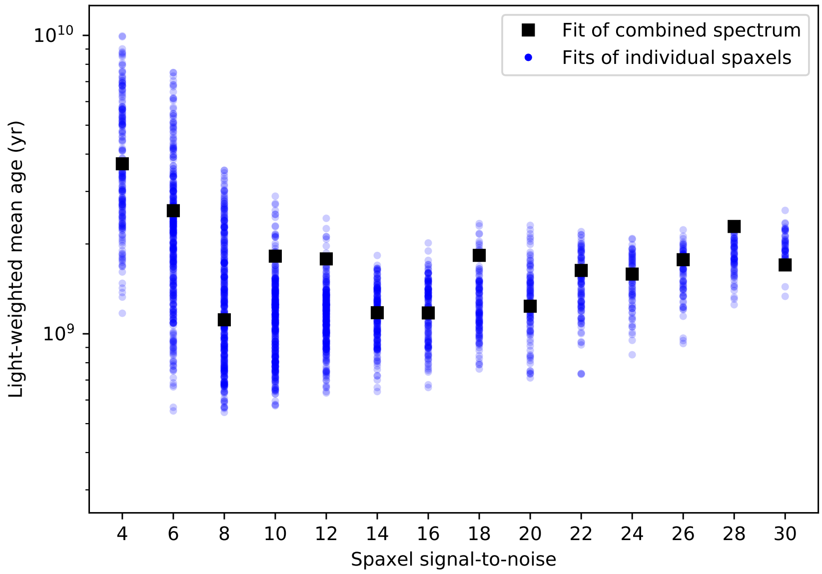

Figure 5.6: The mean age of spaxels in different signal-to-noise ratio bins (*blue*) in a spiral galaxy compared to the mean age of the spectrum of all spaxels combined (*black squares*). There is no significant bias in the average age measured by STARLIGHT compared with varying SNR.

as the SFH measured from the average spectrum of those spaxels.

We find that the light-weighted mean age of the summed spectrum is always within 0.2 dex of the mean age of all individual spaxels (separately fitted) in a given SNR bin, indicating that signal-to-noise effects do not significantly bias the average results (see Figure 5.6). However, perhaps surprising, we find that the full star-formation histories of the summed spectra are most discrepant for the bins of larger SNR, as shown in Figure 5.7. This is likely due to an effect of small systematics (e.g. sky subtraction or flux calibration) dominating over random noise when summing spectra of already-high signal-to-noise ratios. In summing high-SNR spectra, the modest reduction in combined SNR is outweighed by the increase in systematic errors when considering the fine detail required to measure a SFH. The fact that these effects have less significance in measuring the average properties highlights the level of extra complexity involved in measuring

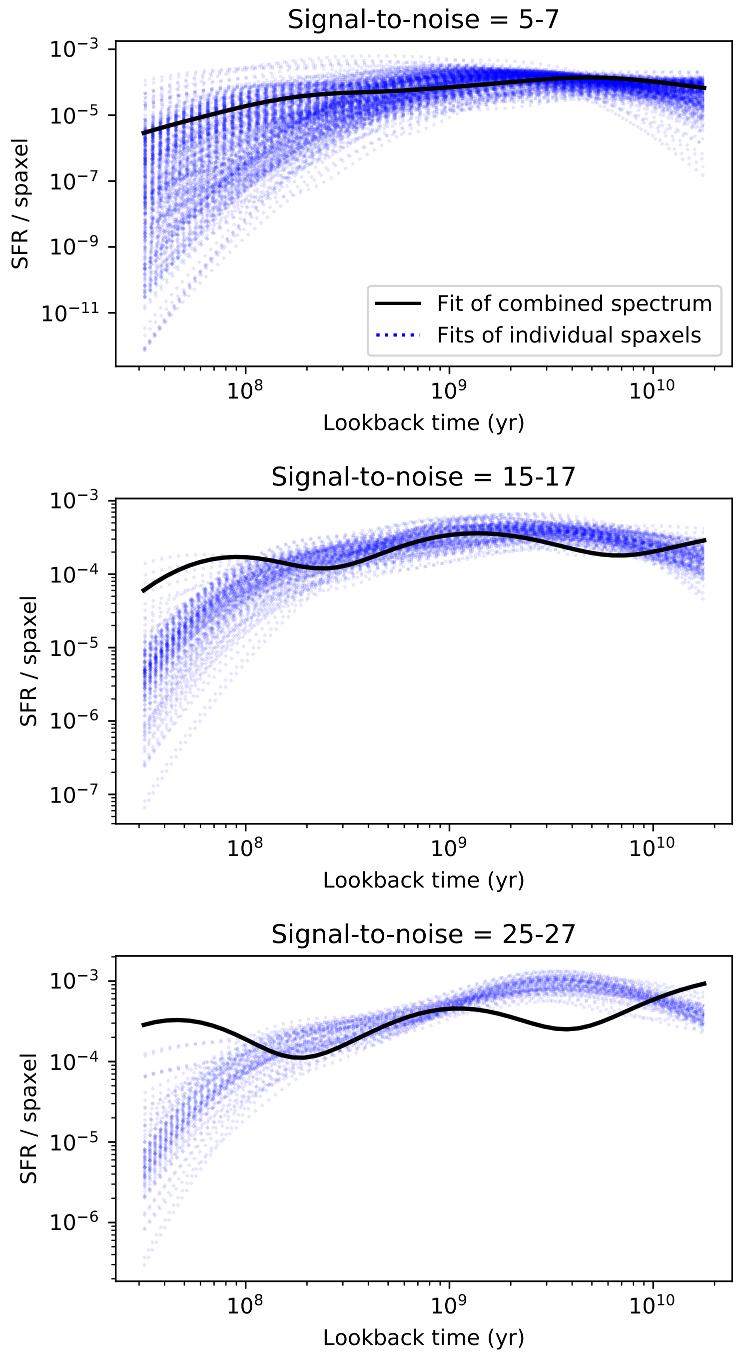

Figure 5.7: The star-formation histories of spaxels (*blue*) in three different signal-to-noise ratio bins compared to the SFH of the spectrum of all spaxels combined (*black*). STARLIGHT shows worse performance at higher signal-to-noise ratios.

SFHs over mean ages.

5.6.2 Recovery of a single stellar population

To further examine whether the above effects are due to systematics in the spectra rather than in Starlight, we tested how well Starlight is able to return the age and metallicity of a single stellar population with known parameters. We can create spectra representing single stellar populations of any age and metallicity by interpolating over the grid of E-MILES SSP template spectra. We produced spectra representing 200 ages and three metallicities using a bilinear interpolation in 2D log space of the 66 SSPs used in the fitting. We then degraded these spectra to signal-to-noise ratios of 5, 10, 15, and 20 by adding Gaussian noise, and also applied a dust extinction with $A_V = 0.2$ using a Calzetti et al. (2000) extinction curve. We blurred these 2400 individual spectra to the MaNGA LSF using the same approach as in Section 5.3, and then applied Starlight using the same SSPs and Starlight configuration as described in Sections 5.3 and 5.4 and as used in science cases, to compare how well the populations are recovered under different circumstances.

5.6.2.1 Light-weighted measurements

The 0.3-dex smoothed distributions of light weights measured from the Starlight output of these known SSPs is shown in Figure 5.8, for signal-to-noise ratios of 5, 10, and 15 and each metallicity. Results for a signal-to-noise ratio of 20 were unchanged from that of 15. Starlight is able to recover the mean age of input stellar populations of all ages older than $\approx 10^8$ years even with an input spectrum signal-to-noise ratio of 5, highlighting the diagnostic power of using such a long wavelength range to model the large-scale continuum in fitting. There is also no significant increase in Starlight's

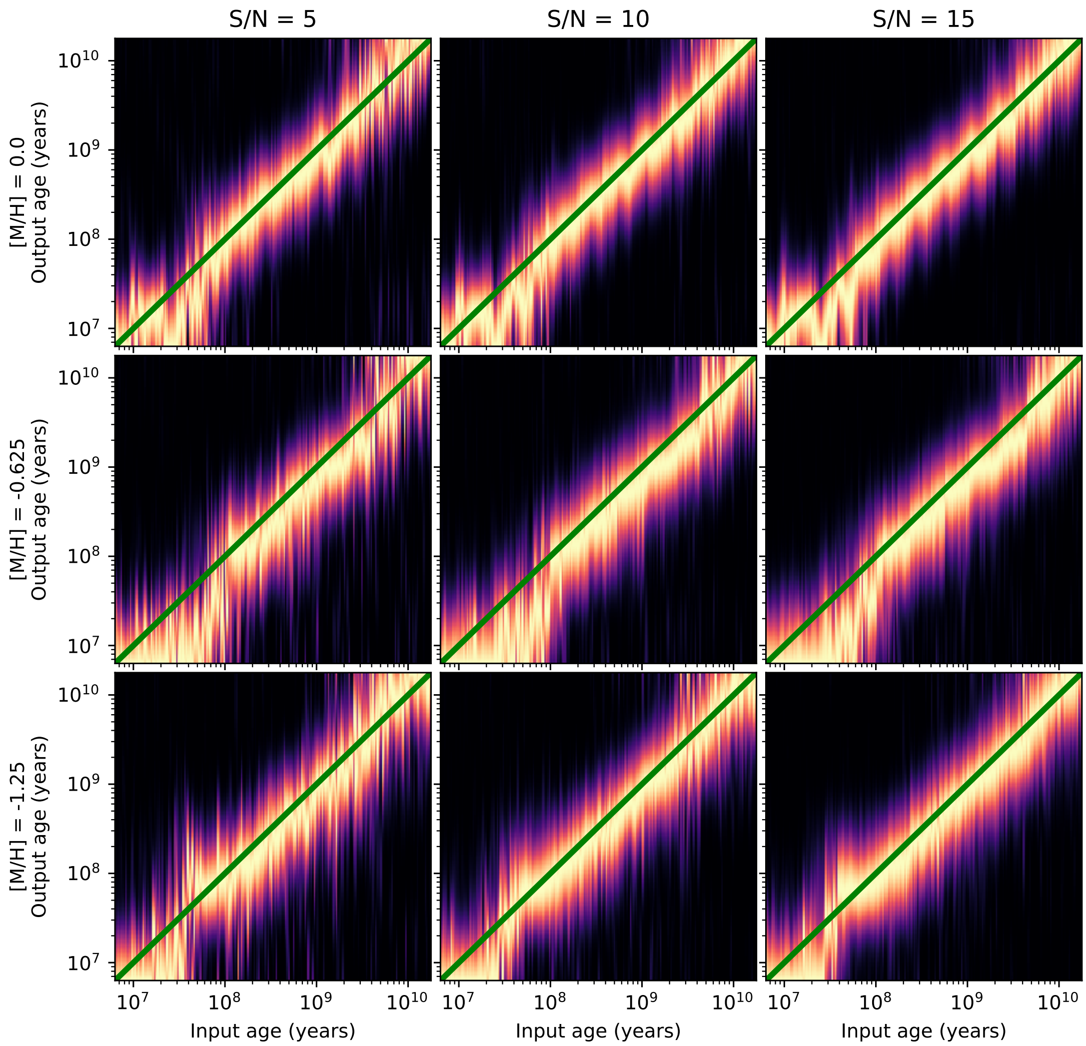

Figure 5.8: Distributions of the measured flux weights given by Starlight in fits of stellar populations of known age, for signal-to-noise ratios of 5 (*left column*), 10 (*middle column*), and 15 (*right column*). Input spectra are interpolated from the grid of E-MILES SSPs at $Z = Z_{\odot}$ (*top row*), $10^{-0.625} Z_{\odot}$ (*middle row*), and $10^{-1.25} Z_{\odot}$ (*bottom row*). The recovered weight distributions are smoothed by 0.3 dex, and the green line indicates equality between input and output ages.

ability to recover the input population beyond a SNR of 10. It is not necessarily clear how much the boundary between the two template libraries affects STARLIGHT's inability to recover stellar populations younger than $\approx 10^{7.5}$ years, or whether it is purely due to the lack of diagnostic spectral information at these ages.

However, a small bias towards younger ages is seen in many cases. This effect is indicated in Figure 5.9, where the measured light-weighted mean ages of the unsmoothed SSP weight distributions are younger than the input age for most populations, particularly in the case of $Z = 10^{-0.625} Z_{\odot}$. For input populations older than 10^8 years, this bias is at a level less than 0.3 dex (and so is within the width of the smoothing applied to the SFHs), and does not show any clear trend with age. The measured light-weighted median age agrees well with the mean age in almost all cases, indicating symmetrical distributions about the measured mean value.

5.6.2.2 Mass-weighted measurements

In Figure 5.10, we show the same fits' smoothed distributions of mass weights. Here, the input populations are accurately recovered, but a tendency to also include small levels of older populations is highlighted. This is a consequence of the combination of a strong trend in mass-to-light ratio with stellar population age and the robust STARLIGHT configuration used. As STARLIGHT fits the input spectrum (i.e. in light space), we force it to assign a weight to at least 30% of all SSP spectra to ensure full SFH recovery in science cases, as explained in Section 5.4. In the case of a single input stellar population, this will result in small spurious weights being given to other templates, and this noise becomes amplified in old populations when considering mass weights.

These extra weights are reflected in increased noise in the offset between the mass-weighted mean recovered and input ages, shown in Figure 5.11. For populations younger

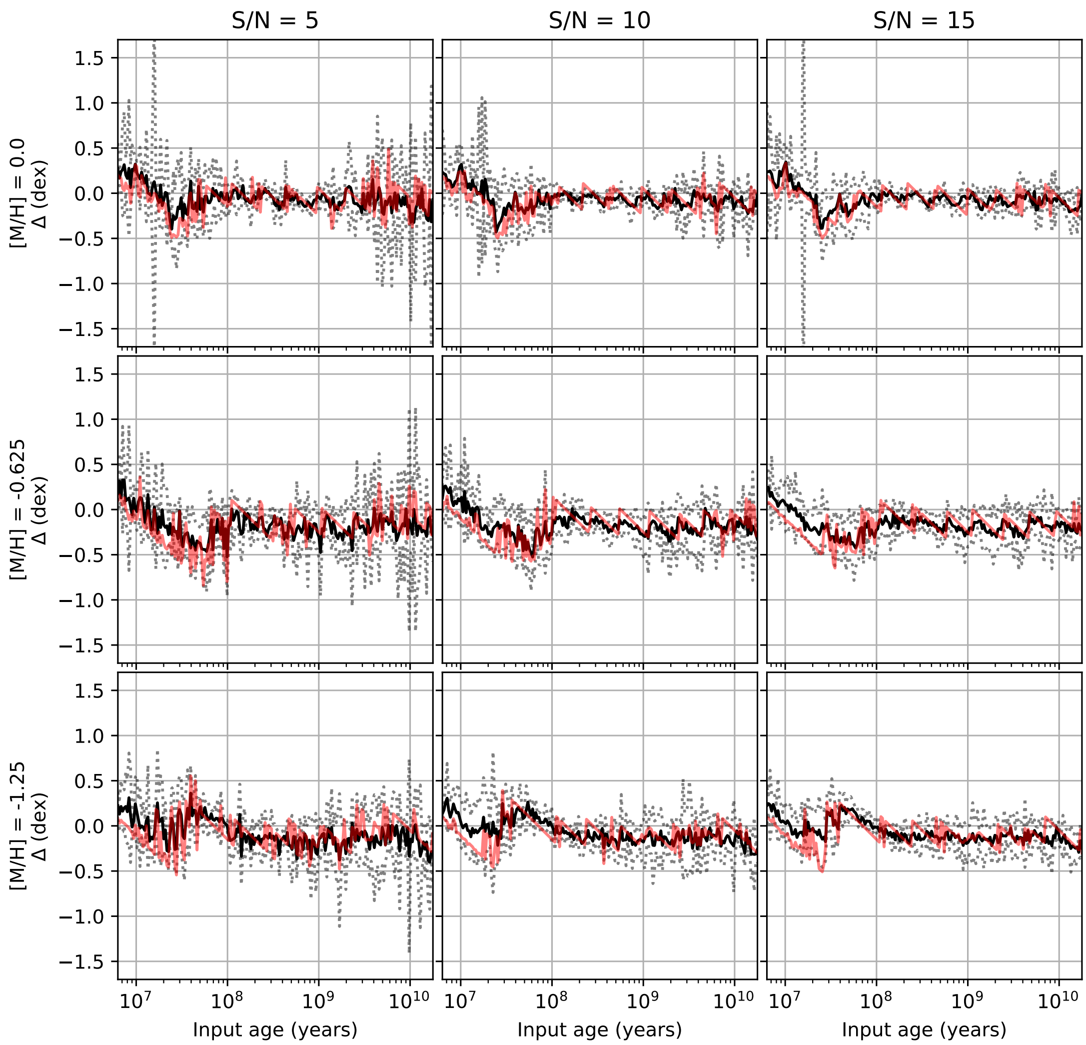

Figure 5.9: Layout as Figure 5.8, but showing the offset Δ between the light-weighted mean (black) — or median (red) — age of the raw (i.e. unsmoothed) STARLIGHT fits and the input spectrum age. Lower values of Δ indicate an underestimate in the measured ages. Dotted lines indicate one standard deviation of the output flux weights about the mean value.

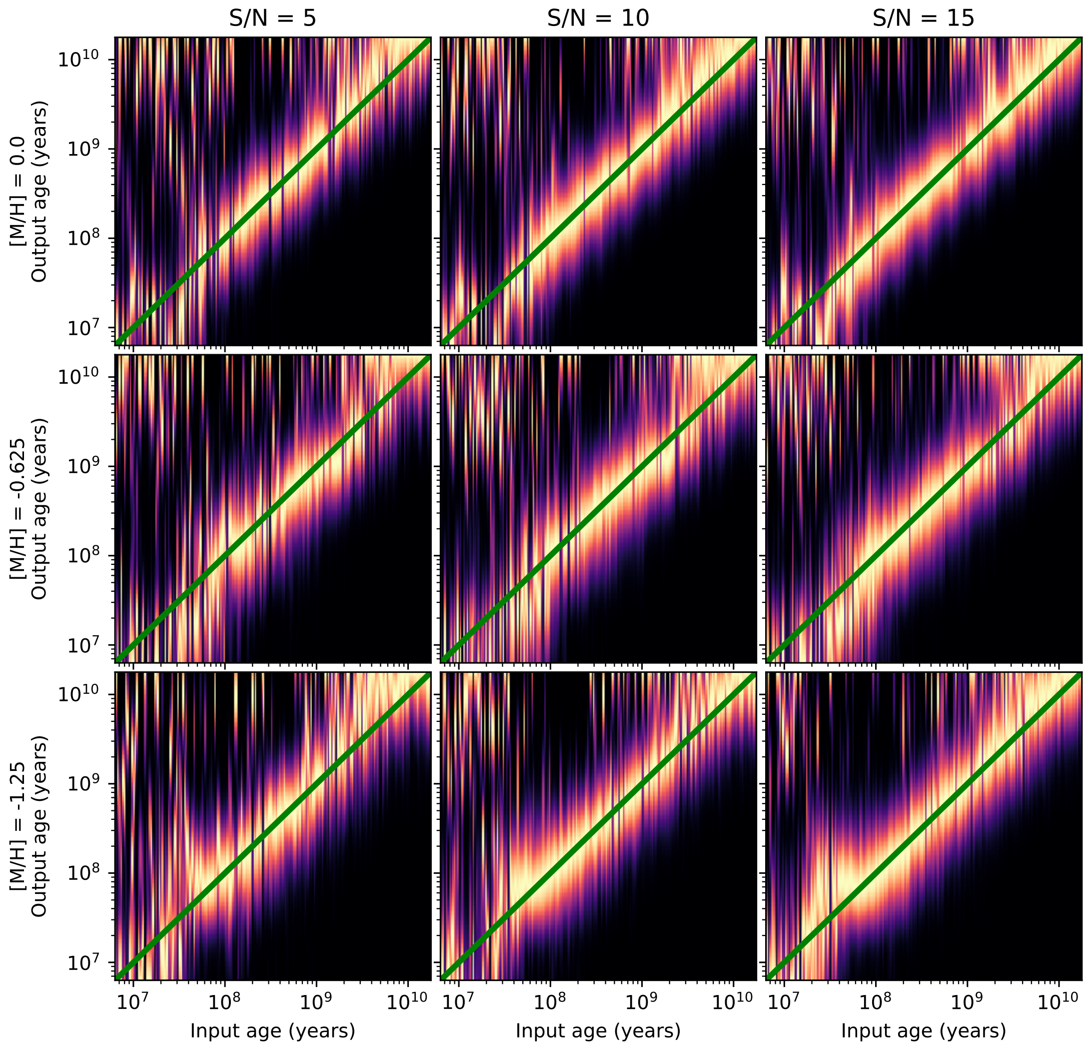

Figure 5.10: As Figure 5.8, but showing the smoothed distribution of mass weights.

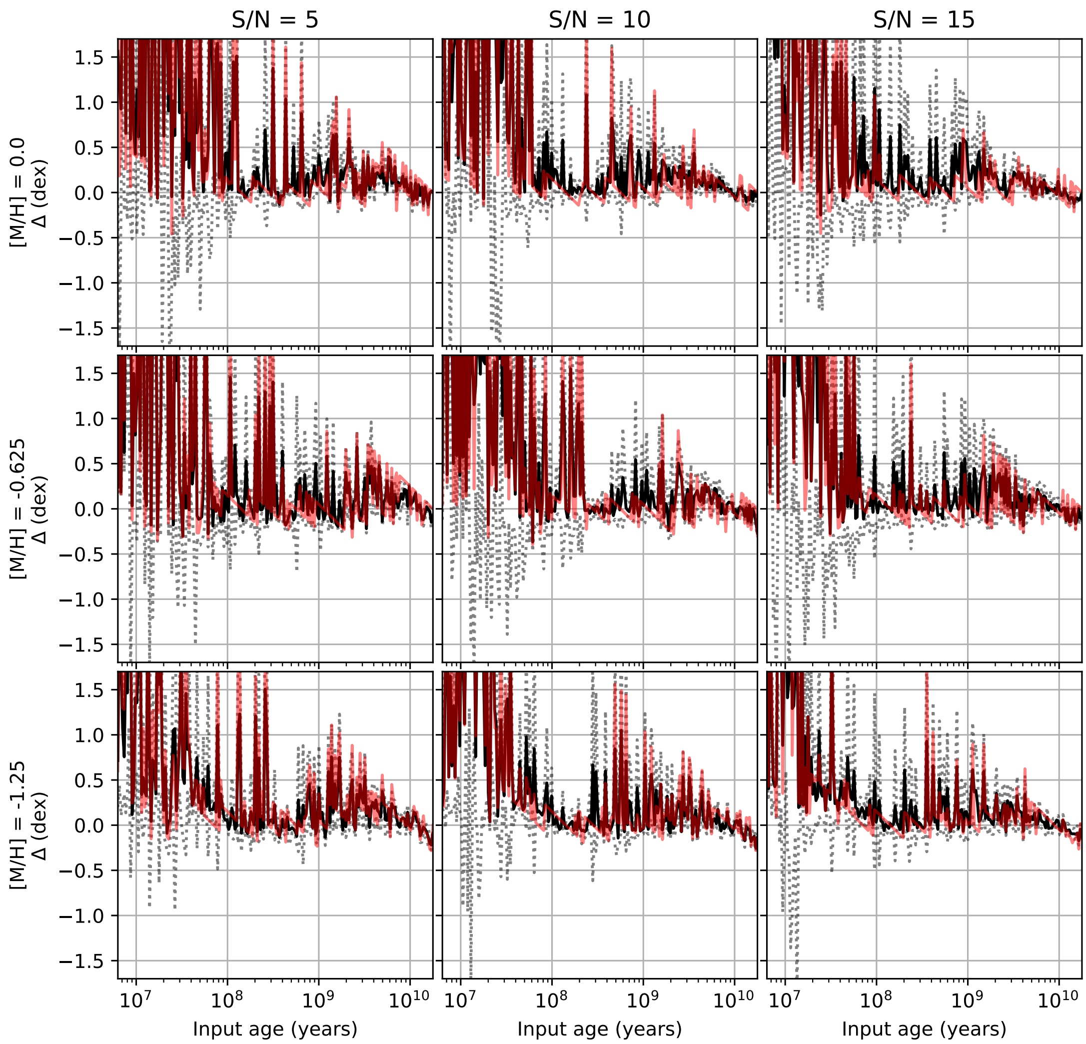

Figure 5.11: As Figure 5.9, but showing the offsets in mass-weighted mean and median ages.

than $\approx 2 \times 10^7$ years (where we have chosen to ignore the population weights in science cases anyway, as described in Section 5.5.4), this noise dominated over STARLIGHT's ability to recover the input ages. In older populations, while the bias towards younger ages seen in the measured light-weighted mean ages is eliminated, the scatter around the true value is instead increased, but at a level low enough to not significantly impact science results.

5.6.2.3 Effects of kinematics and dust

To test whether these results are improved when STARLIGHT does not also have to model the kinematics of the input spectrum, we repeated these test, but with the velocity and dispersion fixed to the known input values. The results were entirely unchanged.

We also performed these same tests with $A_V = 0$ and $A_V = 0.8$ (instead of $A_V = 0.2$ as used above) to check that STARLIGHT is still able to recover populations in low- and high-extinction environments, and found the results to be unchanged here too.

5.6.3 Recovering of a known star-formation history

Finally, to simulate the effects of low SNR on a spectrum comprising multiple stellar populations (such as would be found in real galaxies), we created spectra of three different star-formation histories (SFHs) using the 66 E-MILES template SSPs. The different SFHs reflect different cases:

A: a flat SFH, where the star-formation rate is defined as $SFR(t) = 0.1\ M_{\odot}\mathrm{yr}^{-1}$ for all lookback times t;

B: a peaked and then declining SFH (as seen in many galaxies) with a star-formation rate represented by $SFR(t) = \left[0.2 + \mathcal{N}_{9.2}^{1.5}(\log(t))\right]\ M_{\odot}\mathrm{yr}^{-1}$, where $\mathcal{N}_{\mu}^{\sigma}(x)$ denotes a

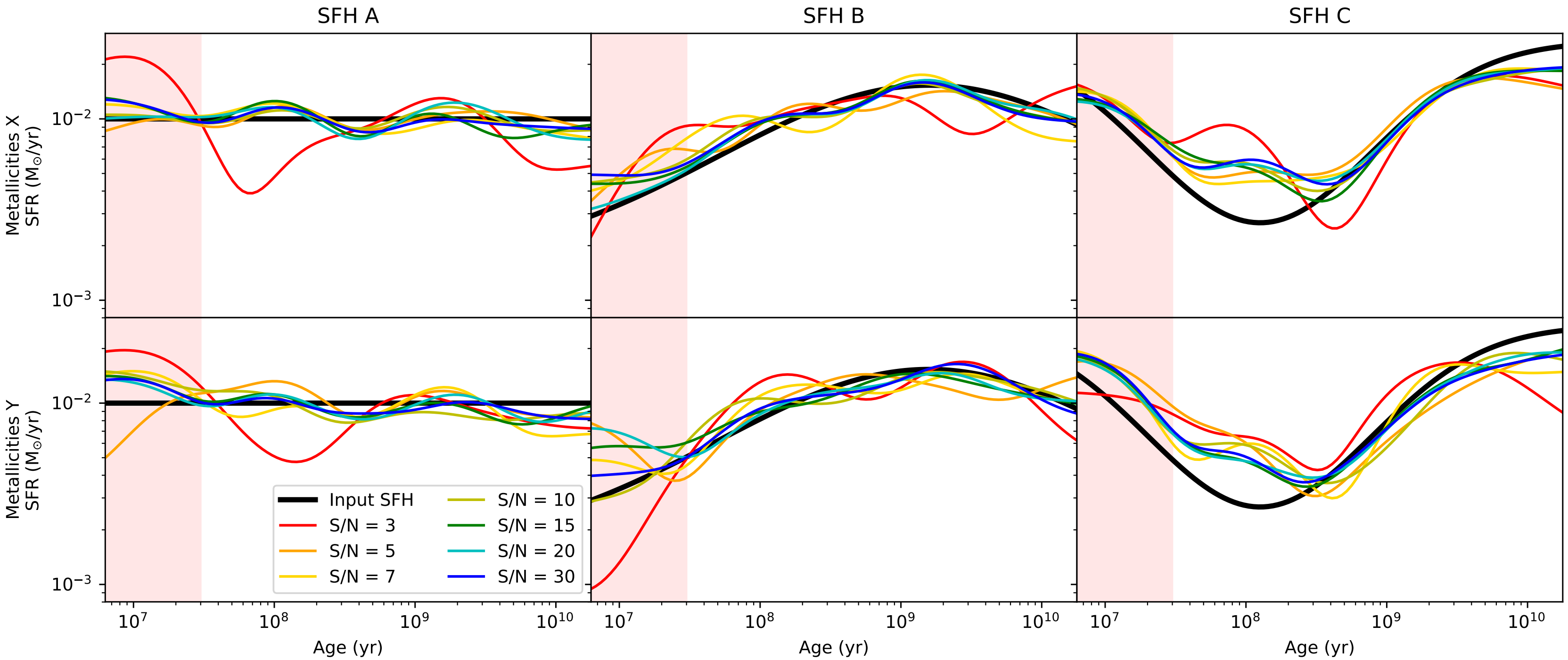

Figure 5.12: The measured SFHs for different input spectrum signal-to-noise ratios (coloured lines) compared to the input SFH shape (black line) for each SFH (*left* to *right*) and metallicity distribution (*top* and *bottom*). Recovered SFHs are smoothed by 0.3 dex. The red-shaded region indicates that for which SSP weights are ignored in science cases (see Section 5.5.4). The general shape is recovered well in all cases, particularly for signal-to-noise ratios greater than 5.

Gaussian function of x centred on $x = \mu$ with standard deviation of σ dex;

C: a declining and rejuvenating SFH with a star-formation history represented by $SFR(t) = \left[1.2 - \mathcal{N}_{8.1}^{0.8}(\log(t))\right]\ M_{\odot}\mathrm{yr}^{-1}$.

In building these SFHs, we assign weights to each SSP assuming that they represent all star-formation between their nominal age and the next-youngest SSP, as we did in Section 5.5.2.

We also included two different metallicity distributions which do not vary with stellar population age:

X: a flat distribution over the range of metallicities in the E-MILES templates, where the relative flux of each SSP of any given age is defined by $F_i = 1$;

Y: a peaked distribution where the relative flux of each SSP is defined at each age t by $F_i = \mathcal{N}_{-0.71}^{0.3}(\log(\mathrm{Z_i}/\mathrm{Z_{\odot}}))$.

These spectra were then degraded to different SNRs of S/N = 3, 5, 7, 10, 15, 20, and 30. When each of these 42 spectra of known SFHs were fit using Starlight, we found the general shape of $SFR(t)$ is recovered in all cases, as shown in Figure 5.12. For a SNR greater than 5 (the lowest typically found in the outskirts of MaNGA galaxies in the Primary or Primary+ samples), the derived SFHs show very good agreement (within 0.15 dex at all lookback times) to the input SFHs. This is also shown in Figure 5.13, where a simple χ^2 goodness-of-fit measurement is obtained between the input SFH and each of the recovered SFHs. Starlight is able to recover SFHs A and B for all cases with S/N $\geq$ 10, and while the measurement of SFH C is worse, it is recovered equally well for S/N $\geq$ 7 in metallicity distribution X and S/N $\geq$ 15 for metallicity distribution Y.

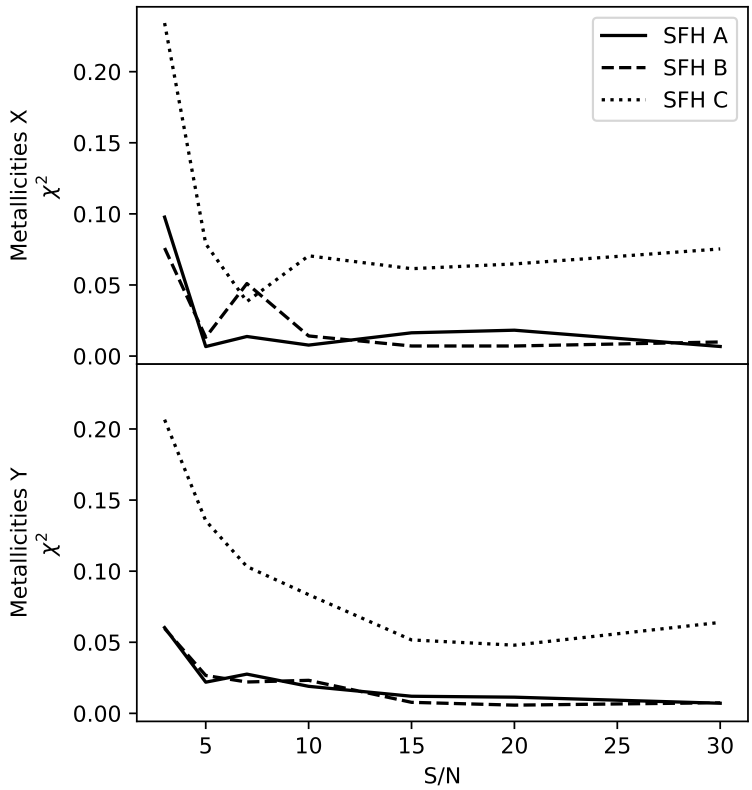

Figure 5.13: A χ^2 goodness-of-fit measurement of the input to the measured SFH in Figure 5.12, for each of the three SFH shapes (line styles) and metallicity distributions (*top* and *bottom*) for different input signal-to-noise ratios. Increasing S/N above 7 does very little to improve Starlight's ability to recover the SFH.

This test again highlights that, even when any given part of the spectrum may be dominated by noise, using such a long wavelength range allows STARLIGHT to still be able to infer a large amount of information from the entire spectrum. It also illustrates that, even when the systematic effects discussed in Section 5.6.1 are negligible, combining regions of an integral-field spectroscopic datacube into regions of high SNR does not necessarily improve the reliability of the fit in any significant way.

5.6.4 Implications

We assume throughout this thesis that the E-MILES model spectra are accurate representations of the stellar populations they represent. A full test of whether this is indeed the case is beyond this thesis, but the tests shown here imply that if this is true, we expect STARLIGHT to be able to recover the true SFHs under all the conditions analysed in this thesis. Notwithstanding this robustness, we must ensure that the low signal-to-noise regions of the galaxy are not affecting our results in ways we don't anticipate. Therefore, in all stages of our science analysis we ensure that we weight spaxels by their flux or mass in deriving results, thereby ensuring that the central regions (with higher SNR and therefore with probably good fits) are emphasised, and low signal-to-noise regions are down-weighted.

5.7 Example spaxel fits

Having assured ourselves that the fitting approach described here should provide reliable results, Figure 5.14 shows the STARLIGHT fits to four different spaxel spectra from the MaNGA galaxy with plate-IFU 8329-12701. Even in the spaxels at large radii and therefore with low signal-to-noise ratio, the residual spectrum shows no strong features;

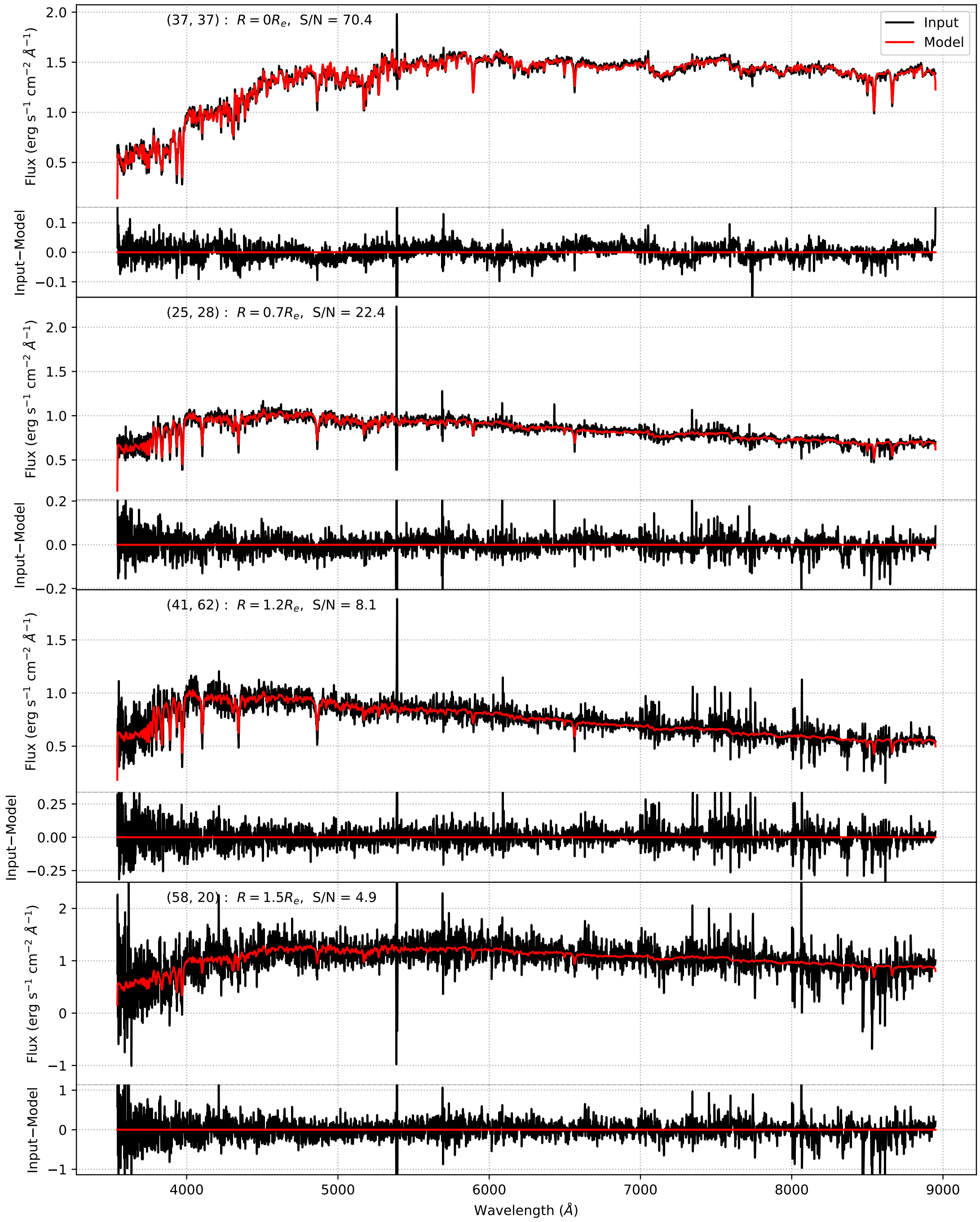

Figure 5.14: Emission-subtracted (black) and the STARLIGHT best-fit model spectra (red) for four different spaxels of the MaNGA spiral galaxy 8329-12701. The lower panels indicate the residuals from the model spectrum in flux units. The spectra shown are from spaxels at different coordinates, radii R, and signal-to-noise ratios S/N as indicated.

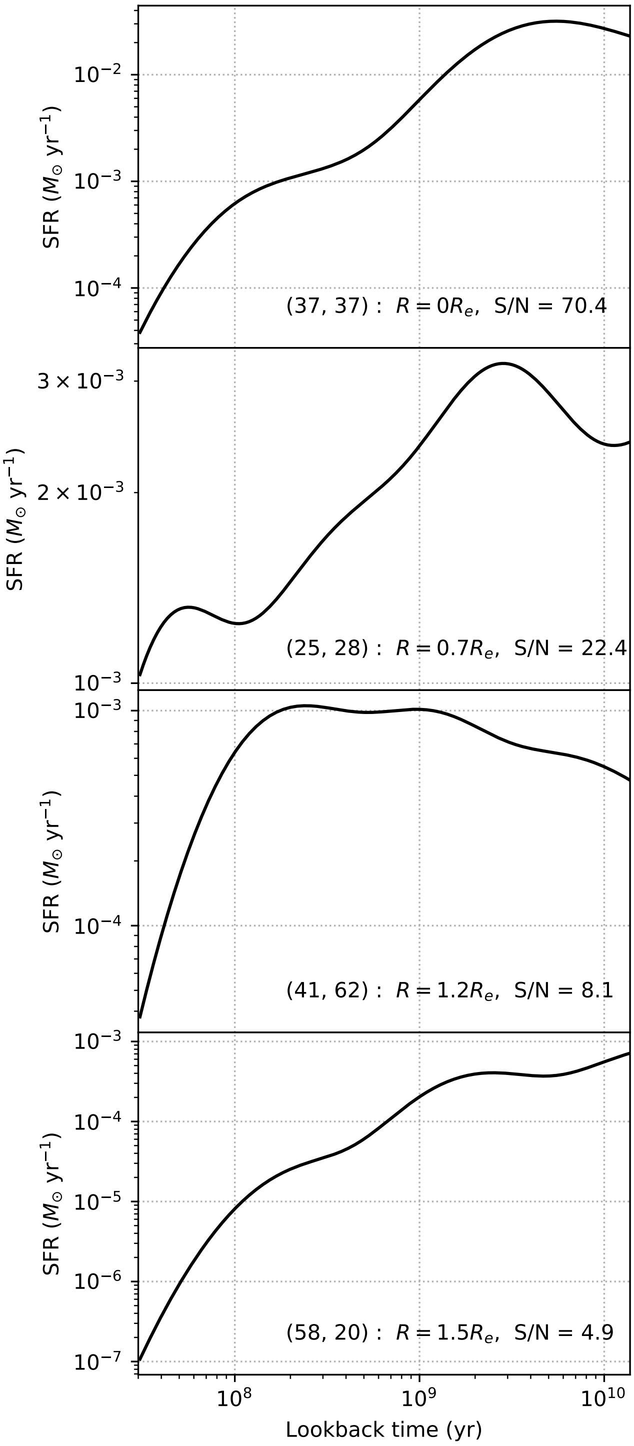

Figure 5.15: The 0.2-dex-smoothed star-formation histories derived from the fits shown in Figure 5.14.

the absorption lines are fit to the same standard as the continuum. The derived star-formation histories of these spaxel fits are shown in Figure 5.15.

5.8 Conclusions

We have outlined the details of the spectral fitting techniques which can be applied to a large sample of galaxies. We have shown that deficiencies in the SSP template spectra can result in unphysical star-formation histories and therefore unreliable measurements of the spatial distribution of stellar populations in galaxies. However, in the process, we showed that the uncertainties surrounding the treatment of the very youngest templates do not significantly impact the derived SFHs over other lookback times. We therefore concluded that until population libraries can accurately model the UV upturn, the best approach in future applications is to allow the youngest populations to be used in the fits, but ignore the weights attributed to them in subsequent analysis. We also showed that Starlight is able to both recover single stellar populations and measure star-formation histories under a large range of conditions — including signal-to-noise ratios as low as 5 — so fitting individual spaxels will not significantly impact any results.

Chapter 6

Excavating the fossil record of stellar populations in spiral galaxies

The growth of galaxies of all types is thought to generally occur “inside out”. In this scenario, the mass that galaxies add over time is built up on their outskirts, causing a measure of half-light or effective radius to increase substantially over time. This model has been backed up by cosmological simulations, and observations of galaxies at different redshifts. However, this growth is expected to leave specific signatures in the stellar population fossil record; in the absence of significant stellar migration, any given galaxy’s outskirts would comprise only young stars, while the central regions would be dominated by older populations. Pushing this picture further, the detailed composition of stars of different ages as a function of radius would provide a measurement of how fast a galaxy has grown over time in both mass and physical size.

We have now established that time-slicing methods can successfully be used to study spiral and bar structures in individual nearby spiral galaxies. We have also detailed and tested a robust implementation of stellar population fitting which can be applied to a large sample of galaxies. By combining the power of these analysis techniques with the large sample size of MaNGA, we therefore now take the next step and study the fossil records of a sample of spiral galaxies. In this chapter, we study the signatures of disk growth in $\approx$ 800 spiral galaxies contained in the fossil record, using time-slicing techniques.

6.1 Introduction

Understanding how, when, and where galaxies built their mass is key to cosmology and astronomy. Analysis of the evolution of the masses and sizes of galaxies has generally been limited to comparisons of different galaxy populations at different redshifts. Studies done in this manner have shown that galaxies have grown in radius whilst building their mass (e.g. Trujillo et al. 2007; van der Wel et al. 2008; van Dokkum et al. 2008, 2013; Patel et al. 2013; Papovich et al. 2015; Whitney et al. 2019), giving rise to the concept of "inside out" formation. It is thought that such growth in the most massive galaxies has been due to some combination of multiple minor mergers (Naab et al., 2009; Furlong et al., 2017), gas accretion (Conselice et al., 2013), and quasar feedback (Fan et al., 2008). These approaches have given us a good insight into how the average properties of galaxies have evolved over cosmic time, but because we cannot track the evolution of any individual system in this way, it is difficult to go beyond such global properties. Although some studies of galaxies at different redshifts have managed to show inside-out growth in disk-like galaxies (e.g. Trujillo et al. 2006; Patel et al. 2013), most are restricted to the highest mass galaxies, so this picture of inside-out growth is normally limited to early-type galaxies.

An alternative approach which is more suited to late-type galaxies is to explore the stellar populations in different regions of a galaxy, particularly through studying how the mean stellar age varies with radius. This requires high-quality spectral data at multiple locations across the face of a galaxy, and so has only been undertaken in detail for large numbers of galaxies since the advent of integral-field spectroscopic surveys such as the Calar-Alto Legacy Integral Field Array (CALIFA; Sánchez et al. 2012), Sydney-AAO Multi-object Integral field spectrograph (SAMI; Croom et al. 2012), and MaNGA surveys. Using such a “fossil record” approach applied to integral-field spectroscopic data has revealed that most galaxies exhibit negative age gradients (e.g. Mehlert et al. 2003; Sánchez-Blázquez et al. 2014; González Delgado et al. 2015; Goddard et al. 2017) — with younger outskirts than centres — or earlier formation times of the central regions (e.g. Ibarra-Medel et al. 2016) providing more evidence for a dominant “inside out” growth mode occurring in galaxies of all Hubble types. This is also backed up by Sacchi et al. (2019) for the case of NGC 7793, who find that broad-band observations of resolved stellar populations in this nearby spiral galaxy indicate a clear gradient in stellar age.

By applying stellar population modelling methods to integral-field spectroscopic data from the CALIFA survey, Cid Fernandes et al. (2013, 2014), Pérez et al. (2013), González Delgado et al. (2017), and García-Benito et al. (2019) have shown that it is possible to reveal much more about a galaxy’s history by deriving full star-formation histories rather than mean ages. We have shown previously that such analyses of the spatial variation in stellar populations of spiral galaxies can help us understand the structure of the spiral arms and bars, but here we investigate how such approaches can also help us study the evolution and growth of populations of galaxies.

Comparative studies of the masses and sizes of galaxies at different lookback times are most effective to measure the growth of early-type galaxies since these are typically the most massive and luminous objects at any given redshift so are easy to identify. By contrast, a fossil record analysis acts as a complementary approach best suited to — but by no means limited to; see e.g. Lacerna et al. (2020) — studying the growth of late-type galaxies, as such galaxies have in general had continued growth over the last several Gyr, where archaeological methods are most sensitive. Of course, there exists a population of spiral galaxies which are passive (see for example Masters et al. 2010; Fraser-McKelvie et al. 2016) — contrary to the well-known relation between the morphology and star formation rate (Tully et al., 1982; Baldry et al., 2004) — so a morphological classification does not always define the extent of the star-formation history of each galaxy. However, for consistency, we have chosen to study a galaxy population selected on their morphology rather than colour, to better understand how this well-defined galaxy class have evolved over time.

In this chapter, we perform full spectral fitting of spiral galaxies from the MaNGA survey (Bundy et al., 2015) and measure spatially-resolved star formation histories, to uncover their formation sequences. In Section 6.2, we outline the data we use from the MaNGA survey and Galaxy Zoo. In Section 6.3 we describe how a sample of spiral galaxies from the MaNGA target list was selected. We then explain how the derived star-formation histories are processed in Section 6.4. The mean age and metallicity gradients are derived in Section 6.5. In Sections 6.6 and 6.7 we analyse the star-formation histories and spatially-resolved stellar populations in more detail, and infer the evolution of the mass–size relation in Section 6.8. Finally, we discuss the interpretation and context of the results in Section 6.9.

6.2 Data

6.2.1 MaNGA

The MaNGA product launch 8 (MPL-8) internal data release contains completed observations of 6778 galaxies, providing a large sample of galaxies of all Hubble types.

In this work, we make use of some of the analysis outputs of MaNGA's data analysis pipeline (DAP; Westfall et al. 2019; see Section 2.1.5) for MPL-8. Specifically, we use the measured stellar velocities $V_{\star}$, deprojected radii R, and emission line spectra, all of which are derived using full spectral modelling. Since this chapter contains analysis of a full sample of spiral galaxies from MPL-8, we make extensive use of the MaNGA sample weightings, which are described in more detail in Section 2.1.2.1.

6.2.2 Galaxy Zoo

We also make use of the morphological classifications of each MaNGA galaxy provided by volunteer "citizen scientists" as part of Galaxy Zoo (Lintott et al., 2008, 2011). The second phase of the project (Galaxy Zoo 2, hereafter GZ2; Willett et al. 2013) includes publicly-available detailed classifications of galaxies based on SDSS DR7 imaging. The users' classifications are weighted and combined to obtain a consensus fraction for each answer to each question for each galaxy, using methods described by Willett et al. (2013) and Hart et al. (2016). We use the redshift-debiased and user-weighted probabilities — which we denote as $p_{\text{classification}}$ — from the Hart et al. (2016) catalogue.

6.3 Sample selection

A sample of spiral galaxies was drawn from the MPL-8 data release using the recommendations of Willett et al. (2013, Table 3); see also Masters et al. 2019 for another recent implementation. We first remove the 45 galaxies in the matched MPL-8/GZ2 catalogues that more than 50% of GZ2 users have classified as having some form of star or artifact in the image. To filter out elliptical galaxy morphologies, we select the 4201 galaxies with $p_{\text{features or disk}} > 0.43$ and at least 20 classifications in this question, as recommended by Willett et al. (2013).

Since we are interested in the variation in stellar population properties across the face of each spiral galaxy, we remove edge-on galaxies from this sample. This cut can be made with either the GZ2 classifications — specifying $p_{\text{not edge-on}} > 0.8$ — following Willett et al. (2013), or using an axis ratio cut — requiring $\frac{b}{a} \geq 0.4$ — following Hart et al. (2017a). To select only face-on galaxies, we choose galaxies that satisfy the Willett et al. (2013) criterion and have an axis ratio of $\frac{b}{a} \geq 0.5$ (corresponding to an inclination of $i \leq 60°$ assuming the galaxies can be modelled as a thin intrinsically circular disks). We used this higher axis ratio cut compared to that used by Hart et al. (2017a) to ensure that we have selected only galaxies for which the radial structure is clearly resolvable with MaNGA. Of the 5902 MPL-8 galaxies for which GZ2 classifications are available, this leaves a sample of 1686 close-to-face-on disky galaxies. Of these, 1314 galaxies satisfy the Willett et al. (2013) requirement for spiral galaxies of $p_{\text{spiral}} > 0.8$ and 20 individual classifications in this question.

We then remove 109 galaxies which have flags for bad or questionable-standard data in the MaNGA DRP, or for which the MaNGA MPL-8 DAP dataproducts are unavailable. To ensure consistency in the spatial resolution relative to the galaxy size, we remove galaxies which are part of MaNGA's Secondary sample (see Chapter 2). For the final sample of spiral galaxies, we therefore select only those 795 which are in the Primary+ MaNGA sample, for which MaNGA observations extend to at least 1.5 R_e. The median redshift of galaxies in our sample (weighted by the MaNGA Primary+ sample weighting) is $z = 0.026$, and 75% of the (weighted) sample are at redshifts $z < 0.03$. The MaNGA observations typically therefore reach to around 8 kpc in radius, depending on the intrinsic size of the galaxy.

6.4 Spectral fitting and time slicing

We fit each spaxel of each galaxy in the sample using the method developed and outlined in Chapter 5. From the SSP template weights obtained in the STARLIGHT fits, we are able to reconstruct the star formation history (SFH) and metallicity distributions at every location in each galaxy in the spiral sample. From the SFHs, it is straightforward to reconstruct an image of the total flux emitted by — or mass contained in — stars of any given age. To ensure that we are not over-interpreting small-scale noise in the age-distributions of weights assigned to individual templates, we first smooth the SFHs before any analysis is done on these images. We have smoothed the distribution of template weights by 0.3 dex in age, but smoothing by any factor between 0.2 and 0.5 dex does not affect results significantly.

As an illustration, Figure 6.1 shows an animation of a single galaxy (MaNGA plate-IFU 8329-12701) from the spiral sample, stepping through stellar population ages from 17 Gyr down to 30 Myr, highlighting the wealth of information contained in the spatially-resolved SFHs available using STARLIGHT and MaNGA. Such animations can be made for any of the galaxies in the sample, but here we show an example of a galaxy observed using the largest-sized (127-fibre) IFU to demonstrate the amount of information potentially available through such time slicing.

It is worth emphasising that we can only measure the current location of stars in the galaxy, so that we can only treat a "time slice" at any given stellar age as an approximation of the structure of the galaxy at that time, since we cannot undo the effects of dynamical heating or radial mixing and migration. However, Martínez-Lombilla et al. (2019) showed that the shape of vertical colour gradients seen in edge-on disk galaxies imply that radial migration occurs at a slower rate than the intrinsic growth of the galactic disk. Simulations of galactic disks also suggest that stellar populations are in general

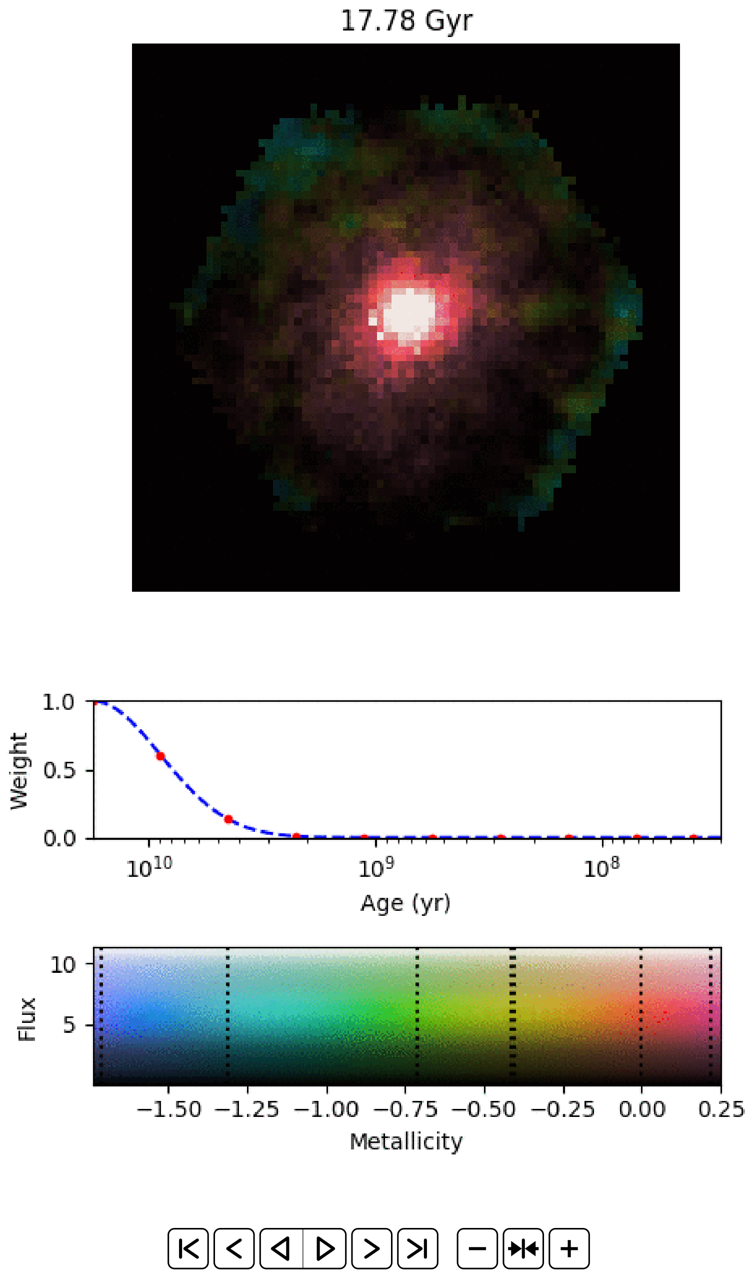

Figure 6.1: Similar to Figure 4.2, but for MaNGA plate-IFU 8329-12701. *Top*: Animation of a MaNGA spiral showing the spatially resolved flux (colour-coded by the metallicity) of stars as a function of age, from 10 to 0.03 Gyr. *Middle*: Weighting function used. The STARLIGHT output is smoothed to 0.3 dex in stellar age. Red points indicate the SSP ages used. *Bottom*: Colour map indicating the flux (in units of 10^{-14} erg s^{-1} cm^{-2} Å^{-1} spaxel^{-1}) and metallicity (in units of $\log(Z/Z_{\odot})$) of the stellar population. Dashed vertical lines indicate the SSP metallicities used.

equally likely to migrate inwards or outwards (Avila-Reese et al., 2018), and only by sufficiently small distances that this effect has only minor effects on the radial distribution of populations (Avila-Reese et al., 2018; Navarro et al., 2018; Barros et al., 2020), so here we assume that the current distribution of a given stellar population is — to a first approximation — representative of the distribution of star formation in the galaxy at the corresponding lookback time.

Clearly this assumption does not hold true for spiral structures, since such distributions will become diluted rapidly with the disk's rotation. However, for the youngest stellar populations, we showed in Chapter 4 that interpreting spatially-resolved star-formation histories in this "time-slicing" approach can help to understand spiral arms and bars. Mallmann et al. (2018) also showed that a similar approach can be used to understand the properties of AGN, and other studies with CALIFA showed that this approach can offer clues to the history of a galaxy's radial profile (Cid Fernandes et al., 2013, 2014; Pérez et al., 2013; González Delgado et al., 2014).

6.5 Mean ages and metallicities

A first-order measurement of the SFHs resolved across the face of a galaxy is that of the mean age or — with a similar calculation — of spatially-resolved metallicity. Using the mass weights assigned to each SSP template by Starlight in the fits for each spaxel spectrum, we derive mass-weighted mean log(age) and log(metallicity) maps for each galaxy like the one shown in Figure 6.2. We then plot the light-weighted median of all spaxels' mean log(age) and log(metallicity) within radial bins of width 0.045 R_e (where R_e is the elliptical Petrosian effective radius measurements from the NSA) against the elliptical galactocentric radius R (in units of R_e), and find a best-fit straight line to these data using a least-squares fit. The fitting is only performed out to 1.2 R_e to avoid the edges

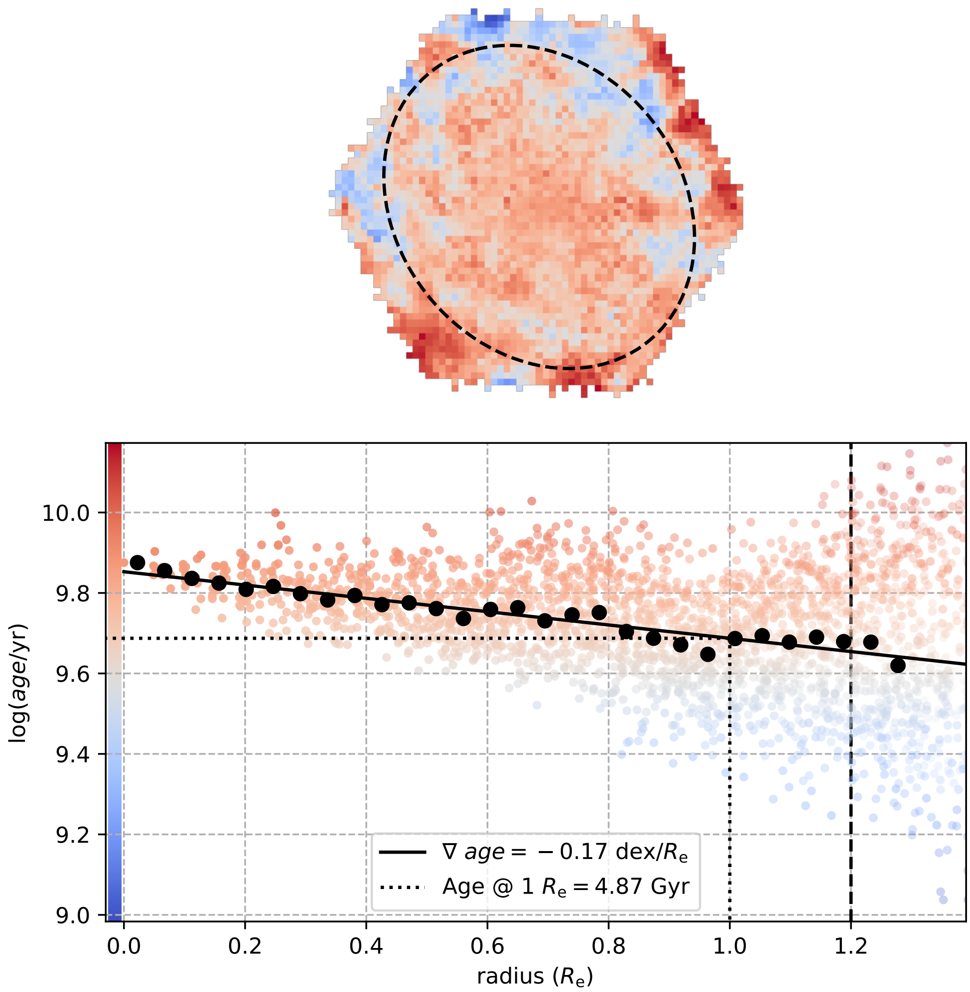

Figure 6.2: A map of the light-weighted mean log(age) (*top*) for a single galaxy (MaNGA plate-IFU 8329-12701). The dashed ellipse denotes 1.2 R_e, and the colour scale is indicated against the y-axis of the *bottom* panel. The values of this map are plotted against radius (*bottom*), where the colours and opacities of the spaxel points represent their mean ages and total contained flux respectively. The median spaxel value within radial bins of width 0.045 R_e (where each spaxel is weighted by its contained flux) is shown as black circles. The best-fit straight line to these points is shown as a black solid line. This line's gradient (−0.17 dex/R_e) and value at 1 R_e (4.87 Gyr, indicated by black dotted lines) are used in Figure 6.3. The vertical dashed line indicates the maximum radial limit of the region within which the best-fit straight line is calculated.

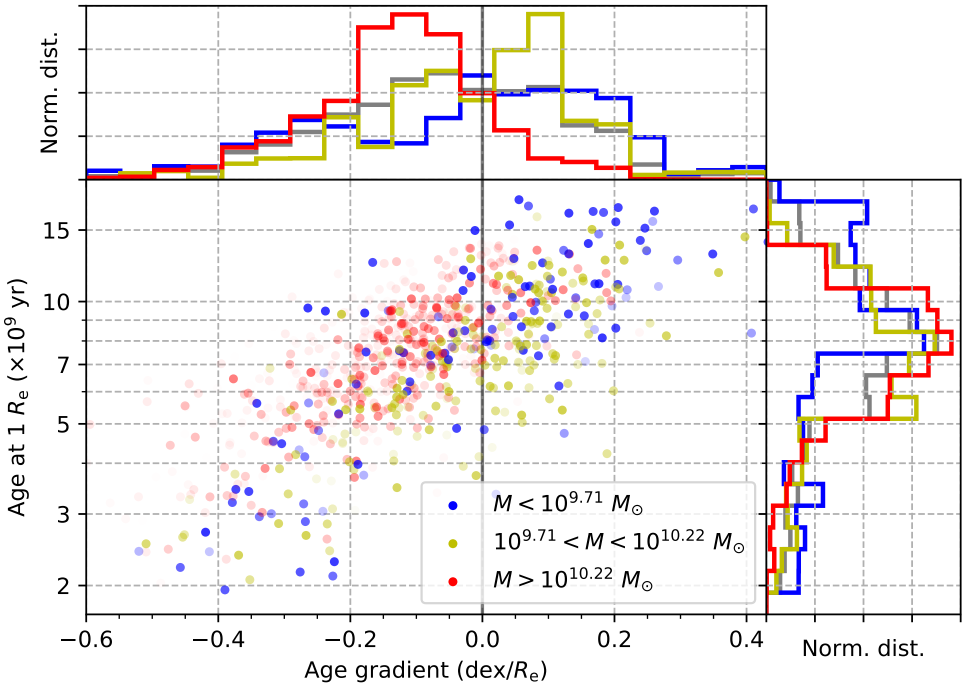

Figure 6.3: Mass-weighted mean ages at 1 R_e (*vertical axis*, where R_e is the elliptical Petrosian radius measurements from the NSA) and mean age gradients (*horizontal axis*) for each galaxy, coloured by the galaxy's total stellar mass. Each data point's transparency is defined by the MaNGA Primary+ sample weighting. The weighted histograms at the *top* and *right* indicate the distributions of ages and their gradients respectively, where the grey line indicates the distribution of the whole sample and the coloured lines indicate those for each of the three mass bins.

of the hexagonal-shaped IFU FOVs and to ensure consistency between galaxies. From these best-fit lines, we obtain a mean age and metallicity gradient, and a characteristic age and metallicity value of the stellar populations located at 1 R_e, a measure which Sánchez et al. (2016b) showed to be representative of the galaxy as a whole. This process is illustrated for a single spiral galaxy (MaNGA plate-IFU 8329-12701) in Figure 6.2.

The distributions of age gradients and ages at 1 R_e are shown in Figure 6.3, and equivalent metallicity measurement in Figure 6.4. We find that, on average, a majority (approximately 60%) of the spiral sample exhibit slight negative age gradients, implying younger outskirts. This agrees with the general picture found by others (Sánchez-

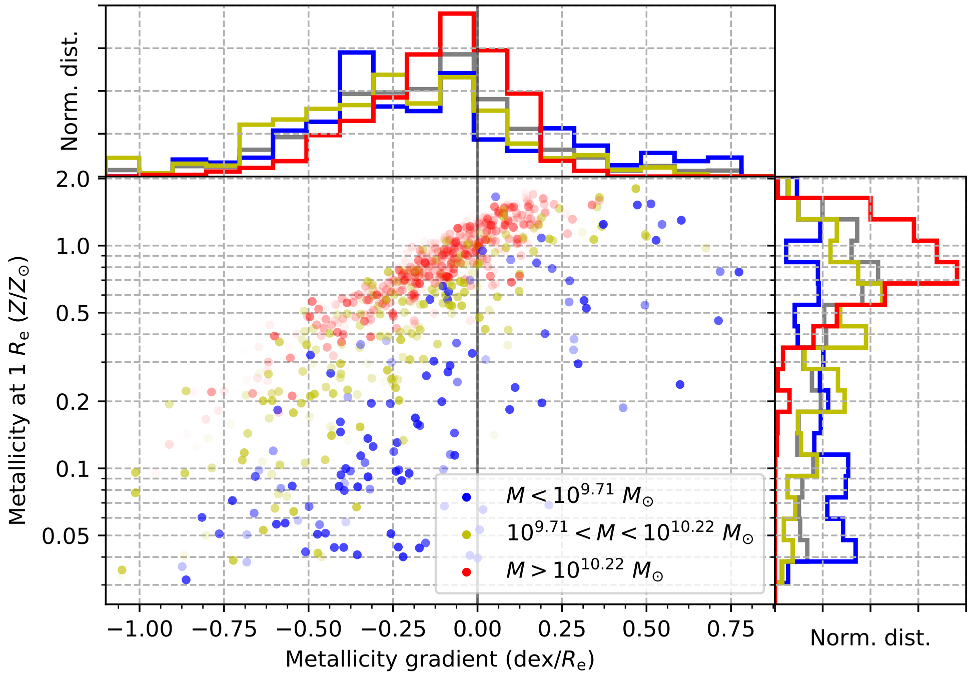

Figure 6.4: As Figure 6.3, but for mass-weighted mean metallicities and their gradients.

Blázquez et al., 2014; González Delgado et al., 2015; Zheng et al., 2017; Goddard et al., 2017) and is usually taken to be evidence for inside-out formation being dominant in the most massive galaxies. When the sample is split into three mass bins (of $M < 10^{9.71}$ $M_\odot$, $10^{9.71} < M < 10^{10.22}$ $M_\odot$, and $M > 10^{10.22}$ $M_\odot$[1]), we find that the approximately 80% of the highest-mass galaxies exhibit negative age gradients while only 50% of the lowest-mass galaxies galaxies do. This difference suggests that inside-out formation is more dominant in high-mass galaxies.

We find that most ($\approx 60 - 80\%$) galaxies in all mass bins also exhibit slight negative metallicity gradients, and Figure 6.4 highlights a strong mass-metallicity correlation too, as first suggested by Lequeux et al. (1979).

[1]The mass bin thresholds used here were chosen such that a volume-limited sample of spiral galaxies selected in the method described in Section 6.3 would contain equal numbers of galaxies in each bin, determined using the "EWEIGHT" sample weighting for the Primary+ MaNGA sample.

6.6 Mass buildup times

Measuring only a mass-weighted mean age or metallicity does not make use of all of the available information in the age distribution of SSP template weights. From a full spectrum fitting approach, it is also possible to use the width of the distribution in stellar age, as well as its mean value. To this end, from a given smoothed SFH, we define the time T_{95} by which 95% the total stellar mass of that spectrum was built up. We measure a T_{95} for all light within $R < 1.2\ R_{\rm e}$ of each galaxy. We find that T_{95} correlates with the total stellar mass of the galaxy, as shown in Figure 6.5: all galaxies with present-day stellar masses within 1.2 $R_{\rm e}$ of $M_\star \geq 2 \times 10^{10} M_\odot$ formed the bulk of their mass at least 5 Gyr ago, while most of those with stellar masses $M_\star \leq 10^{10} M_\odot$ were still building their mass as recently as $\approx$ 2 Gyr ago. This effect is reflected in the known relation between the stellar mass and star formation rates in galaxies, and the results shown here agree well with other fossil record studies (Thomas et al., 2010; Pacifici et al., 2016), empirical modelling (Rodríguez-Puebla et al., 2017; Behroozi et al., 2019), and theoretical modelling (Henriques et al., 2015; Hill et al., 2017) including previous analysis of MaNGA galaxies (Ibarra-Medel et al., 2016). There is a population of low-mass spiral galaxies with large values of T_{95}, but no equivalent population of high-mass galaxies with small build-up times, highlighting that low-mass spiral galaxies have had more varied histories than their high-mass counterparts, as found by Ibarra-Medel et al. (2016).

Using the spatial information available with MaNGA, we are also able to measure how the local value of T_{95} varies with galactic radius R in galaxies of different masses, using the same total stellar mass bins as in Figures 6.3 and 6.4. In Figure 6.6, T_{95} for each spaxel in the sample of spiral galaxies plotted against the galactocentric radius shows that the stellar populations currently at the centres of high-mass galaxies formed

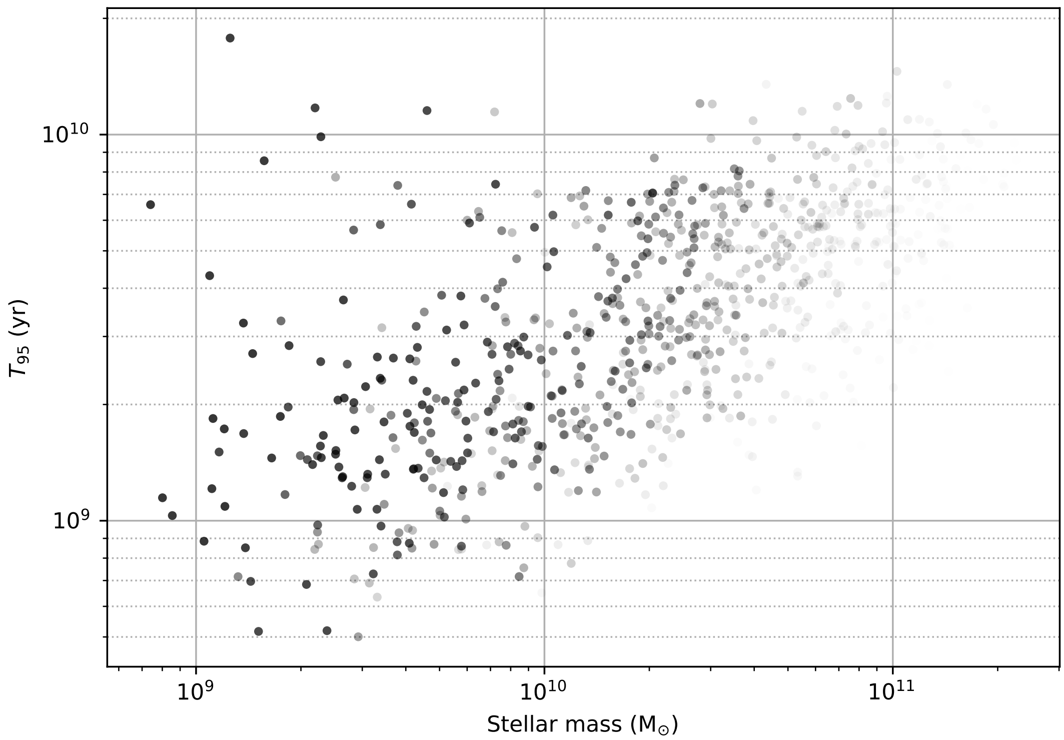

Figure 6.5: Time since 95% of the total stellar mass within 1.2 R_e had been assigned in the STARLIGHT fits (T_{95}) for galaxies of different present-day stellar masses. All spiral galaxies with high present-day mass built the bulk of their mass at early times, but most low-mass galaxies were building their mass more recently. The transparency of each point is defined by the galaxy's MaNGA Primary+ sample described in Chapter 2.

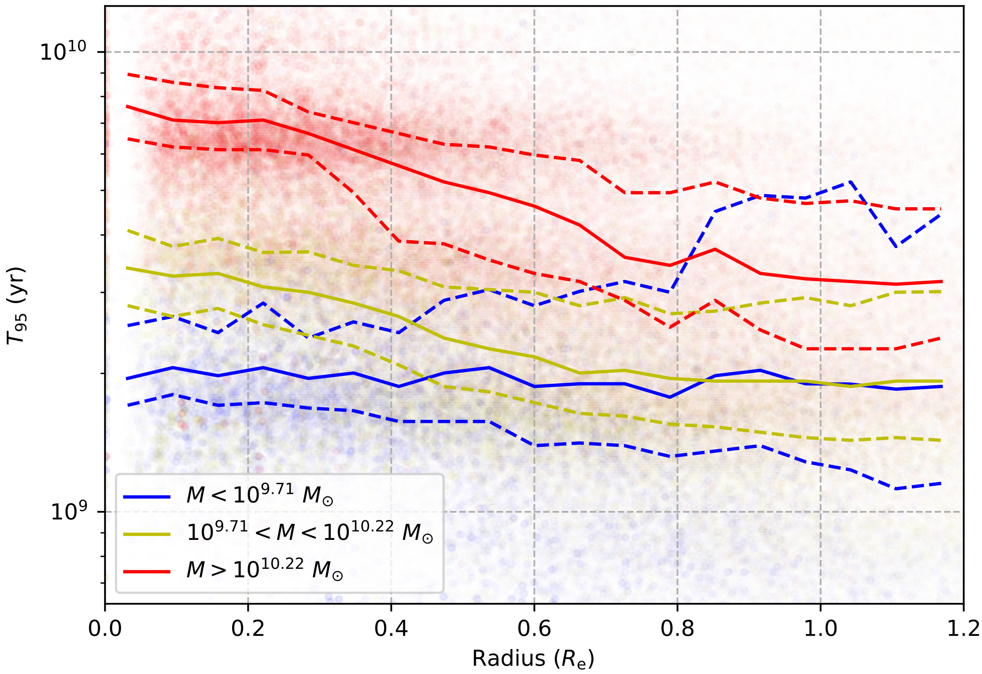

Figure 6.6: Time since 95% of the stellar mass built up (T_{95}) in each spaxel of each galaxy in the spiral sample. Each spaxel in each galaxy is shown as a point, with the opacity defined by the product of the total spaxel flux and the galaxy's MaNGA Primary+ sample weight. Colours denote the galaxy's total present-day mass. Solid lines represent a weighted running median, and dashed lines are one-third and two-third weighted percentiles. The outskirts of galaxies of all masses built up at approximately similar times, but the centres of massive galaxies formed significantly earlier than those of low-mass galaxies.

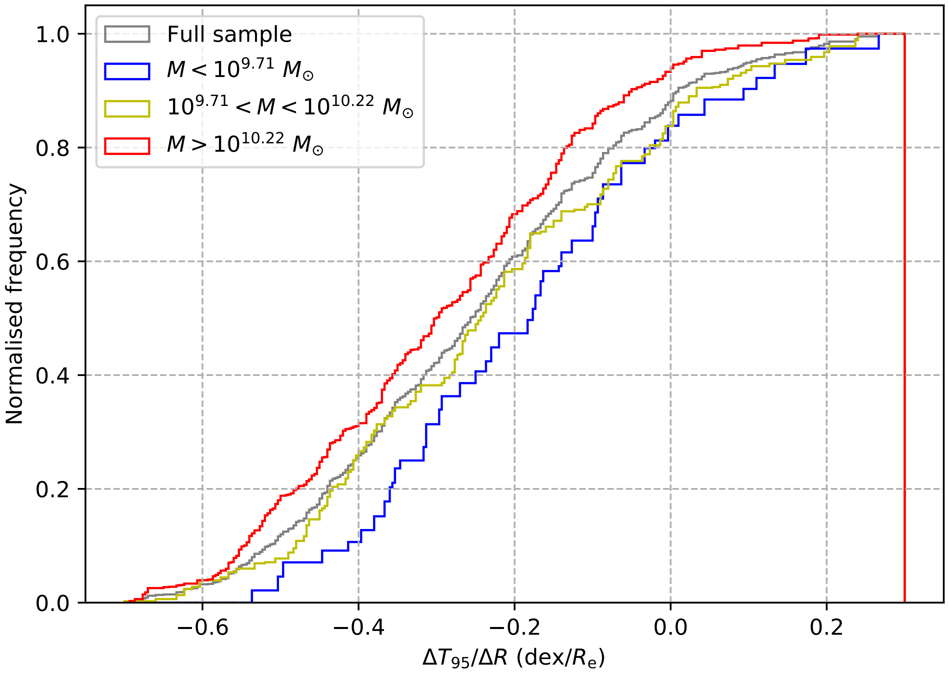

Figure 6.7: Distribution of gradients of T_{95} vs. galactic radius R for galaxies of different masses. Most galaxies show evidence for inside-out formation, and the effect is strongest in high-mass galaxies.

on average significantly earlier (by ≈ 0.7 dex or a factor of 5) than those in low-mass galaxies. By contrast, the galaxy's outskirts built up at approximately the same time regardless of the mass of the host galaxy: at $\approx 1\ R_e$, the discrepancy in T_{95} is much less, at ≈ 0.3 dex (or a factor of 2).

To quantify this effect, we obtained a straight-line fit to the radial profiles of $\log(T_{95})$, weighting spaxels by their flux. We find that the majority of galaxies ($> 80\%$) in each mass bin show a negative gradient, as we show in Figure 6.7, implying younger outskirts than galactic centres. Assuming that the stellar populations of any given age have not significantly migrated since their birth, this is evidence for inside-out growth occurring in the great majority of spiral galaxies. We find strongest evidence in the highest-mass galaxies, for which $> 90\%$ exhibit negative gradients in T_{95}. These results are consistent with the mean age gradient analysis of Section 6.5, which is not surprising since both approaches are measures of the age distributions contained within the derived SFHs. However, directly determining a quantity such as T_{95} is returning something much closer to a physical measurement of how the mass of the galaxy has built up over time.

When a 90%, 75% or 50% threshold was used instead of the 95% threshold results shown here, we found no change to the qualitative conclusions. The higher 95% threshold was used to ensure that the buildup time of more galaxies and spaxels was within the range $0.8 \gtrapprox T_{95} \gtrapprox 5$ Gyr where spectral fitting methods are most sensitive, and avoids saturation at either extreme of the stellar age range we are able to measure.

6.7 Concentration of stellar components

Another more physically-motivated way to expand beyond measuring mean age gradients to infer the radial build-up of spiral galaxies is to analyse the spatial extent of individual stellar populations of different ages. We showed in Chapter 4 that it is possible to measure such distributions directly using time-slicing techniques. The animation in Figure 6.1 suggests systematic variation in how concentrated the stellar populations are in one particular spiral galaxy. Older populations are most centrally-concentrated in the bulge regions of the galaxy while the younger populations make up the more extended disk. This illustrates the general consensus of the cores of galaxies having older ages than the surrounding disks.

To quantify the variation in spatial extent of different stellar populations in the full galaxy sample, we choose to measure a concentration of each stellar population in each spiral galaxy. A concentration can be defined in a number of ways [for example as defined by Conselice (2003)] which often require a larger FOV than MaNGA offers in order to measure a background flux. Here we define the concentration c of a population of stellar age t as

$$c(t) = \frac{m_{r \leq 0.5 R_{\mathrm{e}}}(t)}{m_{r \leq 1.2 R_{\mathrm{e}}}(t)} \tag{6.1}$$

where $m_{r \leq k \mathrm{R}_e}(t)$ is the mean mass contained in all spaxels within $k \times \mathrm{R_e}$ using the R_{e} elliptical Petrosian radius values of each galaxy from the NASA-Sloan Atlas (Blanton et al., 2011). This measure ensures that the extent of each population is scaled by the size of the present-day galaxy, and only requires data from within the MaNGA footprint.

The concentration c of stellar populations of different ages in each galaxy in the full sample is shown in Figure 6.8. There is a clear trend of older populations being most centrally-concentrated (with typical values of $c \approx 2.5$ at $t \geq 2$ Gyr), and the younger stars in all galaxies exhibiting the most spatially extended distributions (with $c \approx 1$ at $t \leq 0.1$ Gyr). This is unsurprising since this is simply a different way of presenting and interpreting the same effects as in Section 6.6, but in a manner that utilises more of the temporal information available to illustrate how radial gradients in mass-to-light ratios (e.g. García-Benito et al. 2019) are created.

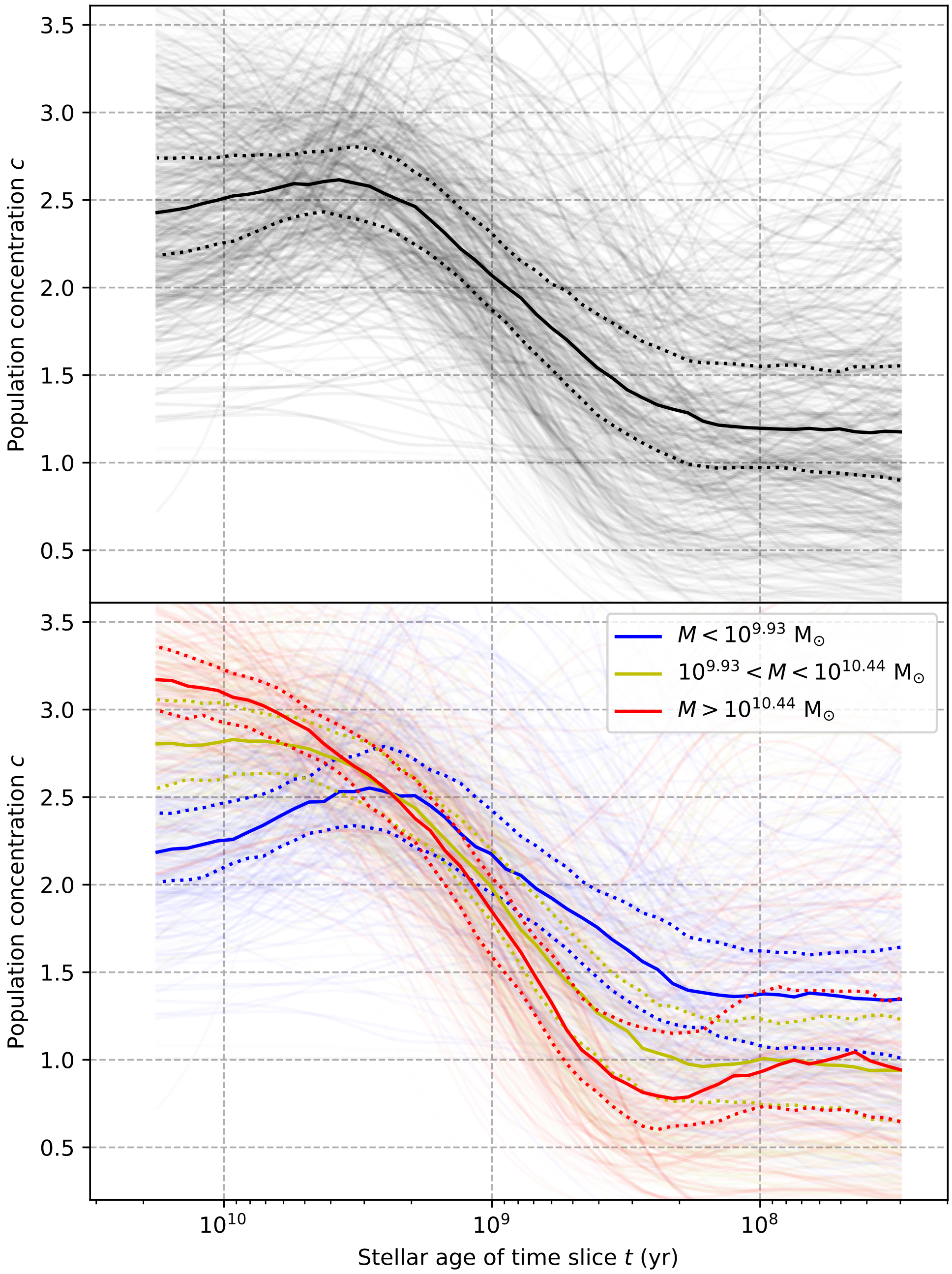

Figure 6.8: Population concentration c of each galaxy's stellar populations in the spiral sample as a function of stellar age, where c at each time slice is defined by Equation 6.1. Each galaxy's line is weighted by its MaNGA Primary+ weighting. The heavy line shows the weighted median of all galaxies, and the dotted lines indicate the weighted one-third and two-third percentiles. *Top*: All galaxies. *Bottom*: The same, but with galaxies coloured by their total (present-day) stellar mass. The youngest stellar populations are more spatially extended than the oldest populations in all galaxies, with the effect strongest in higher-mass galaxies.

We find that there is a strong dependence of $c(t)$ on total (current) galactic stellar mass. Using the same mass bins as in Figures 6.3 and 6.4, we find that in the highest-mass galaxies, the oldest ($\gtrapprox$ 6 Gyr) stellar populations are almost three times more concentrated than the youngest populations ($\lessapprox$ 0.1 Gyr), while in the lowest-mass galaxies this ratio is less than two.

By repeating this analysis using the mean 4020 Å flux mass in the definition of $c(t)$ (i.e. replacing $m_{r \leq kR_{\mathrm{e}}}(t)$ with $f_{r \leq kR_{\mathrm{e}}}(t)$) in Equation 6.1), the results are unchanged. This is unsurprising since the radial variation in mass-to-light ratio is unlikely to be significant for any single time slice t.

This analysis reenforces the conclusion that inside-out growth is the primary formation mode in the majority of spiral galaxies, and that the effect is strongest in higher-mass galaxies.

6.8 Mass–size distribution

Although the mass buildup times in Section 6.6 and the variation in concentration in Section 6.7 both show evidence for inside-out formation being the dominant growth mechanism in spiral galaxies, these analyses are still not directly comparable measurements to those used in most studies over different redshifts. Previously, observational evidence for inside-out formation in galaxies has come from analysing how the masses and sizes of galaxies increase simultaneously over time, by measuring these properties of different populations at different redshifts (e.g. van der Wel et al. 2008; Maltby et al. 2010; van der Wel et al. 2012; van Dokkum et al. 2013; Patel et al. 2013; van der Wel et al. 2014; Papovich et al. 2015; Whitney et al. 2019). This comparison is something that can be directly made using time-slicing methods with integral field spectroscopy for a single galaxy population, to understand how the total mass and size growth has occurred over time.

6.8.1 Deriving integrated half-light and mass measurements

At each stellar age t, we define the stellar mass to be the sum of the masses in all populations with ages $\geq t$ within 1.2 R_e, using the smoothed distribution of weights from Starlight. We can also define a measurement $r_l(t)$ of the light size of a time slice t as being the radius of half the light contained within 1.2 R_e (using R_e elliptical Petrosian radius measurements from the NSA) of all of the light emitted by stars older than t. This definition is used since the MaNGA observations are limited in their fields of view. This limitation prohibits us from reliably measuring a sky background, forbidding a direct half-light radius measurement in a normal approach.

To ensure that the radius and stellar mass measurements defined here using the Starlight fits are reliable, we compare these measurements for the present-day galaxy (i.e. $t = 0$) with the known size and mass measurements of the galaxies in the NSA (see Figure 6.9). We find that r_l is a good proxy for the NSA elliptical Petrosian half-light measurements, with an offset of ≈ 0.2 dex which is a consequence of both the limited MaNGA FOV and the difference in wavelengths used. (The NSA radii are measured in the r band imagery, but the measurements for the Starlight outputs are done on a model 4020 Å image, which would be located in the g band.) We also find that the total stellar masses determined by Starlight are consistent with the photometry-derived masses in the NSA. Both mass measurements assume the same IMF, so a small observed offset is likely due to MaNGA's limited FOV.

Maltby et al. (2010) and van der Wel et al. (2014) showed that, unlike the early-type galaxies, the mass–size relation for spiral galaxies is weak.[2] However, using the

[2]The mass–size relations measured by these works use different methods for measuring galaxy radii. They are therefore not quantitatively comparable so are not shown in Figure 6.9

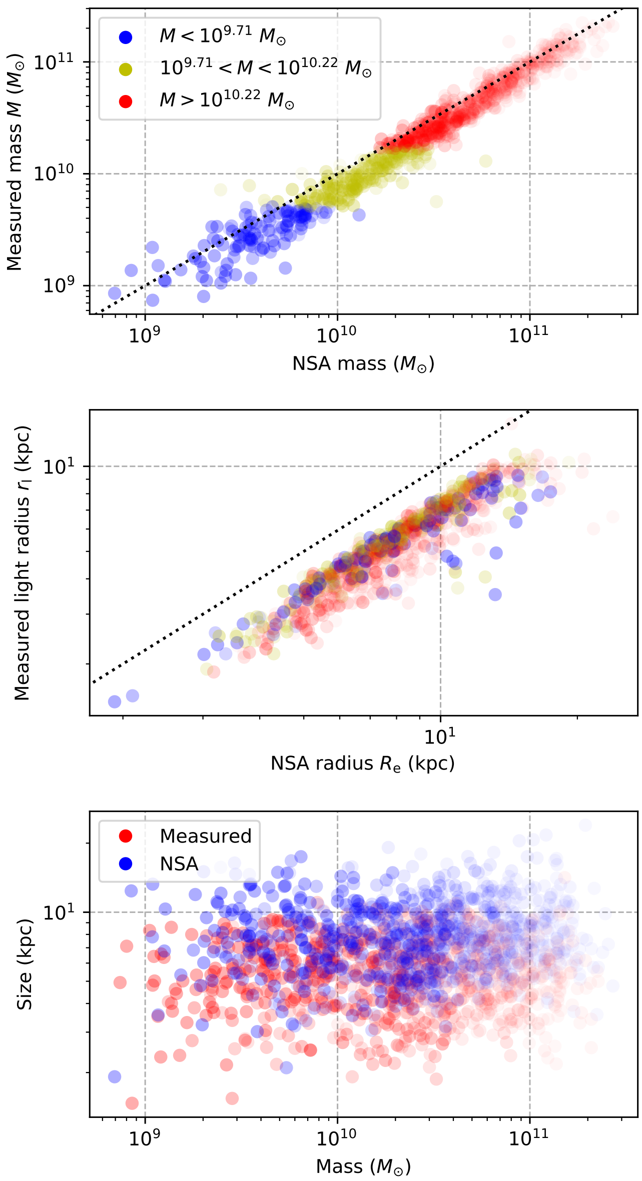

Figure 6.9: Comparison of the masses (*top*) and radii r_l (*middle*) of the spiral sample taken from the NASA-Sloan Atlas (Blanton et al., 2011) and measured by STARLIGHT within 1.2 R_e. The dashed lines indicate equality. Both measurements are consistent with the NSA values, with the offset in measured radius r_l attributable to the limitations of the MaNGA FOV. *Bottom*: We find no mass–size relation for the sample of spiral galaxies at the present day when using the STARLIGHT- or NSA-measured parameters (red and blue respectively). The transparency of the points indicate the relative Primary+ MaNGA sample weighting for each galaxy.

STARLIGHT-derived measurements of the galaxies' masses and sizes, we find no strong mass–size trend in the present day sample of spiral galaxies at all; a Spearman rank test results in a correlation p-value of only $p = 0.84$ for the measured data, and similar for the NSA values. This lack of a relation may indicate that the Galaxy Zoo classifications for low-mass galaxies may be slightly biased so that the smaller low-mass galaxies are less likely to be classified as spirals.

6.8.2 Evolution of the mass–half-light-radius plane

Having reassured ourselves that our mass and r_1 radius measurements are appropriate proxies for the photometric measurements in the present-day galaxies, we can now explore how the mass–size plane changes over time. The upper panels of the animation in Figure 6.10 shows the evolution of the mass-r_1 plane over the last $\approx$ 10 Gyr. Figure 6.11 also shows the distribution of galaxies in the mass–r_1 plane at four different redshifts. The measurements shown are using STARLIGHT's current mass measurements of each SSP template (see Section 5.4 for the distinction between current and initial mass weights). In reality, the mass loss of each population will have been gradual over the galaxy's evolution rather than instantaneous as this approach implies. However, as stated in Section 5.4, by instead adopting the initial mass — and therefore assume that no mass loss occurs at all — we find no significant change to these results. The "reality" would of course be between these two extremes. However, since the two cases reach near-identical results, we present here only the results for the current mass template weightings to avoid uncertainties in modelling time-dependent mass loss estimates separately for each SSP at each time-step.

Assuming an absence of significant systematic radial migration effects, we find that the growth in r_1 of these galaxies has only occurred over the last $\approx$ 3 Gyr, while the bulk

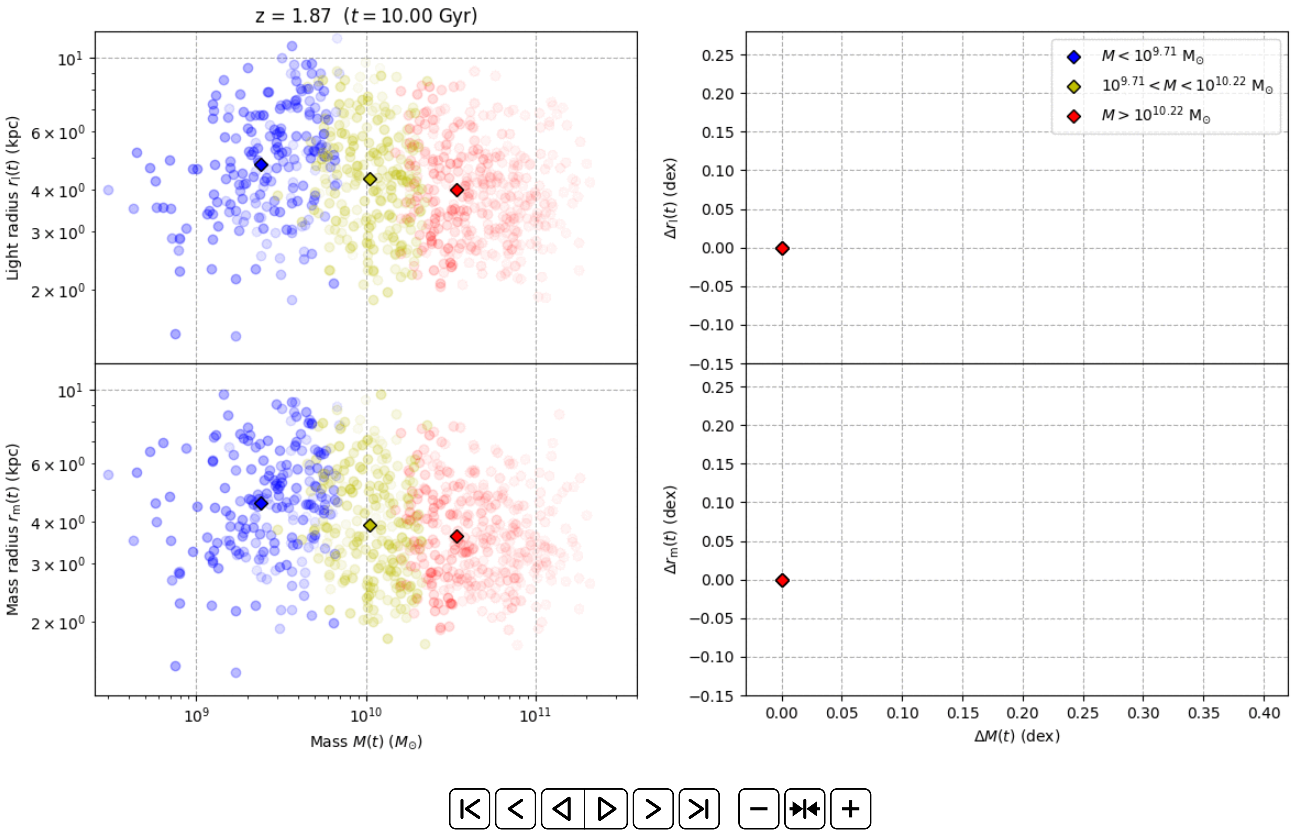

Figure 6.10: Evolution of the mass–size plane of the spiral sample over time. The lookback time and corresponding redshift are indicated at the top of the figure. The left column shows the mass–size plane for the light radius (r_l, *top*) and mass radius (r_m, *bottom*) measurements. The right column indicates the overall change in each galaxy's mass and size (in dex) from the first frame of the animation. The redshift of each galaxy is accounted for, such that in any given frame the star-formation histories of each galaxy is sampled at the difference between the frame age and the lookback time implied by the galaxy's redshift.

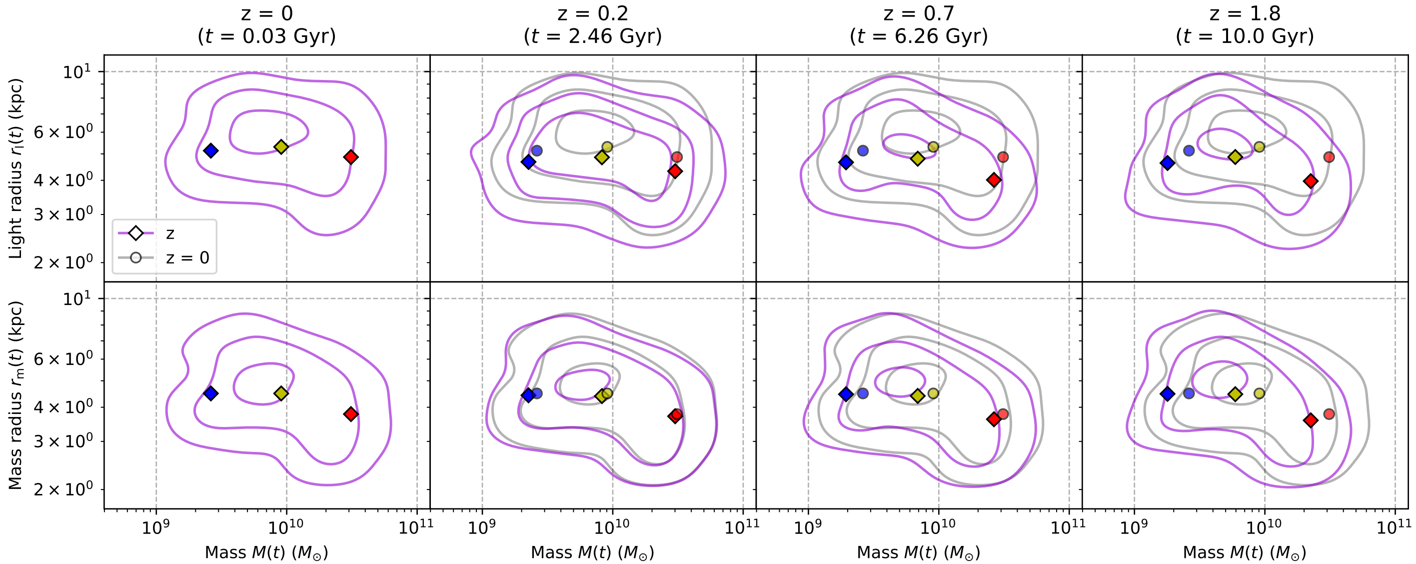

Figure 6.11: The distributions of galaxies at individual snapshots in Figure 6.10 showing the mass–r_l (*upper panels*) and mass–r_m (*lower panels*) planes at selected redshifts z. The corresponding lookback times t are also indicated. As fiducials, the grey contours and circle markers indicate the distribution of galaxies and the mean positions of each mass bin at z = 0, while the magenta contours and coloured diamond points indicate the distribution and mean positions at each redshift's time slice.

of the growth in mass occurred before this. We also find that galaxies generally have not changed their relative mass group, instead growing in mass and size at the same rates as those of similar masses and sizes. This cohort behaviour implies that, although every galaxy has had a unique formation history, tracing the average evolution of a galaxy population (e.g. by measuring galaxy properties at different redshifts) is representative of how most galaxies have evolved over the same time period.

6.8.2.1 Mass dependence

By splitting the galaxy into the subsamples of different mass bins as before, we find that over the last 10 Gyr, the low-mass galaxies have grown significantly more in mass (≈ 0.17 dex) but less in light radius r_l (≈ 0.05 dex) than the high-mass galaxies (≈ 0.14 dex growth in mass, ≈ 0.1 dex in r_l). We also find an effect of downsizing; the "turnup" time — at which galaxies stop growing significantly in mass and start growing in light radius r_l — occurred earlier in high-mass than low-mass galaxies (≈ 3.5 Gyr ago compared to ≈ 1 Gyr ago).

6.8.3 Evolution of the mass–half-mass-radius plane

While the light-weighted radius measurements are directly comparable to the size evolution of galaxy populations observed at different redshifts, the mass distribution of a galaxy is more fundamental to its build-up. In Figures 6.10 and 6.11, we therefore also show the evolution of the mass–size plane but using a half-*mass* size r_m (equivalently defined as the radius containing half of the stellar mass within 1.2 R_e due to the limitations of the MaNGA FOV) using the SSP template mass-to-light ratios. We find that despite increases in the observed light size r_l of the galaxy population, the corresponding increase in the mass size r_m of the same galaxies is minimal; we find an increase of

$\lessapprox$ 0.05 dex in size for almost all galaxies, even in those with low present-day stellar masses. This weak evolution is in agreement with the results presented by Suess et al. (2019a,b) using entirely independent approach to show that the half mass radius does not evolve significantly compared to the evolution of the half light radius.

The physical size growth of spiral galaxies over the last 10 Gyr has therefore been extremely small, at typically only 10% growth. Such an increase in mass radius — however slight — requires a radial increase in the regions of ongoing star formation. Since younger stellar populations dominate the light of a spiral galaxy at any time slice or lookback time, the increase in measured radius in observations of the same galaxies becomes significant. A small amount of star formation in the outskirts of the galaxies will contribute a large amount to the light while contributing comparatively little to the bulk of the galaxy, causing a strong mass-to-light gradient. Direct measurements of the growth of galaxies from observations therefore produce an overestimate of the underlying mass growth rate. This effect has also been recently quantified for cosmological galaxy catalogs from CANDELS (Suess et al., 2019a,b), who showed that the half-light radius growth of galaxies, both star-forming and quiescent, previously reported in many works is significantly weaker for the half-mass radius.

Interestingly, it has been reported by Frankel et al. (2019) that the structure of stellar populations seen in the Milky Way provide evidence for a slower growth in half-mass radius than in the half-light radius, and the evidence presented here — as well as from high-redshift surveys (see above) — suggests that this feature is common in the growth of spiral galaxies. This slow size growth of spiral galaxies seems to be in tension with predictions from semi-analytical models and hydrodynamics simulations of galaxy evolution in the context of the ΛCDM cosmology (see for a discussion Avila-Reese et al. 2018 and more references therein).

6.9 Potential limitations

6.9.1 Limitations of the data

Due to the limited FOV of the MaNGA observations, we are unable to measure a true half-light (or half-mass) radius for any given "time slice", since we do not have any background in the images. We are able to confirm in Figure 6.9 that the radius of half of the light (or mass) contained within 1.2 R_e is a good proxy for the present-day galaxy, but we have no way of confirming this at other stellar population ages. However, since we find that the oldest populations are most concentrated, the measured sizes in the earlier age-steps in the mass–size evolution are likely to be closer to the true sizes. The observed increase in size is therefore a conservative estimate of the real change. Since little of a galaxy's mass is located outside 1 R_e (e.g. Pérez et al. 2013), we expect that the mass radius r_m measurements are likely to be close to true half-mass radii.

6.9.2 Stellar population models and spectral fitting

Although we showed in Chapter 5 that STARLIGHT can measure stellar populations if the models used to do so are correct, this work assumes that the model spectrum templates of the E-MILES (Vazdekis et al., 2016) and Asa'd et al. (2017) libraries are representative of the true observed stellar populations. There are a number of unresolved problems in the field of stellar population modelling; see Conroy (2013) for a comprehensive review. For example, in Section 5.5, we described a correlation between weights assigned to populations $\gtrapprox 10^{9.5}$ years and those of $\lessapprox 10^{7.2}$ years due to a deficiency in the SSP templates. There is also uncertainty surrounding the shape of the IMF and ongoing debate on whether it varies between and within galaxies (La Barbera et al., 2013; Alton et al., 2017; Vaughan et al., 2018; Parikh et al., 2018). In principle, any variation of the

IMF over cosmic time is likely to affect our analysis too.

We also assume here that stellar metallicity is a one-dimensional parameter. In reality, the individual elemental abundances can vary from star to star. Further time-slicing work can be done to measure the simultaneous change in star-formation histories and metallacity evolution, including variation in α-enhanced metals, but this is beyond the scope of this project. Although we are confident that the fitting methods used here can break the age-metallicity degeneracy, the degeneracy between metallicity and [α/Fe] is harder to assess. However, we showed in Section 4.3.1.1 that removing the extra metallicity dimension appears to have little effect on the derived star-formation history.

This work has also assumed a single Calzetti et al. (2000) exinction model which affects every stellar population contained within a single spectrum equally. As we discussed in Section 5.4.1, we expect that younger stellar populations are instead likely to be affected by a greater amount of extinction, but we are unable to resolve this difference in non-parametric fitting using Starlight. How this deficiency affects the measured star-formation histories is not known.

Notwithstanding these shortcomings and assumptions used in the fitting process, the resulting star-formation histories tell a consistent story of inside-out formation in spiral galaxies with no noticeable artifacts, and the coherent structures visible in the time-slicing of galaxy 8329-12701 shown in Figure 6.1 gives confidence in the fitting method for the purposes described here. The clear inside-out formation reported here might even be underestimated: Ibarra-Medel et al. (2019) have recently shown that any intrinsic signature of inside-out growth is diminished by the instrumental/observational setting and the stellar population modelling, mainly the age resolution of the SSP templates.

6.9.3 Effects of radial mixing and mergers

Time-slicing methods can only reveal the current locations of different stellar populations in a galaxy. In this work, we have interpreted these present-day distributions to be indicative of the radial distributions of star formation at the age of the stellar population, and make no attempt to correct for the effects of radial migration or mergers. Fortunately, simulations suggest that the radial distributions of stellar populations in a galactic disk are not significantly altered by radial migration (Avila-Reese et al., 2018; Navarro et al., 2018; Barros et al., 2020), indicating that the assumptions made here are at least approximately valid.

High-resolution simulations of Milky Way-like galaxies show that radial migration has no preferential direction, with most stars being scattered similarly inwards and outwards, by typically no more than 1–2 kpc (Avila-Reese et al., 2018). Instead, stars are equally likely to move in either direction over their lives (Sellwood & Binney, 2002; Avila-Reese et al., 2018), with observations implying that any resulting observed growth as a result of migration occurs slower than the intrinsic growth of the disk (Martínez-Lombilla et al., 2019). Any radial migration of an initially centrally-concentrated distribution of stars is likely to become slightly less concentrated over time, an effect which is observed in the stellar metallicity distributions of the solar neighbourhood in the Milky Way (e.g. Feltzing et al. 2019; Frankel et al. 2018). A galaxy with a radial distribution of star formation that is not varying over time would be observed using time-slicing methods to have been slightly decreasing in measured radius over the same time frame, since the oldest populations will have more time to disperse and would therefore appear at larger radii. The measured variations of spatial distribution of stellar populations of different ages in Section 6.7 are also therefore likely to be a close lower limit on the true variation of the sizes of spiral galaxies over the same time period. Similarly, the recovered change in light size r_l in Section 6.8 is therefore a slightly conservative but representative estimate of how the galaxy evolved over the same time period.

6.10 Conclusions

We have derived spatially-resolved star formation histories for a sample of 795 low-redshift spiral galaxies using STARLIGHT applied to integral-field spectroscopic observations from SDSS-IV MaNGA. From this fossil record analysis, we have built maps indicating the regions in which stellar populations of different ages are located in any given galaxy. We analysed the radial profiles of these "time slices" to extract the historical growth of the population of spiral galaxies. The main findings are:

- We have quantified evidence for inside-out galaxy growth in three different ways, which all indicate that such a growth mode is dominant in the majority of spiral galaxies, and is most significant in high-mass galaxies:
  - The mass-weighted mean age gradient of spiral galaxies tends to be slightly negative; the outskirts are younger than the centres in $\approx 60\%$ of all spiral galaxies. This fraction rises to 80% for galaxies with stellar mass $M > 10^{10.22} M_{\odot}$.
  - By measuring a time T_{95} by which 95% of the stellar mass had built up in each location of the galaxy, we find that T_{95} decreases with radius in the majority galaxies. Gradients in T_{95} are steepest in the highest-mass galaxies.
  - The concentration c of each "time slice" was found for each galaxy. The youngest stellar populations (younger than $\approx 10^{8.5}$ years) are more radially extended than the oldest ($\approx 10^{10}$ years old) populations in all cases, and this effect is most significant in high-mass galaxies.

- By considering the simultaneous increase in stellar mass and the increase in light radius with the addition of ever-younger stellar populations, we found that the mass–size distribution of spiral galaxies evolves with very little change in rank; galaxies grow in mass and size at similar rates to other galaxies with similar masses and sizes. This suggests that a "like for like" approach when comparing the sizes and masses of galaxy distributions at different redshifts is representative of how the individual galaxies themselves have evolved.

- We found that over the last 10 Gyr, galaxies with high present-day stellar masses have grown their half-light size by approximately twice the amount that low-mass galaxies have, although low-mass galaxies have grown slightly more in mass.

- However, when the half-mass radius of the galaxies was used instead, we found that spiral galaxies have barely altered their radial mass distributions over the same time period. Although galaxies appear to grow in (light) size over cosmic time, we show that this is an overestimate of their actual physical growth. This apparent discrepancy is due to a small amount of star formation occurring in the outskirts being able to dominate a galaxy's light while contributing very little to the physical bulk of the galaxy.

Chapter 7

Conclusions and Future Work

The evolution of spiral galaxies and the nature of their structural components still contain unanswered questions despite decades of research. However, modern integral-field spectroscopic galaxy surveys and spectral fitting codes offer exciting new tools to address these questions. This thesis developed an approach of deriving star-formation histories and then building maps of stellar populations of different ages to measure how a galaxy's structural parameters vary with stellar age. As we illustrated in Figures 4.2 and 6.1, such variation in a spiral galaxy's structure can be significant. This thesis demonstrated how the measurement of the spatial variation in star-formation history across spiral galaxies in this manner can help to understand issues as varied as the nature of non-axisymmetric structures such as bars and spiral arms, and the growth of spiral galaxies over the last 10 Gyr.

Possible future expansion of this work includes applying fossil record analysis to a larger sample to reveal how well current models can describe the bar and spiral structure in a population of spiral galaxies, or applying these methods to answer other open questions in galaxy structure and evolution.

7.1 Conclusions

We applied stellar population fitting methods to spiral galaxies in the SDSS-MaNGA sample, primarily using Starlight. Through analysis of the raw outputs from the spectral fitting methods, we showed in Chapter 5 that such results require careful interpretation due to the lack of hot old stars in the stellar population models, but that the derived star-formation histories are likely to be reliable over most of the possible range of stellar population ages despite this shortcoming. By creating test spectra with known distributions in stellar population age, we also found that Starlight is able to both determine the age of a single stellar population and recover a full star-formation history to a reasonable accuracy, even in spectra with signal-to-noise ratios as low as 5 – 10, providing reassurance as to the reliability of these techniques.

7.1.1 The nature of non-axisymmetric structures

Chapters 3 and 4 highlight how there is a large amount of information contained within the azimuthal variations of a spiral galaxy's star-formation history that is missed by studying only the radial variation. We showed that by preserving the full spatial information available with integral-field spectroscopy, we can study the nature and structure of spiral arms and bars.

7.1.1.1 Spiral arms

In Chapter 3, we presented a new direct test of the quasi-stationary density wave theory, and applied it to UGC 3825, a grand-design spiral galaxy. This technique relies on identifying spiral structure exhibited in two different tracers between which there is a characteristic time delay. Through a spectral fitting approach, we derived a map of the location of young ($\leq$ 60 Myr) stars, and compared this with a map of Hα emission which is indicative of ongoing star-formation. The existence of an azimuthal offset between these two tracers lends support to hypothesis that the spiral arms in UGC 3825 are created by a density wave.

We then showed that it is possible to measure the radial dependence of the spiral pattern speed by cross-correlating the two spiral arm tracers. We found that the pattern speed in UGC 3825 is consistent with being constant with radius, providing direct evidence for the density wave spiral arms being quasi-stationary in nature. We also found remarkably consistent results using spiral structure traced by an older (0.2 – 1.3 Gyr) stellar population, supporting the reliability of this new method.

From a "time slicing" analysis of the barred spiral galaxy MCG+07-28-064, in Chapter 4 we also showed that it is possible to measure how the spiral arm contrast of a spiral galaxy varies with stellar population age. These measurements were among the first to make use of the spiral arm masks created as part of the Galaxy Zoo:3D citizen science project. We found that the spiral contrast is greatest in the youngest stellar populations — as expected, since spiral arms are sites of enhanced star formation — but that a contrast was still measurable in stars as old as 2 Gyr. This result provides further evidence for a density wave model of spiral structure being present in this two-armed spiral galaxy.

7.1.1.2 Bars

In Chapter 4, we also measured how the structural parameters of the bar vary with stellar population age in MCG+07-28-064, and demonstrated how this approach can reveal interesting properties of the bar's dynamics and history. For example, we found that the bar's length is greatest when traced by the youngest stars. Since a bar is associated with stable disk-related orbits, this variation of bar length with stellar population age is circumstantial evidence for inside-out growth of the galaxy's disk.

We also found that the bar in MCG+07-28-064 varies in position angle. Specifically, we showed that the bar traced by stellar populations younger than 0.1 Gyr is angled 15° ahead of the bar traced by older populations. Since we found the spatial distribution of these young stars to be consistent with the morphology of the Hα emission line, we attributed this angular offset as star-formation occurring on the leading edge of the bar.

7.1.2 The growth of spiral galaxies

Finally, in Chapter 6, we investigated what the radial variation of star-formation histories in a sample of $\sim$ 800 galaxies can reveal about how spiral galaxies have grown. Consistent with previous stellar population studies, we found that most spiral galaxies exhibit negative gradients in their mean stellar age (indicating that the central regions of a galaxy are on average older than the outskirts), and that this gradient is most significant in high-mass galaxies.

We then defined a T_{95} parameter, which measures the lookback time by which 95% of the current stellar mass contained within a spectrum had been formed in the stellar population fits. We found that T_{95} decreases with radius (i.e. as above, the inner regions formed earliest) and that the radial gradient of T_{95} is strongest in galaxies with high present-day stellar mass.

We also used the full age distribution available from a "time slicing" approach to measure the relative spatial extent of stars of different ages. Specifically, we defined a measurement of concentration c, which confirmed that the youngest stellar populations are most extended and the oldest populations are most centrally-concentrated in spiral galaxies. This difference was found to be most extreme in the highest-mass galaxies.

Together, these analyses provide strong evidence for an inside-out growth mode being dominant in all spiral galaxies, and also that this formation scenario is most significant in high-mass galaxies. However, by making full use of the radial information available with integral field spectroscopy, we showed that it is possible to go further and reconstruct the evolution of each individual galaxy in the mass–size plane. These measurements rely on radial migration not having significantly altered a galaxy's stellar population structure, an assumption which is supported by recent simulations.

We found that each individual galaxy has evolved in the mass–size plane in similar ways, with no change in rank (i.e. galaxies do not mix within the distribution, and instead move in similar ways to each other). This result supports the cosmological approach of determining how the average distribution of the galaxy population at different redshifts varies in the mass–size plane as a robust way to measure how galaxies themselves evolve. We also showed that high-mass galaxies have grown more in light-radius than their low-mass counterparts have over the last $\sim$ 10 Gyr. By contrast, we saw that the relative stellar mass growth in low-mass galaxies over the same time period has been greater than that of high-mass galaxies.

However, by measuring the growth of galaxies' stellar mass-radius, we found that the underlying physical size of a spiral galaxy has not significantly changed over the last 10 Gyr. We concluded that a fossil record analysis of a large sample of galaxies shows that the growth of disks in spiral galaxies does occur inside-out, but that this expansion is in large part due to a relatively small amount of bright star formation in the outskirts of galaxies which does not significantly contribute to the physical bulk of the galaxy.

7.2 Future work

The work in this thesis concerned the development of new approaches to measuring and interpreting galaxy structure using integral-field spectroscopic galaxy surveys. We have demonstrated that such approaches are reliable, and that they can be used to uncover a large amount of information about a galaxy's structural components. There are many potential further applications of the methods outlined in this thesis.

7.2.1 Directly extending this thesis' work

The work in this thesis studied the dynamics and history of a galaxy through a fossil record approach. We showed that these methods work, and that they reveal more about a spiral galaxy than simple radial age gradients. It would therefore be straightforward to apply these methods to other galaxy samples to reveal how the structure of stellar populations in spiral galaxies varies with other galaxy properties.

7.2.1.1 Understanding spiral and bar structures in a population of galaxies

In this thesis, we showed that it is possible to study the properties of the bar and the nature of spiral arms using a fossil record approach, but did not extend this work to more than a single example galaxy in either case.

By applying the method of measuring the spiral pattern speed developed in Chapter 3 to a sample of galaxies, it may be possible to reveal how many spiral galaxies can be explained by a quasi-stationary density wave model. Furthermore, Dobbs & Pringle (2010) predict that the precise distributions of stellar populations around a spiral arm are intrinsically linked to the excitation mechanism responsible for producing spiral structure (see Figure 7.1). The time-slicing methods described in this thesis could in

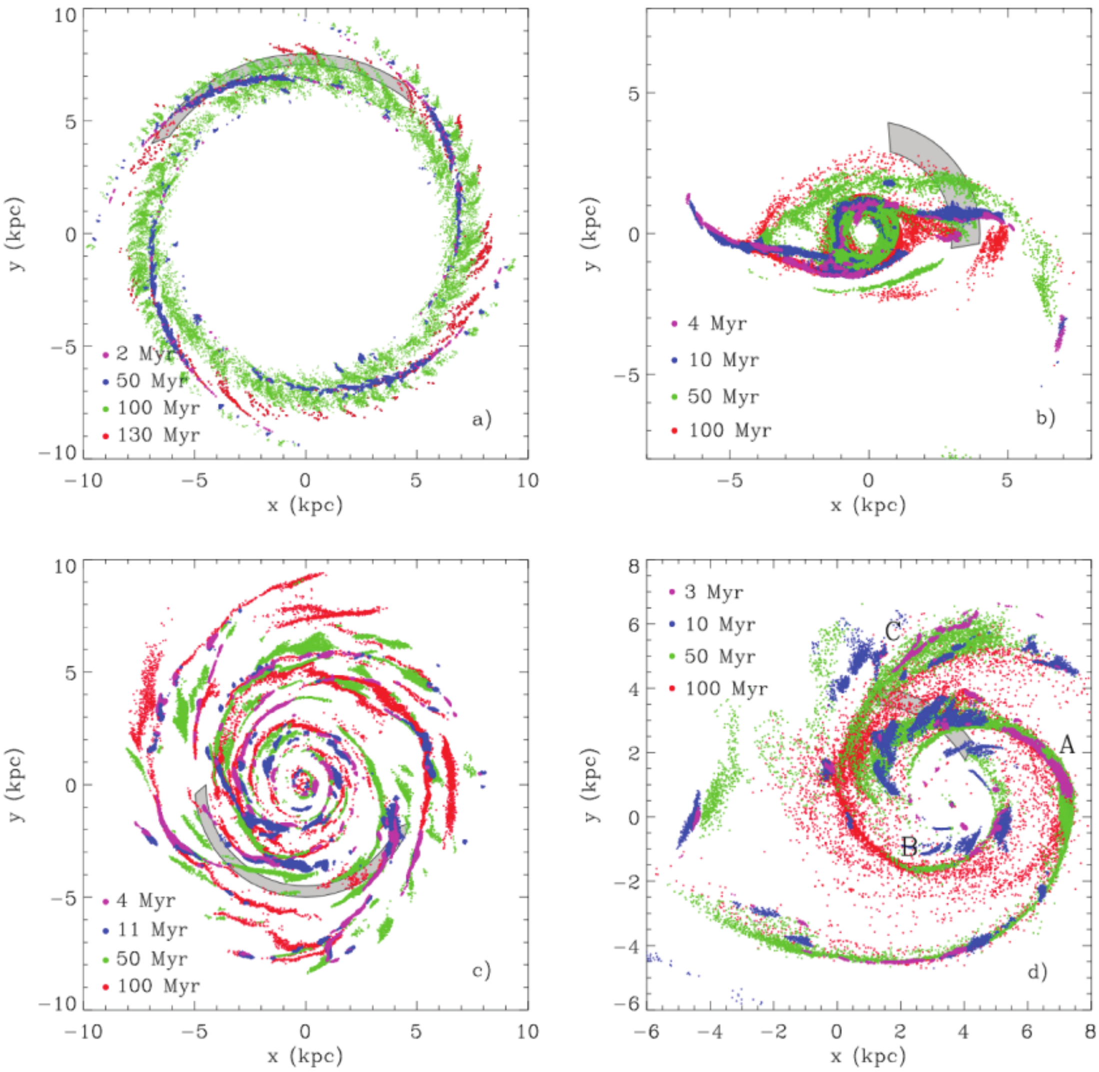

Figure 7.1: Simulations by Dobbs & Pringle (2010) predict different distributions of stellar populations around spiral arms depending on the spiral structure mechanism. Spirals with a fixed pattern speed *top left*, flocculent structure *bottom left*, or structure excited by bars *top right* or tidal interactions *lower right* show different stellar age distributions, denoted by the different colours. Figure taken from Dobbs & Pringle (2010)

principle be used to verify those predictions for barred and flocculent galaxies. Similarly, in Chapter 4, we showed that an enhancement in stellar flux density is observed in stars as old as 2 Gyr, which we argued is indicative of an underlying density wave. Since Galaxy Zoo:3D spiral arm masks are available for $\sim$ 300 spiral galaxies at the time of writing, this effect could be sought in a population of spiral galaxies. Using these methods, it would therefore be possible to confirm whether different spiral mechanisms are indeed responsible for the different spiral types described in Section 1.3.

In Chapter 4, we also revealed the changing morphology of a bar when viewed in stellar populations of different ages. Fraser-McKelvie et al. (2020) have investigated the morphology of Hα emission in bars in a large sample of galaxies, and found that the galaxy's stellar mass is a strong determinant of whether star-formation occurs within, at the end of, or surrounding the bar. Further work could link the stellar population morphologies to these trends.

7.2.1.2 The formation and quenching of lenticular galaxies

Although this thesis has exclusively focused on applications to spiral galaxies due to their extended star-formation histories making them ideal candidates for fossil record studies, further work could determine whether the inside-out growth trends seen in spiral galaxies in Chapter 6 are also seen in lenticular galaxies. If so, this similarity would be evidence for the hypothesis that the S0 morphology is a "faded spiral", rather than an entirely different class of galaxy. Caution in measuring spatial differences in star-formation histories at large lookback times would be required, however, since fossil record analyses are less sensitive to populations older than ~5–8 Gyr.

7.2.1.3 Metallicity evolution

The STARLIGHT outputs include the full distribution of best-fit weights in age–metallicity space, but this thesis has only made use of the stellar ages. Figures 4.2 and 6.1 showed that the mean stellar metallicity of a spiral galaxy varies with stellar age. It would be straightforward to investigate what drives this trend, and whether large changes in metallicity are coincident with a peak in the star-formation history, which might be indicative of infalling pristine gas driving new star formation.

7.2.1.4 IC 342

An ancillary programme of MaNGA is obtaining IFS observations across the face of IC 342, which is an extremely nearby ($\sim$ 3 Mpc; Saha et al. 2002) low-inclination ($i = 31°$; Crosthwaite et al. 2000) massive spiral galaxy. Instead of a single IFU being used to observe a single galaxy, IC 342 requires tiling using several individual observations. This will result in a spatial resolution of $\sim$ 32 pc, compared to $\sim$ kpc scales for the main MaNGA samples. These observations are still ongoing, but with such a high spatial resolution on completion, a study of the stellar populations near the spiral arms could produce high-quality pattern speed measurements using the method described in Chapter 3. It would also be possible to perform the same spectral fitting methods described in Chapters 5 and 6 to the full "megacube" of IC 342 to investigate its disk growth in greater resolution than in this thesis.

7.2.1.5 Using MUSE

Similarly, the methods developed here could be transferred to applications with other IFUs. For example, the state of the art multi-unit spectroscopic explorer (MUSE; Bacon et al. 2010) at the VLT has a similar spectral resolution but superior spatial resolution

($\sim$ 0.04 arcsec compared to $\sim$ 2 arcsec) to MaNGA, making it ideal to use the methods described here to probe smaller spatial scales. However, at 4650–9300 Å, MUSE's wavelength range is more limited than MaNGA's — and therefore cannot measure the Balmer absorption series in galaxies nearer than $z \lessapprox 0.25$ — and as only a single integral-field unit, sample sizes are limited. By obtaining detailed observations of a handful of galaxies, MUSE has already been used to study the role of spiral structure at low redshift in regulating star formation (Kreckel et al., 2016) and affecting local gas metallicity (Sánchez-Menguiano et al., 2016; Vogt et al., 2017), for example.

7.2.2 Cosmic star-formation histories

Applying fossil record methods to single-fibre spectra, Panter et al. (2003, 2007) derived the star-formation and metallicity histories of the Universe. However, Kewley et al. (2005) showed that since single-fibre spectroscopy probes different physical diameters of galaxies of different redshifts, such results may be inaccurate. As a result, there has been some work to use observations from integral-field spectroscopic galaxy surveys to perform spectral fitting out to a larger consistent radius (e.g. López Fernández et al. 2018; Sánchez et al. 2019). These have shown consistency with observations of galaxy populations at different redshifts, but Sánchez et al. (2019) find a peak in total star-formation at $z \sim 1$, slightly later than the $z = 1.5 - 2.5$ found by cosmological studies (e.g. Madau et al. 1998; Madau & Dickinson 2014; Driver et al. 2018). However, this measurement is probing large lookback times of up to 10^{10} years, where fossil record analyses are less sensitive.

As a preliminary test for how the fossil record analysis described in this thesis can be used to derive the star-formation history of the Universe, all galaxies in the Primary+ and Secondary MaNGA samples of MPL-8 have been fitted using the method

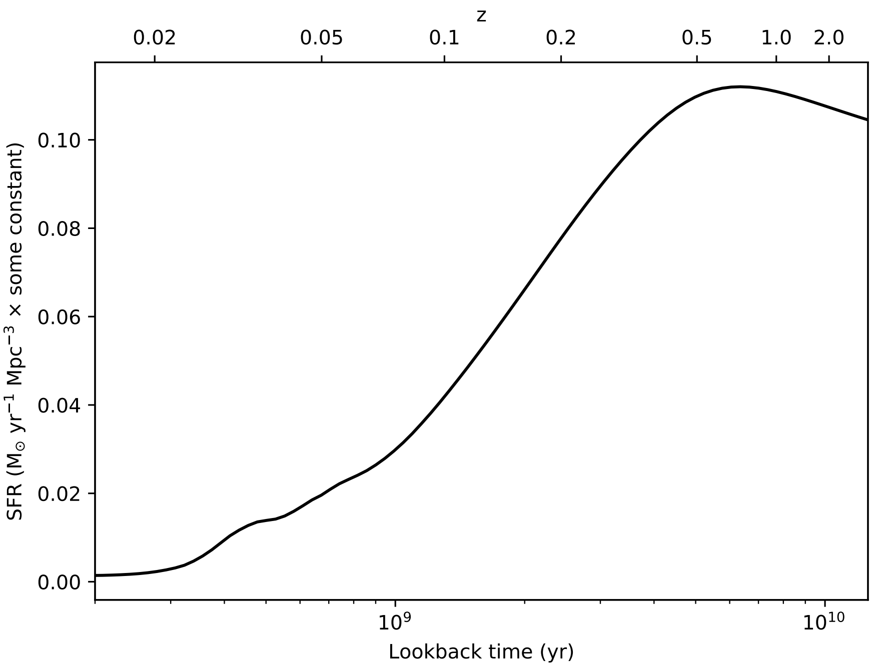

Figure 7.2: The star-formation history of the Universe revealed by fossil record analysis of all galaxies in MPL-8, showing a peak at $z \sim 0.5 - 1$. This is a preliminary result.

described in Chapter 5. To avoid the blurring effects of mixing spectra of galaxies at different relative velocities, all emission-subtracted spaxel spectra of each galaxy were rebinned onto a single rest-frame wavelength base using the MaNGA DAP's stellar velocity measurements, before summing all spaxels within 1.5 R_e. After accounting for the MaNGA sample weighting and for the different observed redshifts of each galaxy, a preliminary cosmic star-formation history is shown in Figure 7.2. Even in this initial test, the measured peak in star-formation history at $z = 0.5 - 1$ is reassuringly approximately consistent with that measured by Sánchez et al. (2019).

In Chapter 6, we demonstrated how a fossil record analysis of the mass–size plane can simultaneously reveal the evolution in the average distributions as well as the growth of individual galaxies within the population. Through a similar approach, Sánchez et al. (2019) also derived the evolution of the galaxy SFR–mass "main sequence", and showed that currently quiescent galaxies dominated the Universe's star-formation in earlier

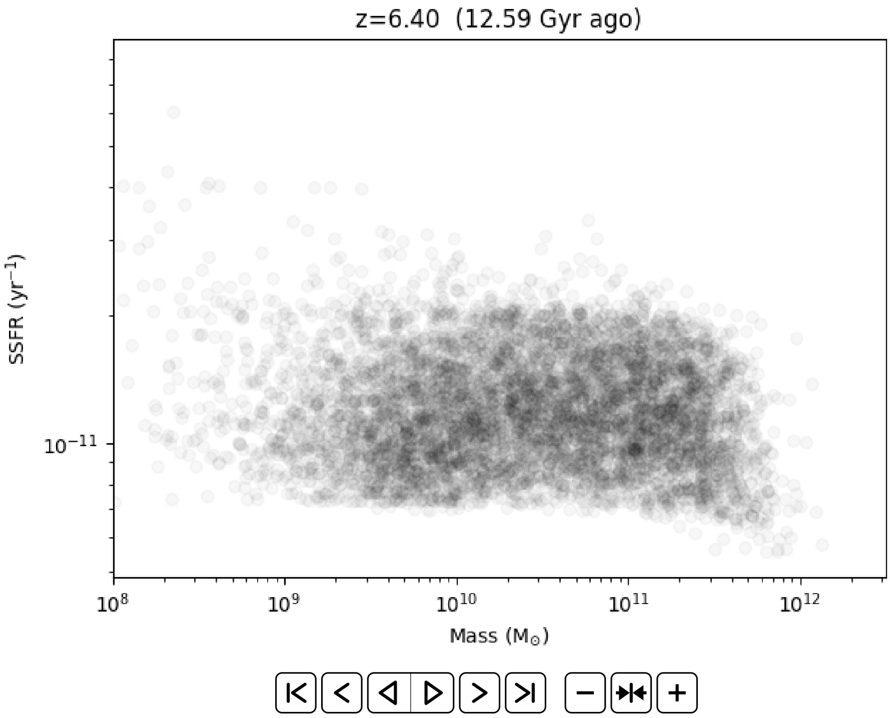

Figure 7.3: Animation showing the evolution of the specific star-formation rate–stellar mass plane. High-mass galaxies appear to shut down their star-formation earlier than low-mass galaxies. This is a preliminary result.

times. An animation of the evolution of MPL-8 galaxies in the specific star-formation rate–stellar mass plane is shown in Figure 7.3. Although this result is very preliminary work, some features are seen which are consistent with the current understanding of the evolution of star-formation rates in galaxies. For example, more massive galaxies appear to become quiescent more rapidly than low-mass galaxies. Further work could readily be done to determine exactly what role a galaxy's stellar mass and present-day morphology have had on its contribution to the Universe's star-formation history or on its evolution in the SFR–mass plane.

Even these preliminary results highlight how powerful and versatile the fossil record analyses developed in this thesis can be in studying the evolution of the Universe, as well as its constituent galaxies and their structural components.

Bibliography

Abazajian K.N., Adelman-McCarthy J.K., Agüeros M.A. et al., 2009. *The Seventh Data Release of the Sloan Digital Sky Survey*. ApJS, 182, 2, 543–558.

Abdeen S., Kennefick D., Kennefick J. et al., 2020. *Determining the Co-Rotation Radii of Spiral Galaxies Using Spiral Arm Pitch Angle Measurements at Multiple Wavelengths*. arXiv e-prints, arXiv:2002.02307.

Aguado D.S., Ahumada R., Almeida A. et al., 2019. *The Fifteenth Data Release of the Sloan Digital Sky Surveys: First Release of MaNGA-derived Quantities, Data Visualization Tools, and Stellar Library*. ApJS, 240, 2, 23.

Aguerri J.A.L., Méndez-Abreu J. & Corsini E.M., 2009. *The population of barred galaxies in the local universe. I. Detection and characterisation of bars*. A&A, 495, 2, 491–504.

Aguerri J.A.L., Méndez-Abreu J., Falcón-Barroso J. et al., 2015. *Bar pattern speeds in CALIFA galaxies. I. Fast bars across the Hubble sequence*. A&A, 576, A102.

Alton P.D., Smith R.J. & Lucey J.R., 2017. *KINETyS: constraining spatial variations of the stellar initial mass function in early-type galaxies*. MNRAS, 468, 2, 1594–1615.

Anders F., Khalatyan A., Chiappini C. et al., 2019. *Photo-astrometric distances, extinctions, and astrophysical parameters for Gaia DR2 stars brighter than G = 18*. A&A, 628, A94.

Andersen D.R. & Bershady M.A., 2013. *The Photometric and Kinematic Structure of Face-on Disk Galaxies. III. Kinematic Inclinations from Hα Velocity Fields*. ApJ, 768, 1, 41.

Aramyan L.S., Hakobyan A.A., Petrosian A.R. et al., 2017. *The Distribution of Supernovae Relative to Spiral Arms of Host Disc Galaxies*. volume 511 of *Astronomical Society of the Pacific Conference Series*, page 180.

Argudo-Fernández M., Verley S., Bergond G. et al., 2015. *Catalogues of isolated galaxies, isolated pairs, and isolated triplets in the local Universe*. A&A, 578, A110.

Arribas S., Carter D., Cavaller L. et al., 1998a. *INTEGRAL: a matrix optical fiber system for WYFFOS*. volume 3355 of *Society of Photo-Optical Instrumentation Engineers (SPIE) Conference Series*, pages 821–827.

Arribas S., del Burgo C., Carter D. et al., 1998b. *INTEGRAL: an Optical-Fiber System for 2-D Spectroscopy on the 4.2-in William Herschel Telescope*. volume 152 of *Astronomical Society of the Pacific Conference Series*, page 149.

Asa'd R.S., Vazdekis A., Cerviño M. et al., 2017. *Young LMC clusters: the role of red supergiants and multiple stellar populations in their integrated light and CMDs*. MNRAS, 471, 3, 3599–3614.

Asari N.V., Cid Fernandes R., Stasińska G. et al., 2007. *The history of star-forming galaxies in the Sloan Digital Sky Survey*. MNRAS, 381, 263–279.

Athanassoula E., 1992. *Morphology of bar orbits*. MNRAS, 259, 328–344.

Avila-Reese V., González-Samaniego A., Colín P. et al., 2018. *The Global and Radial Stellar Mass Assembly of Milky Way-sized Galaxies*. ApJ, 854, 2, 152.

Baba J., Morokuma-Matsui K. & Egusa F., 2015. *Radial distributions of arm-gas offsets as an observational test of spiral theories*. PASJ, 67, L4.

Bacon R., Adam G., Baranne A. et al., 1988. *The Integral Field Spectrograph TIGER*. volume 30 of *European Southern Observatory Conference and Workshop Proceedings*, page 1185.

Bacon R., Adam G., Baranne A. et al., 1995. *3D spectrography at high spatial resolution. I. Concept and realization of the integral field spectrograph TIGER.* A&AS, 113, 347.

Bacon R., Copin Y., Monnet G. et al., 2001. *The SAURON project - I. The panoramic integral-field spectrograph*. MNRAS, 326, 23–35.

Bacon R., Accardo M., Adjali L. et al., 2010. *The MUSE second-generation VLT instrument*. volume 7735 of *Society of Photo-Optical Instrumentation Engineers (SPIE) Conference Series*, page 773508.

Baldry I.K., Glazebrook K., Brinkmann J. et al., 2004. *Quantifying the Bimodal Color-Magnitude Distribution of Galaxies*. ApJ, 600, 681–694.

Barden S.C. & Wade R.A., 1988. *DensePak and spectral imaging with fiber optics.* volume 3 of *Astronomical Society of the Pacific Conference Series*, pages 113–124.

Barrera-Ballesteros J.K., Falcón-Barroso J., García-Lorenzo B. et al., 2014. *Kinematic alignment of non-interacting CALIFA galaxies. Quantifying the impact of bars on stellar and ionised gas velocity field orientations*. A&A, 568, A70.

Barros D.A., Pérez-Villegas A., Lépine J.R.D. et al., 2020. *Exploring the Origin of Moving Groups and Diagonal Ridges by Simulations of Stellar Orbits and Birthplaces*. ApJ, 888, 2, 75.

Beckman J.E., Font J., Borlaff A. et al., 2018. *Precision Determination of Corotation Radii in Galaxy Disks: Tremaine-Weinberg versus Font-Beckman for NGC 3433*. ApJ, 854, 182.

Behroozi P., Wechsler R.H., Hearin A.P. et al., 2019. *UNIVERSEMACHINE: The correlation between galaxy growth and dark matter halo assembly from z = 0-10*. MNRAS, 488, 3, 3143–3194.

Belfiore F., Westfall K.B., Schaefer A. et al., 2019. *The Data Analysis Pipeline for the SDSS-IV MaNGA IFU Galaxy Survey: Emission-Line Modeling*. arXiv e-prints.

Berman S.L., 2003. *Simulations of dual morphology in spiral galaxies*. A&A, 412, 387–398.

Bertelli G., Bressan A., Chiosi C. et al., 1994. *Theoretical isochrones from models with new radiative opacities*. A&AS, 106, 275–302.

Bertin G., Lin C.C., Lowe S.A. et al., 1989. *Modal Approach to the Morphology of Spiral Galaxies. I. Basic Structure and Astrophysical Viability*. ApJ, 338, 78.

Bertin G. & Lin C.C., 1996. *Spiral structure in galaxies: A density wave theory*. The MIT Press.

Bertin G., 2014. *Dynamics of Galaxies*. Cambridge University Press.

Binney J., 1977. *The physics of dissipational galaxy formation.* ApJ, 215, 483–491.

Bittner A., Gadotti D.A., Elmegreen B.G. et al., 2017. *How do spiral arm contrasts relate to bars, disc breaks and other fundamental galaxy properties?* MNRAS, 471, 1, 1070–1087.

Bittner A., Falcón-Barroso J., Nedelchev B. et al., 2019. *The GIST pipeline: A multi-purpose tool for the analysis and visualisation of (integral-field) spectroscopic data*. A&A, 628, A117.

Blanton M.R. & Moustakas J., 2009. *Physical Properties and Environments of Nearby Galaxies*. ARA&A, 47, 1, 159–210.

Blanton M.R., Kazin E., Muna D. et al., 2011. *Improved Background Subtraction for the Sloan Digital Sky Survey Images*. AJ, 142, 31.

Blanton M.R., Bershady M.A., Abolfathi B. et al., 2017. *Sloan Digital Sky Survey IV: Mapping the Milky Way, Nearby Galaxies, and the Distant Universe*. AJ, 154, 28.

Blitz L. & Spergel D.N., 1991. *Direct Evidence for a Bar at the Galactic Center*. ApJ, 379, 631.

Block D.L., Buta R., Knapen J.H. et al., 2004. *Gravitational Bar and Spiral Arm Torques from K_s-band Observations and Implications for the Pattern Speeds*. AJ, 128, 1, 183–201.

Boardman N., Zasowski G., Seth A. et al., 2020. *Milky Way analogues in MaNGA: multiparameter homogeneity and comparison to the Milky Way*. MNRAS, 491, 3, 3672–3701.

Boquien M., Burgarella D., Roehlly Y. et al., 2019. *CIGALE: a python Code Investigating GALaxy Emission*. A&A, 622, A103.

Bovy J., Rix H.W. & Hogg D.W., 2012. *The Milky Way Has No Distinct Thick Disk*. ApJ, 751, 2, 131.

Bovy J., Rix H.W., Schlafly E.F. et al., 2016. *The Stellar Population Structure of the Galactic Disk*. ApJ, 823, 1, 30.

Breda I. & Papaderos P., 2018. *The continuous rise of bulges out of galactic disks*. A&A, 614, A48.

Bruzual G., 1983. *Spectral evolution of galaxies. I. Early-type systems.* ApJ, 273, 105–127.

Bruzual G. & Charlot S., 2003. *Stellar population synthesis at the resolution of 2003*. MNRAS, 344, 1000–1028.

Bundy K., Bershady M.A., Law D.R. et al., 2015. *Overview of the SDSS-IV MaNGA Survey: Mapping nearby Galaxies at Apache Point Observatory*. ApJ, 798, 7.

Burstein D., 1979. *Structure and origin of S0 galaxies. III. The luminosity distribution perpendicular to the plane of the disks in S0's.* ApJ, 234, 829–836.

Buta R.J., Corwin H.G. & Odewahn S.C., 2007. *The de Vaucouleurs Atlas of Galaxies*. Cambridge University Press.

Calzetti D., Armus L., Bohlin R.C. et al., 2000. *The Dust Content and Opacity of Actively Star-forming Galaxies*. ApJ, 533, 682–695.

Calzetti D., 2001. *The Dust Opacity of Star-forming Galaxies*. PASP, 113, 1449–1485.

Calzetti D., Kennicutt Jr. R.C., Bianchi L. et al., 2005. *Star Formation in NGC 5194 (M51a): The Panchromatic View from GALEX to Spitzer*. ApJ, 633, 871–893.

Cappellari M. & Emsellem E., 2004. *Parametric Recovery of Line-of-Sight Velocity Distributions from Absorption-Line Spectra of Galaxies via Penalized Likelihood*. PASP, 116, 138–147.

Cappellari M., Emsellem E., Krajnović D. et al., 2011a. *The ATLAS^{3D} project - I. A volume-limited sample of 260 nearby early-type galaxies: science goals and selection criteria*. MNRAS, 413, 813–836.

Cappellari M., Emsellem E., Krajnović D. et al., 2011b. *The ATLAS^{3D} project - VII. A new look at the morphology of nearby galaxies: the kinematic morphology-density relation*. MNRAS, 416, 3, 1680–1696.

Cappellari M., 2017. *Improving the full spectrum fitting method: accurate convolution with Gauss-Hermite functions*. MNRAS, 466, 798–811.

Cardelli J.A., Clayton G.C. & Mathis J.S., 1989. *The relationship between infrared, optical, and ultraviolet extinction*. ApJ, 345, 245–256.

Carnall A.C., McLure R.J., Dunlop J.S. et al., 2018. *Inferring the star formation histories of massive quiescent galaxies with BAGPIPES: evidence for multiple quenching mechanisms*. MNRAS, 480, 4, 4379–4401.

Chabrier G., 2003. *Galactic Stellar and Substellar Initial Mass Function*. PASP, 115, 763–795.

Charlot S., Worthey G. & Bressan A., 1996. *Uncertainties in the Modeling of Old Stellar Populations*. ApJ, 457, 625.

Chen Y., Trager S., Peletier R. et al., 2011. *XSL: The X-Shooter Spectral Library*. volume 328 of *Journal of Physics Conference Series*, page 012023.

Chevallard J. & Charlot S., 2016. *Modelling and interpreting spectral energy distributions of galaxies with BEAGLE*. MNRAS, 462, 2, 1415–1443.

Cid Fernandes R., Mateus A., Sodré L. et al., 2005. *Semi-empirical analysis of Sloan Digital Sky Survey galaxies - I. Spectral synthesis method*. MNRAS, 358, 2, 363–378.

Cid Fernandes R. & González Delgado R.M., 2010. *Testing spectral models for stellar populations with star clusters - I. Methodology*. MNRAS, 403, 2, 780–796.

Cid Fernandes R., Pérez E., García Benito R. et al., 2013. *Resolving galaxies in time and space. I. Applying STARLIGHT to CALIFA datacubes*. A&A, 557, A86.

Cid Fernandes R., González Delgado R.M., García Benito R. et al., 2014. *Resolving galaxies in time and space. II. Uncertainties in the spectral synthesis of datacubes*. A&A, 561, A130.

Cid Fernandes R., 2018. *On tests of full spectral fitting algorithms*. MNRAS, 480, 4480–4488.

Clerc N., Merloni A., Zhang Y.Y. et al., 2016. *SPIDERS: the spectroscopic follow-up of X-ray selected clusters of galaxies in SDSS-IV*. MNRAS, 463, 4, 4490–4515.

Coccato L., Fabricius M.H., Saglia R.P. et al., 2018. *Spectroscopic decomposition of NGC 3521: unveiling the properties of the bulge and disc*. MNRAS, 477, 2, 1958–1969.

Coelho P., Barbuy B., Meléndez J. et al., 2005. *A library of high resolution synthetic stellar spectra from 300 nm to 1.8 μm with solar and α-enhanced composition*. A&A, 443, 2, 735–746.

Coelho P., Bruzual G., Charlot S. et al., 2007. *Spectral models for solar-scaled and α-enhanced stellar populations*. MNRAS, 382, 2, 498–514.

Comerón S., Salo H., Janz J. et al., 2015. *Galactic archaeology of a thick disc: Excavating ESO 533-4 with VIMOS*. A&A, 584, A34.

Conroy C., Gunn J.E. & White M., 2009. *The Propagation of Uncertainties in Stellar Population Synthesis Modeling. I. The Relevance of Uncertain Aspects of Stellar Evolution and the Initial Mass Function to the Derived Physical Properties of Galaxies*. ApJ, 699, 486–506.

Conroy C., White M. & Gunn J.E., 2010. *The Propagation of Uncertainties in Stellar Population Synthesis Modeling. II. The Challenge of Comparing Galaxy Evolution Models to Observations*. ApJ, 708, 1, 58–70.

Conroy C. & Gunn J.E., 2010. *The Propagation of Uncertainties in Stellar Population Synthesis Modeling. III. Model Calibration, Comparison, and Evaluation*. ApJ, 712, 2, 833–857.

Conroy C., 2013. *Modeling the Panchromatic Spectral Energy Distributions of Galaxies*. ARA&A, 51, 393–455.

Conselice C.J., 2003. *The Relationship between Stellar Light Distributions of Galaxies and Their Formation Histories*. ApJS, 147, 1, 1–28.

Conselice C.J., Mortlock A., Bluck A.F.L. et al., 2013. *Gas accretion as a dominant formation mode in massive galaxies from the GOODS NICMOS Survey*. MNRAS, 430, 2, 1051–1060.

Contopoulos G. & Papayannopoulos T., 1980. *Orbits in weak and strong bars*. A&A, 92, 33–46.

Courtes G., Georgelin Y., Monnet R.B.G. et al., 1988. *A New Device for Faint Objects High Resolution Imagery and Bidimensional Spectrography - First Observational Results with TIGER at CFHT 3.6-METER Telescope*. page 266.

Croom S.M., Lawrence J.S., Bland-Hawthorn J. et al., 2012. *The Sydney-AAO Multi-object Integral field spectrograph*. MNRAS, 421, 872–893.

Crosthwaite L.P., Turner J.L. & Ho P.T.P., 2000. *Structure in the Neutral Hydrogen Disk of the Spiral Galaxy IC 342*. AJ, 119, 4, 1720–1736.

Cuomo V., Lopez Aguerri J.A., Corsini E.M. et al., 2019. *Bar pattern speeds in CALIFA galaxies. II. The case of weakly barred galaxies*. A&A, 632, A51.

Dametto N.Z., Riffel R., Colina L. et al., 2019. *A SINFONI view of the nuclear activity and circumnuclear star formation in NGC 4303 - II. Spatially resolved stellar populations*. MNRAS, 482, 4437–4453.

Davis D.R. & Hayes W.B., 2014. *SpArcFiRe: Scalable Automated Detection of Spiral Galaxy Arm Segments*. ApJ, 790, 87.

Dawson K.S., Schlegel D.J., Ahn C.P. et al., 2013. *The Baryon Oscillation Spectroscopic Survey of SDSS-III*. AJ, 145, 1, 10.

Dawson K.S., Kneib J.P., Percival W.J. et al., 2016. *The SDSS-IV Extended Baryon Oscillation Spectroscopic Survey: Overview and Early Data*. AJ, 151, 2, 44.

de Amorim A.L., García-Benito R., Cid Fernandes R. et al., 2017. *The PyCASSO database: spatially resolved stellar population properties for CALIFA galaxies*. MNRAS, 471, 3, 3727–3752.

de Vaucouleurs G., 1959. *Classification and Morphology of External Galaxies.* Handbuch der Physik, 53, 275.

de Vaucouleurs G., 1963. *Revised Classification of 1500 Bright Galaxies.* ApJS, 8, 31.

Demarque P. & McClure R.D., 1977. *Stellar Populations in the Disk and Halo of the Galaxy (presented by R. D. McClure)*. page 199.

Di Matteo P., Haywood M., Combes F. et al., 2013. *Signatures of radial migration in barred galaxies: Azimuthal variations in the metallicity distribution of old stars*. A&A, 553, A102.

Dias W.S., Monteiro H., Lépine J.R.D. et al., 2019. *The spiral pattern rotation speed of the Galaxy and the corotation radius with Gaia DR2*. MNRAS, 486, 4, 5726–5736.

Dobbs C. & Baba J., 2014. *Dawes Review 4: Spiral Structures in Disc Galaxies*. PASA, 31, e035.

Dobbs C.L. & Pringle J.E., 2010. *Age distributions of star clusters in spiral and barred galaxies as a test for theories of spiral structure*. MNRAS, 409, 396–404.

Dobbs C.L., Theis C., Pringle J.E. et al., 2010. *Simulations of the grand design galaxy M51: a case study for analysing tidally induced spiral structure*. MNRAS, 403, 2, 625–645.

Dobbs C.L., Pettitt A.R., Corbelli E. et al., 2018. *Simulations of the flocculent spiral M33: what drives the spiral structure?* MNRAS, 478, 3, 3793–3808.

Dressler A., 1980. *Galaxy morphology in rich clusters: implications for the formation and evolution of galaxies.* ApJ, 236, 351–365.

Driver S.P., Andrews S.K., da Cunha E. et al., 2018. *GAMA/G10-COSMOS/3D-HST: the 0 < z < 5 cosmic star formation history, stellar-mass, and dust-mass densities*. MNRAS, 475, 3, 2891–2935.

Drory N., MacDonald N., Bershady M.A. et al., 2015. *The MaNGA Integral Field Unit Fiber Feed System for the Sloan 2.5 m Telescope*. AJ, 149, 77.

Egusa F., Sofue Y. & Nakanishi H., 2004. *Offsets between Hα and CO Arms of a Spiral*

Galaxy, NGC 4254: A New Method for Determining the Pattern Speed of Spiral Galaxies. PASJ, 56, L45–L48.

Egusa F., Kohno K., Sofue Y. et al., 2009. *Determining Star Formation Timescale and Pattern Speed in Nearby Spiral Galaxies*. ApJ, 697, 1870–1891.

Egusa F., Koda J. & Scoville N., 2011. *Molecular Gas Evolution Across a Spiral Arm in M51*. ApJ, 726, 85.

Ellison S.L., Sánchez S.F., Ibarra-Medel H. et al., 2018. *Star formation is boosted (and quenched) from the inside-out: radial star formation profiles from MaNGA*. MNRAS, 474, 2, 2039–2054.

Elmegreen D.M. & Elmegreen B.G., 1982. *Flocculent and grand design spiral structure in field, binary and group galaxies*. MNRAS, 201, 1021–1034.

Emsellem E., Cappellari M., Krajnović D. et al., 2007. *The SAURON project - IX. A kinematic classification for early-type galaxies*. MNRAS, 379, 2, 401–417.

Eskridge P.B., Frogel J.A., Pogge R.W. et al., 2000. *The Frequency of Barred Spiral Galaxies in the Near-Infrared*. AJ, 119, 536–544.

Faber S.M., 1972. *Quadratic programming applied to the problem of galaxy population synthesis.* A&A, 20, 361.

Falcón-Barroso J., Bacon R., Bureau M. et al., 2006. *The SAURON project - VII. Integral-field absorption and emission-line kinematics of 24 spiral galaxy bulges*. MNRAS, 369, 2, 529–566.

Falcón-Barroso J., Sánchez-Blázquez P., Vazdekis A. et al., 2011. *An updated MILES stellar library and stellar population models*. A&A, 532, A95.

Falcón-Barroso J., Lyubenova M., van de Ven G. et al., 2017. *Stellar kinematics across the Hubble sequence in the CALIFA survey: general properties and aperture corrections*. A&A, 597, A48.

Falcón-Barroso J., van de Ven G., Lyubenova M. et al., 2019. *The CALIFA view on stellar angular momentum across the Hubble sequence*. A&A, 632, A59.

Fall S.M. & Efstathiou G., 1980. *Formation and rotation of disc galaxies with haloes.* MNRAS, 193, 189–206.

Fan L., Lapi A., De Zotti G. et al., 2008. *The Dramatic Size Evolution of Elliptical Galaxies and the Quasar Feedback*. ApJ, 689, 2, L101.

Feltzing S., Bowers J.B. & Agertz O., 2019. *Constraining churning and blurring in the Milky Way using large spectroscopic surveys – an exploratory study*. arXiv e-prints, arXiv:1907.08011.

Font J., Beckman J.E., Epinat B. et al., 2011. *Resonant Structure in the Disks of Spiral Galaxies, Using Phase Reversals in Streaming Motions from Two-dimensional Hα Fabry-Perot Spectroscopy*. ApJ, 741, L14.

Frankel N., Rix H.W., Ting Y.S. et al., 2018. *Measuring Radial Orbit Migration in the Galactic Disk*. ApJ, 865, 2, 96.

Frankel N., Sanders J., Rix H.W. et al., 2019. *The Inside-out Growth of the Galactic Disk*. ApJ, 884, 2, 99.

Franzetti P., Scodeggio M., Garilli B. et al., 2008. *GOSSIP, a New VO Compliant Tool for SED Fitting*. volume 394 of *Astronomical Society of the Pacific Conference Series*, page 642.

Fraser-McKelvie A., Brown M.J.I., Pimbblet K.A. et al., 2016. *A photometrically and spectroscopically confirmed population of passive spiral galaxies*. MNRAS, 462, 1, L11–L15.

Fraser-McKelvie A., Brown M.J.I., Pimbblet K. et al., 2018. *Multiple mechanisms quench passive spiral galaxies*. MNRAS, 474, 2, 1909–1921.

Fraser-McKelvie A., Merrifield M., Aragón-Salamanca A. et al., 2019. *SDSS-IV MaNGA: stellar population gradients within barred galaxies*. MNRAS, 488, 1, L6–L11.

Fraser-McKelvie A., Aragón-Salamanca A., Merrifield M. et al., 2020. *SDSS-IV MaNGA: Spatially resolved star formation in barred galaxies*. arXiv e-prints, arXiv:2005.08987.

Freeman K.C., 1970. *On the Disks of Spiral and S0 Galaxies*. ApJ, 160, 811.

Fukugita M., Ichikawa T., Gunn J.E. et al., 1996. *The Sloan Digital Sky Survey Photometric System*. AJ, 111, 1748.

Fulbright J.P., 2002. *Abundances and Kinematics of Field Stars. II. Kinematics and Abundance Relationships*. AJ, 123, 1, 404–412.

Furlong M., Bower R.G., Crain R.A. et al., 2017. *Size evolution of normal and compact galaxies in the EAGLE simulation*. MNRAS, 465, 1, 722–738.

Gadotti D.A., Seidel M.K., Sánchez-Blázquez P. et al., 2015. *MUSE tells the story of NGC 4371: The dawning of secular evolution*. A&A, 584, A90.

Garcia A.A., Rasilla J.L., Arribas S. et al., 1994. *Bidimensional spectroscopy with optical fibers at the William Herschel and Nordic Optical Telescopes*. volume 2198 of

Society of Photo-Optical Instrumentation Engineers (SPIE) Conference Series, pages 75–86.

García-Benito R., González Delgado R.M., Pérez E. et al., 2019. *Spatially resolved mass-to-light from the CALIFA survey. Mass-to-light ratio vs. color relations*. A&A, 621, A120.

Garma-Oehmichen L., Cano-Díaz M., Hernández-Toledo H. et al., 2020. *SDSS-IV MaNGA: bar pattern speed estimates with the Tremaine-Weinberg method and their error sources*. MNRAS, 491, 3, 3655–3671.

Gavazzi G., Consolandi G., Dotti M. et al., 2015. *Hα3: an Hα imaging survey of HI selected galaxies from ALFALFA. VI. The role of bars in quenching star formation from $z = 3$ to the present epoch.* A&A, 580, A116.

Ge J., Yan R., Cappellari M. et al., 2018. *Recovering stellar population parameters via two full-spectrum fitting algorithms in the absence of model uncertainties*. MNRAS, 478, 2633–2649.

Ge J., Mao S., Lu Y. et al., 2019. *Recovering stellar population parameters via different population models and stellar libraries*. MNRAS, 485, 2, 1675–1693.

Gerola H. & Seiden P.E., 1978. *Stochastic star formation and spiral structure of galaxies.* ApJ, 223, 129–139.

Gerssen J., Kuijken K. & Merrifield M.R., 1997. *The shape of the velocity ellipsoid in NGC 488*. MNRAS, 288, 618–622.

Gilmore G. & Reid N., 1983. *New light on faint stars - III. Galactic structure towards the South Pole and the Galactic thick disc.* MNRAS, 202, 1025–1047.

Girardi L., Bressan A., Bertelli G. et al., 2000. *Evolutionary tracks and isochrones for low- and intermediate-mass stars: From 0.15 to 7 M_{sun}, and from Z=0.0004 to 0.03*. A&AS, 141, 371–383.

Goddard D., Thomas D., Maraston C. et al., 2017. *SDSS-IV MaNGA: Spatially resolved star formation histories in galaxies as a function of galaxy mass and type*. MNRAS, 466, 4731–4758.

Gonzalez R.A. & Graham J.R., 1996. *Tracing the Dynamics of Disk Galaxies with Optical and Infrared Surface Photometry: Color Gradients in M99*. ApJ, 460, 651.

González Delgado R.M., Cerviño M., Martins L.P. et al., 2005. *Evolutionary stellar population synthesis at high spectral resolution: optical wavelengths*. MNRAS, 357, 945–960.

González Delgado R.M., Pérez E., Cid Fernandes R. et al., 2014. *The star formation history of CALIFA galaxies: Radial structures*. A&A, 562, A47.

González Delgado R.M., García-Benito R., Pérez E. et al., 2015. *The CALIFA survey across the Hubble sequence. Spatially resolved stellar population properties in galaxies*. A&A, 581, A103.

González Delgado R.M., Cid Fernandes R., Pérez E. et al., 2016. *Star formation along the Hubble sequence. Radial structure of the star formation of CALIFA galaxies*. A&A, 590, A44.

González Delgado R.M., Pérez E., Cid Fernandes R. et al., 2017. *Spatially-resolved star formation histories of CALIFA galaxies. Implications for galaxy formation*. A&A, 607, A128.

Gonzalez-Perez V., Castander F.J. & Kauffmann G., 2011. *Colour gradients within SDSS DR7 galaxies: hints of recent evolution*. MNRAS, 411, 2, 1151–1166.

Gouliermis D.A., Elmegreen B.G., Elmegreen D.M. et al., 2017. *Hierarchical star formation across the grand-design spiral NGC 1566*. MNRAS, 468, 509–530.

Grabelsky D.A., Cohen R.S., Bronfman L. et al., 1987. *Molecular Clouds in the Carina Arm: Large-Scale Properties of Molecular Gas and Comparison with H i*. ApJ, 315, 122.

Graham M.T., Cappellari M., Li H. et al., 2018. *SDSS-IV MaNGA: stellar angular momentum of about 2300 galaxies: unveiling the bimodality of massive galaxy properties*. MNRAS, 477, 4, 4711–4737.

Grosbol P.J. & Patsis P.A., 1998. *Stellar disks of optically flocculent and grand design spirals. Decoupling of stellar and gaseous disks*. A&A, 336, 840–854.

Guerin J. & Felenbok P., 1988. *Optical fibres for astronomical applications.* volume 3 of *Astronomical Society of the Pacific Conference Series*, pages 52–62.

Gunn J.E., Siegmund W.A., Mannery E.J. et al., 2006. *The 2.5 m Telescope of the Sloan Digital Sky Survey*. AJ, 131, 2332–2359.

Hart R.E., Bamford S.P., Willett K.W. et al., 2016. *Galaxy Zoo: comparing the demographics of spiral arm number and a new method for correcting redshift bias*. MNRAS, 461, 3663–3682.

Hart R.E., Bamford S.P., Hayes W.B. et al., 2017a. *Galaxy Zoo and SPARCFIRE: constraints on spiral arm formation mechanisms from spiral arm number and pitch angles*. MNRAS, 472, 2263–2279.

Hart R.E., Bamford S.P., Casteels K.R.V. et al., 2017b. *Galaxy Zoo: star formation versus spiral arm number*. MNRAS, 468, 2, 1850–1863.

Hart R.E., Bamford S.P., Keel W.C. et al., 2018. *Galaxy Zoo: constraining the origin of spiral arms*. MNRAS, 478, 1, 932–949.

Hearnshaw J.B., 1972. *The abundances of the elements in the oldest disk stars*. Mem. RAS, 77, 55.

Heavens A.F., Jimenez R. & Lahav O., 2000. *Massive lossless data compression and multiple parameter estimation from galaxy spectra*. MNRAS, 317, 4, 965–972.

Henriques B.M.B., White S.D.M., Thomas P.A. et al., 2015. *Galaxy formation in the Planck cosmology - I. Matching the observed evolution of star formation rates, colours and stellar masses*. MNRAS, 451, 3, 2663–2680.

Hernquist L. & Mihos J.C., 1995. *Excitation of Activity in Galaxies by Minor Mergers*. ApJ, 448, 41.

Hill A.R., Muzzin A., Franx M. et al., 2017. *The Mass Growth and Stellar Ages of Galaxies: Observations versus Simulations*. ApJ, 849, 2, L26.

Ho I.T., Seibert M., Meidt S.E. et al., 2017. *The Chemical Evolution Carousel of Spiral Galaxies: Azimuthal Variations of Oxygen Abundance in NGC1365*. ApJ, 846, 1, 39.

Holmberg E., 1958. *A photographic photometry of extragalactic nebulae.* Meddelanden fran Lunds Astronomiska Observatorium Serie II, 136, 1.

Holwerda B.W., González R.A., van der Kruit P.C. et al., 2005. *The opacity of spiral galaxy disks. VI. Extinction, stellar light and color*. A&A, 444, 1, 109–117.

Hubble E.P., 1925. *NGC 6822, a remote stellar system.* ApJ, 62, 409–433.

Hubble E.P., 1926a. *A spiral nebula as a stellar system: Messier 33.* ApJ, 63, 236–274.

Hubble E.P., 1926b. *Extragalactic nebulae.* ApJ, 64, 321–369.

Hubble E.P., 1929. *A spiral nebula as a stellar system, Messier 31.* ApJ, 69, 103–158.

Hubble E.P., 1936. *Realm of the Nebulae*. Yale University Press.

Hunt J.A.S., Hong J., Bovy J. et al., 2018. *Transient spiral structure and the disc velocity substructure in Gaia DR2*. MNRAS, 481, 3, 3794–3803.

Ibarra-Medel H.J., Sánchez S.F., Avila-Reese V. et al., 2016. *SDSS IV MaNGA: the global and local stellar mass assemby histories of galaxies*. MNRAS, 463, 2799–2818.

Ibarra-Medel H.J., Avila-Reese V., Sánchez S.F. et al., 2019. *Optical integral field spectroscopy observations applied to simulated galaxies: testing the fossil record method*. MNRAS, 483, 4, 4525–4550.

Jungwiert B. & Palous J., 1994. *Stochastic self-propagating star formation with anisotropic probability distribution.* A&A, 287, 55–67.

Kalinova V., van de Ven G., Lyubenova M. et al., 2017. *The inner mass distribution of late-type spiral galaxies from <monospace>SAURON</monospace> stellar kinematic maps*. MNRAS, 464, 2, 1903–1922.

Kalnajs A.J., 1965. *The Stability of Highly Flattened Galaxies.* Ph.D. thesis, HARVARD UNIVERSITY.

Kalnajs A.J., 1973. *Spiral Structure Viewed as a Density Wave*. Proceedings of the Astronomical Society of Australia, 2, 4, 174–177.

Karachentsev I.D. & Karachentseva V.E., 2019. *A reference sample of face-on bulgeless galaxies*. MNRAS, 485, 1, 1477–1487.

Kauffmann G., Heckman T.M., White S.D.M. et al., 2003. *Stellar masses and star formation histories for 10^5 galaxies from the Sloan Digital Sky Survey*. MNRAS, 341, 1, 33–53.

Kendall S., Kennicutt R.C. & Clarke C., 2011. *Spiral structure in nearby galaxies - I. Sample, data analysis and overview of results*. MNRAS, 414, 1, 538–564.

Kendall S., Clarke C. & Kennicutt R.C., 2015. *Spiral structure in nearby galaxies - II. Comparative analysis and conclusions*. MNRAS, 446, 4, 4155–4167.

Kennedy R., Bamford S.P., Häußler B. et al., 2016a. *Galaxy And Mass Assembly (GAMA): Galaxy colour gradients versus colour, structure, and luminosity*. A&A, 593, A84.

Kennedy R., Bamford S.P., Häußler B. et al., 2016b. *Galaxy And Mass Assembly (GAMA): understanding the wavelength dependence of galaxy structure with bulge-disc decompositions*. MNRAS, 460, 4, 3458–3471.

Kennicutt R. C. J., 1983. *The rate of star formation in normal disk galaxies.* ApJ, 272, 54–67.

Kennicutt Jr. R.C., 1998. *Star Formation in Galaxies Along the Hubble Sequence*. ARA&A, 36, 189–232.

Kereš D., Katz N., Weinberg D.H. et al., 2005. *How do galaxies get their gas?* MNRAS, 363, 1, 2–28.

Kewley L.J., Jansen R.A. & Geller M.J., 2005. *Aperture Effects on Star Formation Rate, Metallicity, and Reddening*. PASP, 117, 829, 227–244.

Kinman T.D., Wirtanen C.A. & Janes K.A., 1966. *An RR LYR star survey with the Lick 20-inch. astrograph. IV. A surveyof 3 fields near North galactic pole.* ApJS, 13, 379.

Knapen J.H., Beckman J.E., Heller C.H. et al., 1995. *The Central Region in M100: Observations and Modeling*. ApJ, 454, 623.

Knapen J.H., Shlosman I. & Peletier R.F., 2000. *A Subarcsecond Resolution Near-Infrared Study of Seyfert and "Normal" Galaxies. II. Morphology*. ApJ, 529, 93–100.

Koleva M., Prugniel P., Bouchard A. et al., 2009. *ULySS: a full spectrum fitting package*. A&A, 501, 1269–1279.

Kraljic K., Bournaud F. & Martig M., 2012. *The Two-phase Formation History of Spiral Galaxies Traced by the Cosmic Evolution of the Bar Fraction*. ApJ, 757, 60.

Kreckel K., Blanc G.A., Schinnerer E. et al., 2016. *Characterizing Spiral Arm and Interarm Star Formation*. ApJ, 827, 2, 103.

Kreckel K., Ho I.T., Blanc G.A. et al., 2019. *Mapping Metallicity Variations across Nearby Galaxy Disks*. ApJ, 887, 1, 80.

Kroupa P., 2001. *The Local Stellar Initial Mass Function*. volume 228 of *Astronomical Society of the Pacific Conference Series*, page 187.

Kurucz R.L., 2011. *Including all the lines*. Canadian Journal of Physics, 89, 417–428.

Kučinskas A., Hauschildt P.H., Ludwig H.G. et al., 2005. *Broad-band photometric colors and effective temperature calibrations for late-type giants. I. Z = 0.02*. A&A, 442, 1, 281–308.

La Barbera F., Ferreras I., Vazdekis A. et al., 2013. *SPIDER VIII - constraints on the stellar initial mass function of early-type galaxies from a variety of spectral features*. MNRAS, 433, 4, 3017–3047.

Lacerna I., Ibarra-Medel H., Avila-Reese V. et al., 2020. *SDSS-IV MaNGA: global and local stellar population properties of elliptical galaxies and their assembly histories*. arXiv e-prints, arXiv:2001.05506.

Law D.R., Yan R., Bershady M.A. et al., 2015. *Observing Strategy for the SDSS-IV/MaNGA IFU Galaxy Survey*. AJ, 150, 19.

Law D.R., Cherinka B., Yan R. et al., 2016. *The Data Reduction Pipeline for the SDSS-IV MaNGA IFU Galaxy Survey*. AJ, 152, 83.

Le Borgne J.F., Bruzual G., Pelló R. et al., 2003. *STELIB: A library of stellar spectra at R ~2000*. A&A, 402, 433–442.

Leavitt H.S. & Pickering E.C., 1912. *Periods of 25 Variable Stars in the Small Magellanic Cloud.* Harvard College Observatory Circular, 173, 1–3.

Lee H.c., Worthey G., Trager S.C. et al., 2007. *On the Age and Metallicity Estimation of Spiral Galaxies Using Optical and Near-Infrared Photometry*. ApJ, 664, 1, 215–225.

Lee S.K., Idzi R., Ferguson H.C. et al., 2009. *Biases and Uncertainties in Physical Parameter Estimates of Lyman Break Galaxies from Broadband Photometry*. ApJS, 184, 1, 100–132.

Lee S.K., Ferguson H.C., Somerville R.S. et al., 2010. *The Estimation of Star Formation Rates and Stellar Population Ages of High-redshift Galaxies from Broadband Photometry*. ApJ, 725, 2, 1644–1651.

Leitherer C., Schaerer D., Goldader J.D. et al., 1999. *Starburst99: Synthesis Models for Galaxies with Active Star Formation*. ApJS, 123, 1, 3–40.

Lejeune T., Cuisinier F. & Buser R., 1997. *Standard stellar library for evolutionary synthesis. I. Calibration of theoretical spectra*. A&AS, 125, 229–246.

Lejeune T., Cuisinier F. & Buser R., 1998. *A standard stellar library for evolutionary synthesis. II. The M dwarf extension*. A&AS, 130, 65–75.

Lequeux J., Peimbert M., Rayo J.F. et al., 1979. *Reprint of 1979A&A....80..155L. Chemical composition and evolution of irregular and blue compact galaxies.* A&A, 500, 145–156.

Li H., Ge J., Mao S. et al., 2017. *SDSS-IV MaNGA: Variation of the Stellar Initial Mass Function in Spiral and Early-type Galaxies*. ApJ, 838, 2, 77.

Lin C.C. & Shu F.H., 1964. *On the Spiral Structure of Disk Galaxies.* ApJ, 140, 646.

Lin C.C. & Shu F.H., 1966. *On the Spiral Structure of Disk Galaxies, II. Outline of a Theory of Density Waves*. Proc. NAS, 55, 229–234.

Lintott C., Schawinski K., Bamford S. et al., 2011. *Galaxy Zoo 1: data release of morphological classifications for nearly 900 000 galaxies*. MNRAS, 410, 166–178.

Lintott C.J., Schawinski K., Slosar A. et al., 2008. *Galaxy Zoo: morphologies derived from visual inspection of galaxies from the Sloan Digital Sky Survey*. MNRAS, 389, 1179–1189.

López Fernández R., González Delgado R.M., Pérez E. et al., 2018. *Cosmic evolution of the spatially resolved star formation rate and stellar mass of the CALIFA survey*. A&A, 615, A27.

MacArthur L.A., Courteau S., Bell E. et al., 2004. *Structure of Disk-dominated Galaxies. II. Color Gradients and Stellar Population Models*. ApJS, 152, 2, 175–199.

Mackereth J.T. & Bovy J., 2020. *Weighing the stellar constituents of the galactic halo with APOGEE red giant stars*. MNRAS, 492, 3, 3631–3646.

Madau P., Pozzetti L. & Dickinson M., 1998. *The Star Formation History of Field Galaxies*. ApJ, 498, 1, 106–116.

Madau P. & Dickinson M., 2014. *Cosmic Star-Formation History*. ARA&A, 52, 415–486.

Majewski S.R., Schiavon R.P., Frinchaboy P.M. et al., 2017. *The Apache Point Observatory Galactic Evolution Experiment (APOGEE)*. AJ, 154, 3, 94.

Mallmann N.D., Riffel R., Storchi-Bergmann T. et al., 2018. *The first 62 AGN observed with SDSS-IV MaNGA - II. Resolvedstellar populations*. MNRAS, 478, 5491–5504.

Maltby D.T., Aragón-Salamanca A., Gray M.E. et al., 2010. *The environmental dependence of the stellar-mass-size relation in STAGES galaxies*. MNRAS, 402, 1, 282–294.

Maraston C., 1998. *Evolutionary synthesis of stellar populations: a modular tool*. MNRAS, 300, 872–892.

Maraston C., 2005. *Evolutionary population synthesis: models, analysis of the ingredients and application to high-z galaxies*. MNRAS, 362, 3, 799–825.

Maraston C., Pforr J., Renzini A. et al., 2010. *Star formation rates and masses of z ∼2 galaxies from multicolour photometry*. MNRAS, 407, 2, 830–845.

Maraston C. & Strömbäck G., 2011. *Stellar population models at high spectral resolution*. MNRAS, 418, 4, 2785–2811.

Maraston C., Hill L., Thomas D. et al., 2019. *Stellar population models based on the SDSS-IV MaStar library of stellar spectra. I. Intermediate-age/old models*. arXiv e-prints, arXiv:1911.05748.

Martin P. & Friedli D., 1997. *Star formation in bar environments. I. Morphology, star formation rates and general properties.* A&A, 326, 449–464.

Martínez-García E.E., González-Lópezlira R.A. & Bruzual-A G., 2009. *Spiral Density Wave Triggering of Star Formation in SA and SAB Galaxies*. ApJ, 694, 512–545.

Martínez-García E.E. & González-Lópezlira R.A., 2013. *Signatures of Long-lived Spiral Patterns*. ApJ, 765, 105.

Martínez-Lombilla C., Trujillo I. & Knapen J.H., 2019. *Discovery of disc truncations above the galaxies' mid-plane in Milky Way-like galaxies*. MNRAS, 483, 1, 664–691.

Martins L.P., González Delgado R.M., Leitherer C. et al., 2005. *A high-resolution stellar library for evolutionary population synthesis*. MNRAS, 358, 1, 49–65.

Martins L.P. & Coelho P., 2007. *Testing the accuracy of synthetic stellar libraries*. MNRAS, 381, 4, 1329–1346.

Masters K.L., Mosleh M., Romer A.K. et al., 2010. *Galaxy Zoo: passive red spirals*. MNRAS, 405, 2, 783–799.

Masters K.L., Nichol R.C., Hoyle B. et al., 2011. *Galaxy Zoo: bars in disc galaxies*. MNRAS, 411, 2026–2034.

Masters K.L., Lintott C.J., Hart R.E. et al., 2019. *Galaxy Zoo: unwinding the winding problem - observations of spiral bulge prominence and arm pitch angles suggest local spiral galaxies are winding*. MNRAS, 487, 2, 1808–1820.

Mathis H., Charlot S. & Brinchmann J., 2006. *Extracting star formation histories from medium-resolution galaxy spectra*. MNRAS, 365, 385–400.

Mehlert D., Thomas D., Saglia R.P. et al., 2003. *Spatially resolved spectroscopy of Coma cluster early-type galaxies. III. The stellar population gradients*. A&A, 407, 423–435.

Meidt S.E., Rand R.J. & Merrifield M.R., 2009. *Uncovering the Origins of Spiral Structure by Measuring Radial Variation in Pattern Speeds*. ApJ, 702, 277–290.

Miller R., Kennefick D., Kennefick J. et al., 2019. *Investigating the Origins of Spiral Structure in Disk Galaxies through a Multiwavelength Study*. ApJ, 874, 2, 177.

Minchev I. & Famaey B., 2010. *A New Mechanism for Radial Migration in Galactic Disks: Spiral-Bar Resonance Overlap*. ApJ, 722, 1, 112–121.

Mineikis T. & Vansevičius V., 2010. *Disk Galaxy Models Driven by Stochastic Self-Propagating Star Formation*. Baltic Astronomy, 19, 111–120.

Mingozzi M., Belfiore F., Cresci G. et al., 2020. *SDSS IV MaNGA – Metallicity and ionisation parameter in local star-forming galaxies from Bayesian fitting to photoionisation models*. arXiv e-prints, arXiv:2002.05744.

Molaeinezhad A., Falcón-Barroso J., Martínez-Valpuesta I. et al., 2017. *The imprints of bars on the vertical stellar population gradients of galactic bulges*. MNRAS, 467, 1, 353–368.

Monachesi A., Bell E.F., Radburn-Smith D.J. et al., 2016. *The GHOSTS survey - II. The diversity of halo colour and metallicity profiles of massive disc galaxies*. MNRAS, 457, 2, 1419–1446.

Morganson E., Green P.J., Anderson S.F. et al., 2015. *The Time Domain Spectroscopic Survey: Variable Selection and Anticipated Results*. ApJ, 806, 2, 244.

Moustakas J., Zaritsky D., Brown M. et al., 2011. *Evolution of the Stellar Mass-Metallicity Relation Since z=0.75*. arXiv e-prints, arXiv:1112.3300.

Mueller M.W. & Arnett W.D., 1976. *Propagating star formation and irregular structure in spiral galaxies.* ApJ, 210, 670–678.

Munari U., Sordo R., Castelli F. et al., 2005. *An extensive library of 2500 10 500 Å synthetic spectra*. A&A, 442, 3, 1127–1134.

Naab T., Johansson P.H. & Ostriker J.P., 2009. *Minor Mergers and the Size Evolution of Elliptical Galaxies*. ApJ, 699, 2, L178–L182.

Naim A., Lahav O., Buta R.J. et al., 1995. *A comparative study of morphological classifications of APM galaxies*. MNRAS, 274, 4, 1107–1125.

Navarro J.F., Yozin C., Loewen N. et al., 2018. *The innate origin of radial and vertical gradients in a simulated galaxy disc*. MNRAS, 476, 3648–3660.

Nissen P.E. & Schuster W.J., 2010. *Two distinct halo populations in the solar neighborhood. Evidence from stellar abundance ratios and kinematics*. A&A, 511, L10.

Ocvirk P., Pichon C., Lançon A. et al., 2006a. *STECKMAP: STEllar Content and Kinematics from high resolution galactic spectra via Maximum A Posteriori*. MNRAS, 365, 74–84.

Ocvirk P., Pichon C., Lançon A. et al., 2006b. *STECMAP: STEllar Content from high-resolution galactic spectra via Maximum A Posteriori*. MNRAS, 365, 46–73.

Oh S.H., Kim W.T., Lee H.M. et al., 2008. *Physical Properties of Tidal Features in Interacting Disk Galaxies*. ApJ, 683, 1, 94–113.

Pacifici C., Oh S., Oh K. et al., 2016. *Timing the Evolution of Quiescent and Star-forming Local Galaxies*. ApJ, 824, 1, 45.

Panter B., Heavens A.F. & Jimenez R., 2003. *Star formation and metallicity history of the SDSS galaxy survey: unlocking the fossil record*. MNRAS, 343, 1145–1154.

Panter B., Jimenez R., Heavens A.F. et al., 2007. *The star formation histories of galaxies in the Sloan Digital Sky Survey*. MNRAS, 378, 1550–1564.

Papovich C., Labbé I., Quadri R. et al., 2015. *ZFOURGE/CANDELS: On the Evolution of M* Galaxy Progenitors from z = 3 to 0.5*. ApJ, 803, 1, 26.

Parikh T., Thomas D., Maraston C. et al., 2018. *SDSS-IV MaNGA: the spatially resolved stellar initial mass function in ~400 early-type galaxies*. MNRAS, 477, 3, 3954–3982.

Patel S.G., Fumagalli M., Franx M. et al., 2013. *The Structural Evolution of Milky-Way-like Star-forming Galaxies since z ~1.3*. ApJ, 778, 2, 115.

Peng C.Y., Ho L.C., Impey C.D. et al., 2002. *Detailed Structural Decomposition of Galaxy Images*. AJ, 124, 266–293.

Pérez E., Cid Fernandes R., González Delgado R.M. et al., 2013. *The Evolution of Galaxies Resolved in Space and Time: A View of Inside-out Growth from the CALIFA Survey*. ApJ, 764, 1, L1.

Peterken T., Merrifield M., Aragón-Salamanca A. et al., 2020. *SDSS-IV MaNGA: Excavating the fossil record of stellar populations in spiral galaxies*. arXiv e-prints, arXiv:2005.03012.

Peterken T.G., Merrifield M.R., Aragón-Salamanca A. et al., 2019a. *A direct test of density wave theory in a grand-design spiral galaxy*. Nature Astronomy, 3, 178–182.

Peterken T.G., Fraser-McKelvie A., Aragón-Salamanca A. et al., 2019b. *Time-slicing spiral galaxies with SDSS-IV MaNGA*. MNRAS, 489, 1338–1343.

Pettitt A.R., Tasker E.J., Wadsley J.W. et al., 2017. *Star formation and ISM morphology in tidally induced spiral structures*. MNRAS, 468, 4189–4204.

Pforr J., Maraston C. & Tonini C., 2012. *Recovering galaxy stellar population properties from broad-band spectral energy distribution fitting*. MNRAS, 422, 4, 3285–3326.

Pietrinferni A., Cassisi S., Salaris M. et al., 2004. *A Large Stellar Evolution Database for Population Synthesis Studies. I. Scaled Solar Models and Isochrones*. ApJ, 612, 168–190.

Planck Collaboration, Aghanim N., Akrami Y. et al., 2018. *Planck 2018 results. VI. Cosmological parameters*. arXiv e-prints, arXiv:1807.06209.

Poetrodjojo H., Groves B., Kewley L.J. et al., 2018. *The SAMI Galaxy Survey: Spatially resolved metallicity and ionization mapping*. MNRAS, 479, 4, 5235–5265.

Pringle J.E. & Dobbs C.L., 2019. *The evolution of pitch angles of spiral arms*. MNRAS, 490, 1, 1470–1473.

Prugniel P. & Soubiran C., 2001. *A database of high and medium-resolution stellar spectra*. A&A, 369, 1048–1057.

Puerari I. & Dottori H., 1997. *A Morphological Method to Determine Corotation Radii in Spiral Galaxies*. ApJ, 476, L73–L75.

Quillen A.C., Carrillo I., Anders F. et al., 2018. *Spiral arm crossings inferred from ridges in Gaia stellar velocity distributions*. MNRAS, 480, 3, 3132–3139.

Rayner J.T., Cushing M.C. & Vacca W.D., 2009. *The Infrared Telescope Facility (IRTF) Spectral Library: Cool Stars*. ApJS, 185, 2, 289–432.

Roberts M.S., 1963. *The Content of Galaxies: Stars and Gas*. ARA&A, 1, 149.

Roberts W.W., 1969. *Large-Scale Shock Formation in Spiral Galaxies and its Implications on Star Formation*. ApJ, 158, 123.

Rodríguez-Puebla A., Primack J.R., Avila-Reese V. et al., 2017. *Constraining the galaxy-halo connection over the last 13.3 Gyr: star formation histories, galaxy mergers and structural properties*. MNRAS, 470, 1, 651–687.

Rosse W.P., 1845–1850. *Observations on the Nebulae*. Philosophical Transactions of the Royal Society of London Series I, 140, 499–514.

Rowlands K., Heckman T., Wild V. et al., 2018. *SDSS-IV MaNGA: spatially resolved star formation histories and the connection to galaxy physical properties*. MNRAS, 480, 2544–2561.

Sacchi E., Cignoni M., Aloisi A. et al., 2019. *Star Formation Histories of the LEGUS Spiral Galaxies. I. The Flocculent Spiral NGC 7793*. ApJ, 878, 1, 1.

Saha A., Claver J. & Hoessel J.G., 2002. *Cepheids and Long-Period Variables in IC 342*. AJ, 124, 2, 839–861.

Sakhibov F., Zinchenko I.A., Pilyugin L.S. et al., 2018. *Spiral arms in CALIFA galaxies traced by non-circular velocities, abundances and extinctions*. MNRAS, 474, 2, 1657–1671.

Salo H., Laurikainen E., Buta R. et al., 2010. *Bars do Drive Spiral Density Waves*. ApJ, 715, 1, L56–L61.

Sánchez S.F., García-Lorenzo B., Jahnke K. et al., 2006. *Decoupling the host and nuclear spectra of type I AGNs using integral field spectroscopy: A test on 3C 120*. New Astron. Rev., 49, 10-12, 501–507.

Sánchez S.F., Kennicutt R.C., Gil de Paz A. et al., 2012. *CALIFA, the Calar Alto Legacy Integral Field Area survey. I. Survey presentation*. A&A, 538, A8.

Sánchez S.F., 2015. *IFUs surveys, a panoramic view of galaxy evolution*. volume 309 of *IAU Symposium*, pages 85–92.

Sánchez S.F., Pérez E., Sánchez-Blázquez P. et al., 2016a. *Pipe3D, a pipeline to analyze Integral Field Spectroscopy Data: I. New fitting philosophy of FIT3D*. Rev. Mex. Astron. Astrofis., 52, 21–53.

Sánchez S.F., Pérez E., Sánchez-Blázquez P. et al., 2016b. *Pipe3D, a pipeline to analyze Integral Field Spectroscopy Data: II. Analysis sequence and CALIFA dataproducts*. Rev. Mex. Astron. Astrofis., 52, 171–220.

Sánchez S.F., Avila-Reese V., Rodríguez-Puebla A. et al., 2019. *SDSS-IV MaNGA - an archaeological view of the cosmic star formation history*. MNRAS, 482, 1557–1586.

Sánchez-Blázquez P., Peletier R.F., Jiménez-Vicente J. et al., 2006. *Medium-resolution Isaac Newton Telescope library of empirical spectra*. MNRAS, 371, 2, 703–718.

Sánchez-Blázquez P., Rosales-Ortega F.F., Méndez-Abreu J. et al., 2014. *Stellar population gradients in galaxy discs from the CALIFA survey. The influence of bars*. A&A, 570, A6.

Sánchez-Gil M.C., Jones D.H., Pérez E. et al., 2011. *Age patterns in a sample of spiral galaxies*. MNRAS, 415, 1, 753–772.

Sánchez-Menguiano L., Pérez I., Zurita A. et al., 2015. *On the morphology of dust lanes in galactic bars*. MNRAS, 450, 3, 2670–2676.

Sánchez-Menguiano L., Sánchez S.F., Kawata D. et al., 2016. *Evidence of Ongoing*

Radial Migration in NGC 6754: Azimuthal Variations of the Gas Properties. ApJ, 830, 2, L40.

Sánchez-Menguiano L., Sánchez S.F., Pérez I. et al., 2017. *Arm and interarm abundance gradients in CALIFA spiral galaxies*. A&A, 603, A113.

Sánchez-Menguiano L., Sánchez Almeida J., Muñoz-Tuñón C. et al., 2019. *Characterizing the Local Relation between Star Formation Rate and Gas-phase Metallicity in MaNGA Spiral Galaxies*. ApJ, 882, 1, 9.

Sánchez-Menguiano L., Sánchez S.F., Pérez I. et al., 2020. *Arm-interarm gas abundance variations explored with MUSE: the role of spiral structure in the chemical enrichment of galaxies*. MNRAS, 492, 3, 4149–4163.

Schaefer A.L., Tremonti C., Belfiore F. et al., 2020. *SDSS-IV MaNGA: Variations in the N/O–O/H Relation Bias Metallicity Gradient Measurements*. ApJ, 890, 1, L3.

Schinnerer E., Meidt S.E., Colombo D. et al., 2017. *The PdBI Arcsecond Whirlpool Survey (PAWS): The Role of Spiral Arms in Cloud and Star Formation*. ApJ, 836, 62.

Schönrich R. & Binney J., 2009. *Chemical evolution with radial mixing*. MNRAS, 396, 1, 203–222.

Searle L., Sargent W.L.W. & Bagnuolo W.G., 1973. *The History of Star Formation and the Colors of Late-Type Galaxies*. ApJ, 179, 427–438.

Searle L. & Zinn R., 1978. *Composition of halo clusters and the formation of the galactic halo*. ApJ, 225, 357–379.

Seidel M.K., Falcón-Barroso J., Martínez-Valpuesta I. et al., 2016. *The BaLROG project - II. Quantifying the influence of bars on the stellar populations of nearby galaxies*. MNRAS, 460, 4, 3784–3828.

Sellwood J.A. & Carlberg R.G., 1984. *Spiral instabilities provoked by accretion and star formation*. ApJ, 282, 61–74.

Sellwood J.A. & Sparke L.S., 1988. *Pattern speeds in barred spiral galaxies.* MNRAS, 231, 25P–31.

Sellwood J.A. & Wilkinson A., 1993. *Dynamics of barred galaxies*. Reports on Progress in Physics, 56, 2, 173–256.

Sellwood J.A. & Binney J.J., 2002. *Radial mixing in galactic discs*. MNRAS, 336, 3, 785–796.

Sellwood J.A. & Carlberg R.G., 2014. *Transient Spirals as Superposed Instabilities*. ApJ, 785, 137.

Silk J., 2001. *The formation of galaxy discs*. MNRAS, 324, 2, 313–318.

Simard L., Mendel J.T., Patton D.R. et al., 2011. *A Catalog of Bulge+disk Decompositions and Updated Photometry for 1.12 Million Galaxies in the Sloan Digital Sky Survey*. ApJS, 196, 1, 11.

Simkin S.M., Su H.J. & Schwarz M.P., 1980. *Nearby Seyfert galaxies.* ApJ, 237, 404–413.

Smee S.A., Gunn J.E., Uomoto A. et al., 2013. *The Multi-object, Fiber-fed Spectrographs for the Sloan Digital Sky Survey and the Baryon Oscillation Spectroscopic Survey*. AJ, 146, 32.

Smethurst R.J., Merrifield M., Lintott C.J. et al., 2019. *SNITCH: seeking a simple, informative star formation history inference tool*. MNRAS, 484, 3, 3590–3603.

Struck C., Dobbs C.L. & Hwang J.S., 2011. *Slowly breaking waves: the longevity of tidally induced spiral structure*. MNRAS, 414, 3, 2498–2510.

Suess K.A., Kriek M., Price S.H. et al., 2019a. *Half-mass Radii for ~7000 Galaxies at 1.0 ≤ z ≤ 2.5: Most of the Evolution in the Mass-Size Relation Is Due to Color Gradients*. ApJ, 877, 2, 103.

Suess K.A., Kriek M., Price S.H. et al., 2019b. *Half-mass Radii of Quiescent and Star-forming Galaxies Evolve Slowly from 0 ≲ z ≤ 2.5: Implications for Galaxy Assembly Histories*. ApJ, 885, 1, L22.

Tabor M., Merrifield M., Aragón-Salamanca A. et al., 2017. *Untangling galaxy components: full spectral bulge-disc decomposition*. MNRAS, 466, 2024–2033.

Tabor M., Merrifield M., Aragón-Salamanca A. et al., 2019. *SDSS-IV MaNGA: full spectroscopic bulge-disc decomposition of MaNGA early-type galaxies*. MNRAS, 485, 2, 1546–1558.

Tamburro D., Rix H.W., Walter F. et al., 2008. *Geometrically Derived Timescales for Star Formation in Spiral Galaxies*. AJ, 136, 2872–2885.

Taranu D.S., Obreschkow D., Dubinski J.J. et al., 2017. *Self-consistent Bulge/Disk/Halo Galaxy Dynamical Modeling Using Integral Field Kinematics*. ApJ, 850, 1, 70.

Tenjes P., Tuvikene T., Tamm A. et al., 2017. *Spiral arms and disc stability in the Andromeda galaxy*. A&A, 600, A34.

Thomas D., Maraston C., Schawinski K. et al., 2010. *Environment and self-regulation in galaxy formation*. MNRAS, 404, 4, 1775–1789.

Thornley M.D., 1996. *Uncovering Spiral Structure in Flocculent Galaxies*. ApJ, 469, L45.

Thornley M.D. & Mundy L.G., 1997a. *Are Flocculent Spirals Devoid of Density Waves? Gas Morphology and Kinematics in NGC 5055*. ApJ, 484, 1, 202–221.

Thornley M.D. & Mundy L.G., 1997b. *Dynamic and Stochastic Influences on Spiral Structure in the Flocculent Spiral NGC 4414*. ApJ, 490, 2, 682–697.

Tinsley B.M., 1968. *Evolution of the Stars and Gas in Galaxies*. ApJ, 151, 547.

Tinsley B.M., 1979. *Stellar lifetimes and abundance ratios in chemical evolution.* ApJ, 229, 1046–1056.

Tinsley B.M., 1980. *Evolution of the Stars and Gas in Galaxies*. Fundamentals Cosmic Phys., 5, 287–388.

Tojeiro R., Heavens A.F., Jimenez R. et al., 2007. *Recovering galaxy star formation and metallicity histories from spectra using VESPA*. MNRAS, 381, 1252–1266.

Toomre A., 1969. *Group Velocity of Spiral Waves in Galactic Disks*. ApJ, 158, 899.

Toomre A., 1977. *Theories of spiral structure*. ARA&A, 15, 437–478.

Tremaine S. & Weinberg M.D., 1984. *A kinematic method for measuring the pattern speed of barred galaxies*. ApJ, 282, L5–L7.

Trujillo I., Förster Schreiber N.M., Rudnick G. et al., 2006. *The Size Evolution of Galaxies since z~3: Combining SDSS, GEMS, and FIRES*. ApJ, 650, 1, 18–41.

Trujillo I., Conselice C.J., Bundy K. et al., 2007. *Strong size evolution of the most massive galaxies since z~2*. MNRAS, 382, 1, 109–120.

Tully R.B., Mould J.R. & Aaronson M., 1982. *A color-magnitude relation for spiral galaxies*. ApJ, 257, 527–537.

Valdes F., Gupta R., Rose J.A. et al., 2004. *The Indo-US Library of Coudé Feed Stellar Spectra*. ApJS, 152, 2, 251–259.

van der Wel A., Holden B.P., Zirm A.W. et al., 2008. *Recent Structural Evolution of Early-Type Galaxies: Size Growth from z = 1 to z = 0*. ApJ, 688, 1, 48–58.

van der Wel A., Bell E.F., Häussler B. et al., 2012. *Structural Parameters of Galaxies in CANDELS*. ApJS, 203, 2, 24.

van der Wel A., Franx M., van Dokkum P.G. et al., 2014. *3D-HST+CANDELS: The Evolution of the Galaxy Size-Mass Distribution since z = 3*. ApJ, 788, 1, 28.

van Dokkum P.G., Franx M., Kriek M. et al., 2008. *Confirmation of the Remarkable Compactness of Massive Quiescent Galaxies at z ∼2.3: Early-Type Galaxies Did not Form in a Simple Monolithic Collapse*. ApJ, 677, 1, L5.

van Dokkum P.G., Leja J., Nelson E.J. et al., 2013. *The Assembly of Milky-Way-like Galaxies Since z ∼2.5*. ApJ, 771, 2, L35.

Vaughan S.P., Davies R.L., Zieleniewski S. et al., 2018. *Radial measurements of IMF-sensitive absorption features in two massive ETGs*. MNRAS, 475, 1, 1073–1092.

Vazdekis A., Sánchez-Blázquez P., Falcón-Barroso J. et al., 2010. *Evolutionary stellar population synthesis with MILES - I. The base models and a new line index system*. MNRAS, 404, 1639–1671.

Vazdekis A., Coelho P., Cassisi S. et al., 2015. *Evolutionary stellar population synthesis with MILES - II. Scaled-solar and α-enhanced models*. MNRAS, 449, 1177–1214.

Vazdekis A., Koleva M., Ricciardelli E. et al., 2016. *UV-extended E-MILES stellar population models: young components in massive early-type galaxies*. MNRAS, 463, 3409–3436.

Verley S., Combes F., Verdes-Montenegro L. et al., 2007a. *Star formation in isolated AMIGA galaxies: dynamical influence of bars*. A&A, 474, 43–53.

Verley S., Leon S., Verdes-Montenegro L. et al., 2007b. *The AMIGA sample of isolated galaxies. V. Quantification of the isolation*. A&A, 472, 121–130.

Vogt F.P.A., Pérez E., Dopita M.A. et al., 2017. *Evidence for azimuthal variations of the oxygen-abundance gradient tracing the spiral structure of the galaxy HCG 91c*. A&A, 601, A61.

Wake D.A., Bundy K., Diamond-Stanic A.M. et al., 2017. *The SDSS-IV MaNGA Sample: Design, Optimization, and Usage Considerations*. AJ, 154, 86.

Walcher J., Groves B., Budavári T. et al., 2011. *Fitting the integrated spectral energy distributions of galaxies*. Ap&SS, 331, 1–52.

Weinberg M.D., 1985. *Evolution of barred galaxies by dynamical friction.* MNRAS, 213, 451–471.

Westera P., Lejeune T., Buser R. et al., 2002. *A standard stellar library for evolutionary synthesis. III. Metallicity calibration*. A&A, 381, 524–538.

Westfall K.B., Cappellari M., Bershady M.A. et al., 2019. *The Data Analysis Pipeline for the SDSS-IV MaNGA IFU Galaxy Survey: Overview*. arXiv e-prints.

White S.D.M. & Rees M.J., 1978. *Core condensation in heavy halos: a two-stage theory for galaxy formation and clustering*. MNRAS, 183, 341–358.

Whitney A., Conselice C.J., Bhatawdekar R. et al., 2019. *Unbiased Differential Size Evolution and the Inside-Out Growth of Galaxies in the Deep CANDELS GOODS Fields at* $1 \leq z \leq 7$. arXiv e-prints, arXiv:1911.02589.

Wilkinson D.M., Maraston C., Thomas D. et al., 2015. *P-MaNGA: full spectral fitting and stellar population maps from prototype observations*. MNRAS, 449, 328–360.

Wilkinson D.M., Maraston C., Goddard D. et al., 2017. *FIREFLY (Fitting IteRativEly For Likelihood analYsis): a full spectral fitting code*. MNRAS, 472, 4297–4326.

Willett K.W., Lintott C.J., Bamford S.P. et al., 2013. *Galaxy Zoo 2: detailed morphological classifications for 304 122 galaxies from the Sloan Digital Sky Survey*. MNRAS, 435, 2835–2860.

Wood D.B., 1966. *Multicolor Photoelectric Photometry of Galaxies*. ApJ, 145, 36.

Worthey G., 1994. *Comprehensive Stellar Population Models and the Disentanglement of Age and Metallicity Effects*. ApJS, 95, 107.

Wuyts S., Förster Schreiber N.M., Lutz D. et al., 2011. *On Star Formation Rates and Star Formation Histories of Galaxies Out to z ∼3*. ApJ, 738, 1, 106.

Xu Y., Hou L.G. & Wu Y.W., 2018. *The spiral structure of the Milky Way*. Research in Astronomy and Astrophysics, 18, 12, 146.

Yan R., Bundy K., Law D.R. et al., 2016a. *SDSS-IV MaNGA IFS Galaxy Survey: Survey Design, Execution, and Initial Data Quality*. AJ, 152, 197.

Yan R., Tremonti C., Bershady M.A. et al., 2016b. *SDSS-IV/MaNGA: Spectrophotometric Calibration Technique*. AJ, 151, 8.

Yan R., Chen Y., Lazarz D. et al., 2019. *SDSS-IV MaStar: A Large and Comprehensive Empirical Stellar Spectral Library—First Release*. ApJ, 883, 2, 175.

Yi S.K., 2003. *Uncertainties of Synthetic Integrated Colors as Age Indicators*. ApJ, 582, 1, 202–214.

Yi S.K., 2008. *The Current Understanding on the UV Upturn*. volume 392 of *Astronomical Society of the Pacific Conference Series*, page 3. Astronomical Society of the Pacific.

Yoachim P. & Dalcanton J.J., 2006. *Structural Parameters of Thin and Thick Disks in Edge-on Disk Galaxies*. AJ, 131, 1, 226–249.

Zhang X., 2016. *N-body simulations of collective effects in spiral and barred galaxies*. Astron. & Comp., 17, 86–128.

Zheng Z., Wang H., Ge J. et al., 2017. *SDSS-IV MaNGA: environmental dependence of stellar age and metallicity gradients in nearby galaxies*. MNRAS, 465, 4, 4572–4588.

Zhu L., van de Ven G., Méndez-Abreu J. et al., 2018. *Morphology and kinematics of orbital components in CALIFA galaxies across the Hubble sequence*. MNRAS, 479, 1, 945–960.